Oxidative Medicine and Cellular Longevity

The Bio-Effects Caused by Ionizing Radiation-Derived Intracellular Redox Reaction

Lead Guest Editor: Fei Ye
Guest Editors: Yi Xie, Chao Sun, Lu Cai, and Bing Wang

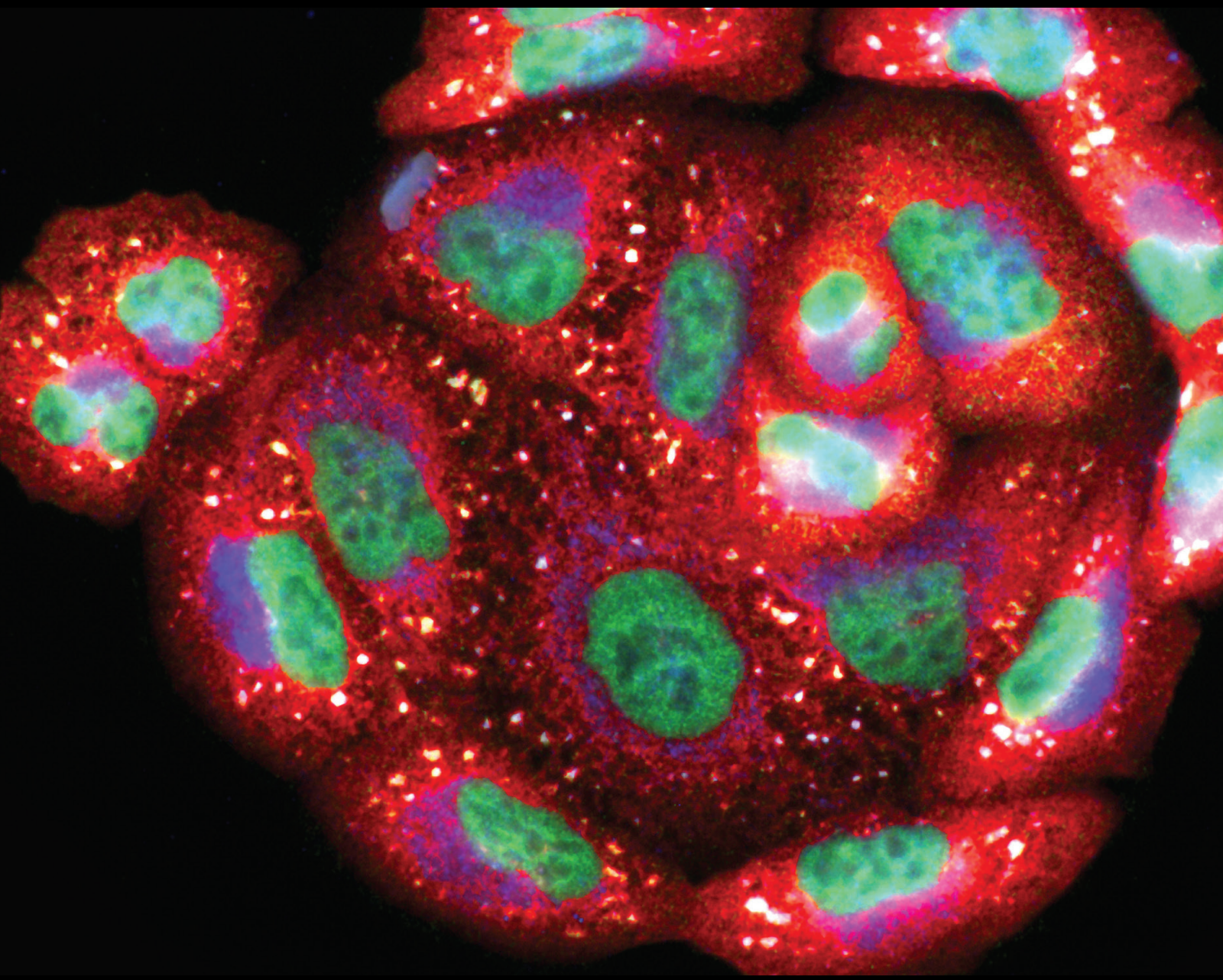

The Bio-Effects Caused by Ionizing Radiation-Derived Intracellular Redox Reaction

Oxidative Medicine and Cellular Longevity

The Bio-Effects Caused by Ionizing Radiation-Derived Intracellular Redox Reaction

Lead Guest Editor: Fei Ye
Guest Editors: Yi Xie, Chao Sun, Lu Cai, and Bing Wang

Chief Editor

Jeannette Vasquez-Vivar, USA

Associate Editors

Amjad Islam Aqib, Pakistan
Angel Catalá, Argentina
Cinzia Domenicotti, Italy
Janusz Gebicki, Australia
Aldrin V. Gomes, USA
Vladimir Jakovljevic, Serbia
Thomas Kietzmann, Finland
Juan C. Mayo, Spain
Ryuichi Morishita, Japan
Claudia Penna, Italy
Sachchida Nand Rai, India
Paola Rizzo, Italy
Mithun Sinha, USA
Daniele Vergara, Italy
Victor M. Victor, Spain

Academic Editors

Ammar AL-Farga, Saudi Arabia
Mohd Adnan, Saudi Arabia
Ivanov Alexander, Russia
Fabio Altieri, Italy
Daniel Dias Rufino Arcanjo, Brazil
Peter Backx, Canada
Amira Badr, Egypt
Damian Bailey, United Kingdom
Rengasamy Balakrishnan, Republic of Korea
Jiaolin Bao, China
Ji C. Bihl, USA
Hareram Birla, India
Abdelhakim Bouyahya, Morocco
Ralf Braun, Austria
Laura Bravo, Spain
Matt Brody, USA
Amadou Camara, USA
Marcio Carocho, Portugal
Peter Celec, Slovakia
Giselle Cerchiaro, Brazil
Arpita Chatterjee, USA
Shao-Yu Chen, USA
Yujie Chen, China
Deepak Chhangani, USA
Ferdinando Chiaradonna, Italy
Zhao Zhong Chong, USA
Fabio Ciccarone, Italy
Alin Ciobica, Romania
Ana Cipak Gasparovic, Croatia
Giuseppe Cirillo, Italy
Maria R. Ciriolo, Italy
Massimo Collino, Italy
Manuela Corte-Real, Portugal
Manuela Curcio, Italy
Domenico D'Arca, Italy
Francesca Danesi, Italy
Claudio De Lucia, USA
Damião De Sousa, Brazil
Enrico Desideri , Italy
Francesca Diomede, Italy
Raul Dominguez-Perles, Spain
Joël R. Drevet, France
Grégory Durand, France
Alessandra Durazzo, Italy
Javier Egea, Spain
Pablo A. Evelson, Argentina
Mohd Farhan, USA
Ioannis G. Fatouros, Greece
Gianna Ferretti, Italy
Swaran J. S. Flora, India
Maurizio Forte, Italy
Teresa I. Fortoul, Mexico
Anna Fracassi , USA
Rodrigo Franco, USA
Juan Gambini, Spain
Gerardo García-Rivas, Mexico
Husam Ghanim, USA
Jayeeta Ghose, USA
Rajeshwary Ghosh, USA
Lucia Gimeno-Mallench , Spain
Anna M. Giudetti, Italy
Daniela Giustarini, Italy
José Rodrigo Godoy, USA
Saeid Golbidi, Canada
Guohua Gong, China
Tilman Grune, Germany
Solomon Habtemariam, United Kingdom
Eva-Maria Hanschmann, Germany
Md Saquib Hasnain, India
Md Hassan, India

Contents

Hindawi
Oxidative Medicine and Cellular Longevity
Volume 2022, Article ID 1622829, 11 pages
https://doi.org/10.1155/2022/1622829

Research Article

Comprehensive Temporal Protein Dynamics during Postirradiation Recovery in *Deinococcus radiodurans*

Yan Xiong,[1] Linyang Wei,[2] Shuchen Xin,[2] Rui Min,[2] Feng Liu,[2] Nuomin Li,[2] and Yongqian Zhang[2]

[1]*Analysis & Testing Center, Beijing Institute of Technology, Beijing 102488, China*
[2]*School of Life Science, Beijing Institute of Technology, Beijing 100081, China*

Correspondence should be addressed to Yongqian Zhang; zyq@bit.edu.cn

Received 11 July 2022; Accepted 19 September 2022; Published 11 November 2022

Academic Editor: Fei Ye

Deinococcus radiodurans (*D. radiodurans*) is an extremophile that can tolerate ionizing radiation, ultraviolet radiation, and oxidation. How *D. radiodurans* responds to and survives high levels of ionizing radiation is still not clear. In this study, we performed label-free proteomics to explore the proteome dynamics during postirradiation recovery (PIR). Surprisingly, proteins involved in translation were repressed during the initial hours of PIR. *D. radiodurans* also showed enhanced DNA repair and antioxidative response after 6 kGy of gamma irradiation. Moreover, proteins involved in sulfur metabolism and phenylalanine metabolism were enriched at 1 h and 12 h, respectively, indicating different energy and material needs during PIR. Furthermore, based on these findings, we proposed a novel model to elucidate the possible molecular mechanisms of robust radioresistance in *D. radiodurans*, which may serve as a reference for future radiation repair.

1. Introduction

Deinococcus radiodurans (*D. radiodurans*) is one of the most radiation-resistant organisms found on Earth [1–3]. The molecular basis of postirradiation recovery (PIR) after a high dose of radiation has become the focus of intense research on the radiation tolerance mechanism of *D. radiodurans*. Previous studies have found that *D. radiodurans* has superb DNA repair ability and a remarkable antioxidative system [4, 5].

At present, most of the evidence regarding the DNA repair mechanism and oxidative stress resistance comes from the transcriptome, knockout mutagenesis, the DNA repair kinetics of mutants, and the activities of DNA repair-related candidate proteins and antioxidant enzymes [6–11]. A few details of the protein changes involved in the *D. radiodurans* radiation-resistant mechanism have also been reported by quantitative proteomics [12–16].

Although these results have shown that several key proteins played an important role in the radiation tolerance mechanism of *D. radiodurans*, they lack deep protein coverage, global protein analysis, and elucidation of the dynamic changes during PIR, which limits further understanding of the biological processes involved in the response to ionizing radiation.

To the best of our knowledge, a comprehensive analysis of the specific radiation tolerance mechanism of *D. radiodurans* has not yet been performed. As the label-free quantitative proteomics method is effective in screening and identifying protein profiles [17, 18], it was applied to conduct a systematic and comprehensive proteomic analysis on *D. radiodurans* at different time points during PIR after 6 kGy γ-irradiation. A total of 413 differentially abundant proteins (DAPs, $s_0 = 2.0$, FDR < 0.05) were reported. The observed profile showed that proteins involved in DNA repair, antioxidative response, sulfur metabolism, and phenylalanine metabolism were significantly enriched. The dataset also resolves the timing of protein induction and repression, indicating the potential primary molecular functions at specific times during PIR.

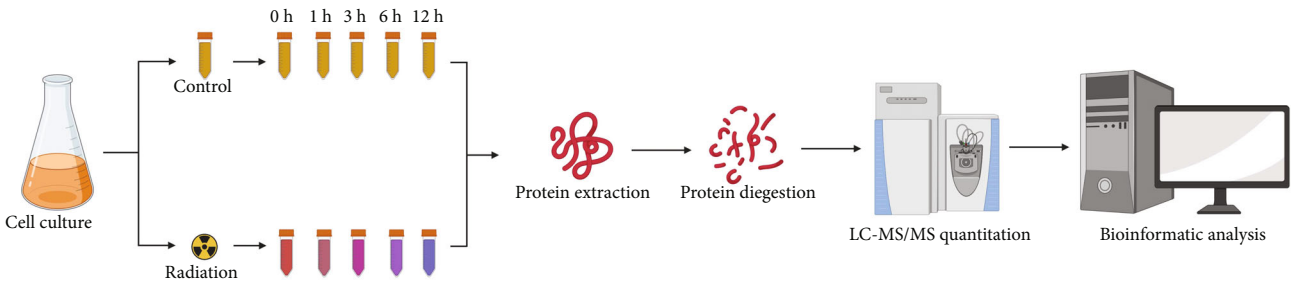

Figure 1: Experimental workflow for differentially abundant proteins in *D. radiodurans* during postirradiation recovery. After radiation, the bacteria in the control and irradiation groups were collected at the required time intervals (0 h, 1 h, 3 h, 6 h, and 12 h) during PIR. Proteins were extracted, digested, and then, subjected to LC–MS/MS analysis. Finally, differentially abundant proteins were evaluated by label-free quantitation.

The proteomic changes incorporated in this study preliminarily elucidate the possible mechanism underlying the radiation resistance of *D. radiodurans*.

2. Materials and Methods

2.1. Strains and Culture Conditions. D. radiodurans cells were purchased from the China Common Microorganism Collection Management Center (No. 1.633, CGMCC, Beijing, China). The strains were cultured in TGY liquid medium (1% tryptone, 0.5% glucose, and 0.1% yeast extract) at 30°C with shaking at 150 rpm.

2.2. Irradiation Conditions and Postirradiation Recovery. The bacteria were cultured to the early stationary phase (at an OD_{600} of 1.5, 30°C, 150 rpm) and subjected to 6 kGy of ^{60}Co γ-rays at a dose rate of 30 Gy/min (Peking University, Beijing, China). Another aliquot without irradiation served as the control group. Subsequently, irradiated and control suspensions were centrifuged (10000 × g, 5 min, 4°C) and transferred to fresh TGY at an initial OD_{600} of 0.1 to allow recovery (30°C, 150 rpm). Cell turbidities were collected every 2 hours during PIR. At the required time intervals (0 h, 1 h, 3 h, 6 h, and 12 h), the cells were washed twice with PBS buffer and harvested after centrifugation (10000 × g, 10 min, 4°C). These experiments included three independent biological repeats.

2.3. Scanning Electron Microscopy (SEM) and Transmission Electron Microscopy (TEM) Analysis. After irradiation, electron microscopy was performed to analyze cytological morphology [19, 20]. All experimental bacterial strains were collected and fixed with 2.5% glutaraldehyde. The fixed cells were dehydrated by a graded series of ethanol for 15 min each step. For SEM analysis, cells were transferred to isoamyl acetate and dried in a Hitachi Model HCP-2 critical point dryer (Hitachi, Japan) with liquid CO_2. Pellets for SEM examination were coated with gold and viewed with a Hitachi SU8010SEM instrument (*Hitachi*, Japan). For TEM analysis, specimens were processed as described previously [20]. Ultrathin sections (70–90 nm) were stained with lead citrate and uranyl acetate and observed using a Hitachi H-7650 TEM instrument (Hitachi, Japan).

2.4. Protein Extraction and Digestion. The collected bacteria were dissolved in lysis buffer (8 M urea, 2 mM EDTA, 1 mM PMSF) and extracted by ultrasonication in an ice bath (SONICS VCX800, *power*: 800 W, frequency: 20 kHz, treatment time 4 min, vibration 2 s, interval 2 s). The total protein supernatant was centrifuged at 15000 × g for 45 min at 4°C. The protein concentration was optimized using a bicinchoninic acid (BCA) assay kit (Pierce, MA, USA).

For digestion, 50 μg of protein from each sample was used. The protein was reduced by incubating at 56°C for 30 min with 10 mM dithiothreitol (DTT, Sigma). Finally, 50 mM iodoacetamide (IAA, Sigma) was added for alkylation for 30 min. After dilution with 50 mM NH_4HCO_3 to decrease the urea concentration to below 2 M, the protein was first digested with trypsin at 37°C overnight at a mass ratio of 50 : 1 (m/m, protein : trypsin) and subsequently at a ratio of 100 : 1 (m/m, protein : trypsin) at 37°C for 4 h.

Finally, digestion was ended by 1% formic acid (v/v). Peptides were desalted by a Monospin C18 column (Shimadzu, 5010-21700). The desalted eluates were dried, and pellets were stored at -80°C until further analysis.

2.5. NanoLC–MS/MS Analysis. Peptides from each sample were dissolved in loading buffer (0.1% FA, v/v) and centrifuged at 12,000 × g for 10 min. The supernatant was analyzed on a U-3000 nanoLC system (dp92br2) coupled to a Q-Exactive HFX mass spectrometer (Thermo Fisher Scientific, Bremen, Germany). Peptides were separated using a 15 cm house-made C18 reversed-phase column (100 μm inner diameter, 1.9 μm resin) and a 90 min elution gradient. Mobile phase A consisted of 0.1% FA and H_2O, and mobile phase B consisted of 20% H_2O and 80% ACN. A 90 min gradient (mobile phase B: 5% at 0 min, 10% at 16 min, 22% at 60 min, 35% at 78 min, 99% at 83 min, 99% at 85 min, 5% at 86 min, and 0% at 90 min) was used at a flow rate of 300 nl/min. The data were acquired in a data-dependent mode. For mass spectrometry parameters, the m/z range was set to 350-1500 for the MS scan, and the accumulation time was 0.25 s. The top 20 most intense ions in MS1 were selected for MS/MS analysis, and the dynamic exclusion time was 20 s.

2.6. Protein Identification and Quantification. The MS/MS data were searched against the *D. radiodurans* database from

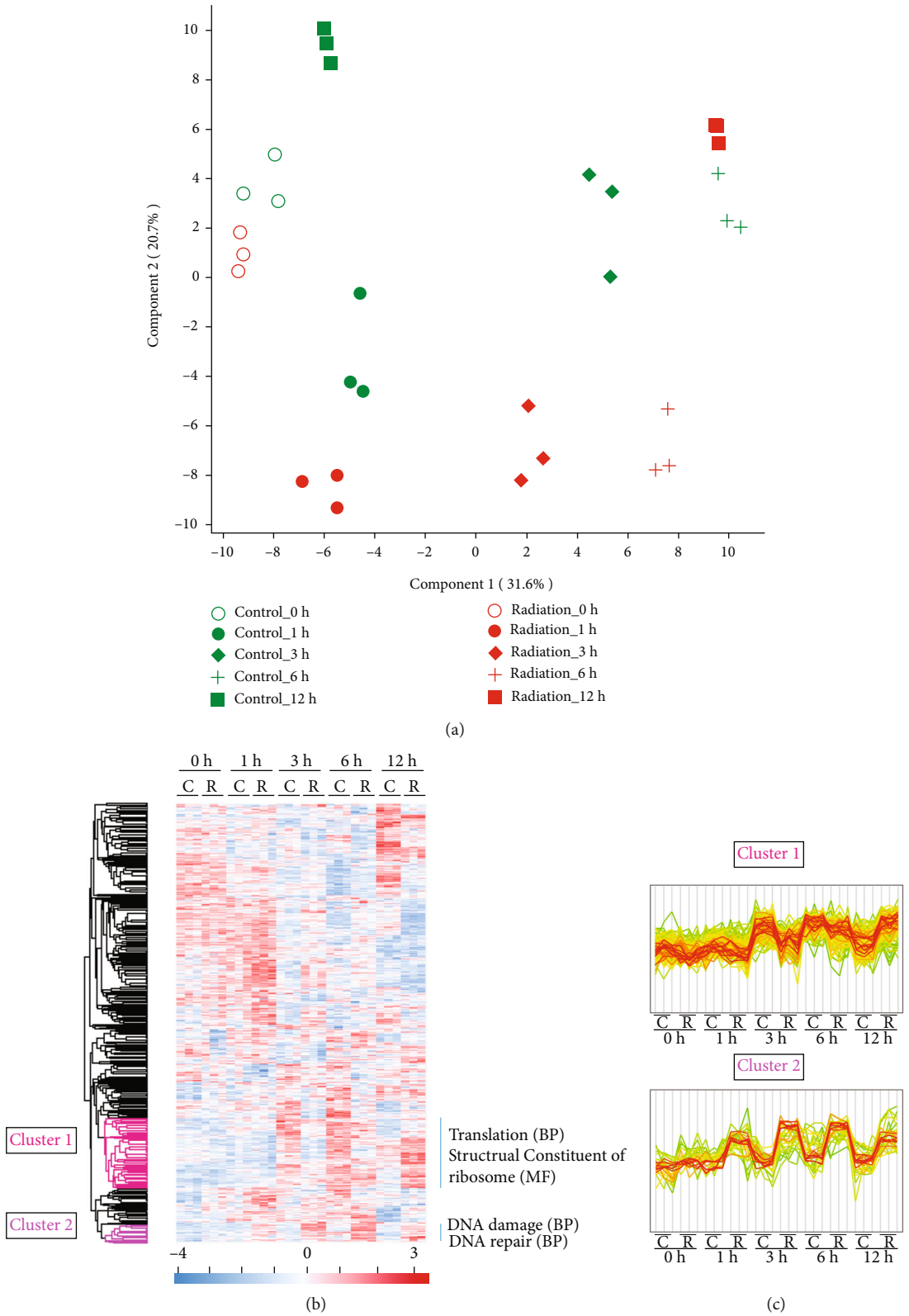

Figure 2: Principal component analysis (PCA) and cluster analysis of proteome data. (a) PCA score biplot of protein percentage data of samples during PIR. The cumulative data variance on the first two PCs was 52.3%. (b) Cluster analysis demonstrating the grouping of the replicate samples and 2 clusters with significantly enriched GO terms. (c) Expression levels are shown in the two clusters (Supplementary Table S8), in which cluster 1 includes translation (GOBP) and structural constituent of ribosome (GOMF) (119 proteins, $p = 7.5E - 3$), and cluster 2 includes DNA damage and DNA repair (GOBP) (31 proteins, $p = 1.8E - 4$). Proteins belonging to the cluster are shown in green to red based on the distance from the mean of all proteins in the cluster.

Table 1: Numbers of DAPs during postirradiation recovery.

Postirradiation recovery/h	Upregulated proteins	Downregulated proteins	Differentially abundant proteins (DAPs)
0	6	6	12
1	10	8	18
3	57	65	122
6	60	57	117
12	124	148	272

UniProtKB (https://www.uniprot.org/, uniprot-proteome_UP000002524, last modified on 12/1/2019, 3085 proteins) with MaxQuant software (v 1.6.4.0). The search parameters were as follows: the specific enzyme was trypsin KR_C, which allows up to 4 missing cleavages; carbamidomethyl[C] was set as the fixed modification; oxidation [M] and acetyl [ProteinN-term] were the variable modifications; and the precursor and fragment tolerances were both set to 20 ppm. All protein identification was based on the criteria of a false discovery rate (FDR) less than 1%. The option of matching between runs was enabled with a matching time window of 0.7 min and alignment window of 20 min. The other parameters in MaxQuant were set to the default values. The built-in label-free quantification algorithm (LFQ) in MaxQuant was applied for quantification. The missing values in proteomic datasets were imputed using *NAguideR* [21].

2.7. Bioinformatics Analysis. Statistical analysis was performed by Perseus (v.1.6.2.3). The differential proteins were identified at a 5% FDR threshold ($s0 = 2.0$). Furthermore, the functional annotations of differential proteins were analyzed by DAVID 6.8 bioinformatics tools (https://david.ncifcrf.gov/) [22]. Gene Ontology (GO) biological process (GOBP), GO cellular components (GOCC), and GO molecular function (GOMF) terms were identified with FDR < 0.05. STRING (https://www.string-db.org/), Cytoscape (version 3.6.1), plugin ClueGO (version 2.5.4), and Cluepedia (version 1.5.4) were used to show protein–protein interactions (PPIs) of related proteins. A two-sided hypergeometric test with a Benjamini–Hochberg correction was performed to assess enrichment significance. Only results with p value < 0.05 are presented. The kappa score of PPI was set to 0.7. KEGG (Kyoto Encyclopedia of Genes and Genomes) was also applied for pathway analysis, and p value < 0.05 was considered to be significant using a two-sided hypergeometric test with a Fisher correction.

3. Results and Discussion

The overall experimental workflow is shown in Figure 1. The growth curve during PIR is shown in Figure S1, and quantitative information was obtained for 1942 proteins and 11095 peptides across all samples (Supplementary Table S1-2). The overall reproducibility of these MS-MS data was assessed by performing multivariate statistical analysis. As shown in Figure 2, the first principal component (PC1) captures 31.6% of the variance, followed by PC2 with a 20.7% variance. Visual inspection of the data showed a clear separation of the samples between control and irradiation-treated cells.

The numbers of differentially abundant proteins (DAPs) are shown in Table 1 and Figure 3 (Supplementary Table S3-7). As it took time to recover from irradiation, there were few DAPs at 0 h of PIR. The DAPs at 1, 3, 6, and 12 h were subjected to further detailed analysis. We used the DAVID bioinformatics tool to understand the GO clusters of the DAPs at the systems level (Figures 2(b) and 2(c)). According to cluster analysis, upregulated proteins involved in DNA repair (GOBP, cluster 2) at the time intervals of 1, 3, and 6 h; proteins in translation (GOBP, cluster 1) were downregulated at time intervals of 1 and 3 h and while upregulated at 12 h. These dynamic changes indicated that cells slowed down translation and engaged in DNA repair to recover in the early stages of PIR and resumed active growth at later times.

3.1. DNA Damage Response. The unusual radioresistance of *D. radiodurans* primarily originates from its efficient DNA repair ability. Proteomic analysis revealed that functional categories of DNA repair were overrepresented in *D. radiodurans* exposed to irradiation compared with the control cells (Figures 2(b) and 2(c)).

Additionally, Figure 4(a) shows that there were seven DAPs overlapping all the stages of PIR: DNA repair protein PprA, CinA-like protein, protein RecA (recombinase A), DNA damage response protein D (DdrD), single-stranded DNA-binding protein (Ssb), DNA gyrase subunit A (GyrA), and DNA topoisomerase (ATP-hydrolyzing). These proteins were all upregulated and participated in DNA repair.

Single-stranded DNA-binding protein (Ssb) is vital for cell survival in replication and DNA damage repair [23]. Altered Ssb expression significantly affects ionizing radiation tolerance at both the transcript and protein levels [12, 24]. RecA plays a unique role in the repair of DNA damage. It is a recombinase mediating homologous recombination [25]. Comparative proteomics revealed RecA recruitment to the nucleoid of Deinococcus after irradiation-induced DNA damage [26]. PprA is a species-specific radiation-induced protein that ameliorates DNA damage. It plays a critical role in the radiation-induced nonhomologous end-joining repair mechanism [27]. In vivo, PprA interacted with GyrA and DNA topoisomerase to preserve the integrity of the *D. radiodurans* genome after DNA damage [28]. Similar to other Ddr proteins, ddrD gene expression is controlled by the IrrE/DdrO protein pair, and DdrD likely contributes to cell recovery after extensive genotoxic stress [29].

Investigations with TEM and SEM confirmed this observation. The typical *D. radiodurans* morphology of tetracocci is shown in Figure 5. The ultrastructure of the cell envelope of the radiation group showed that DNA could spread between

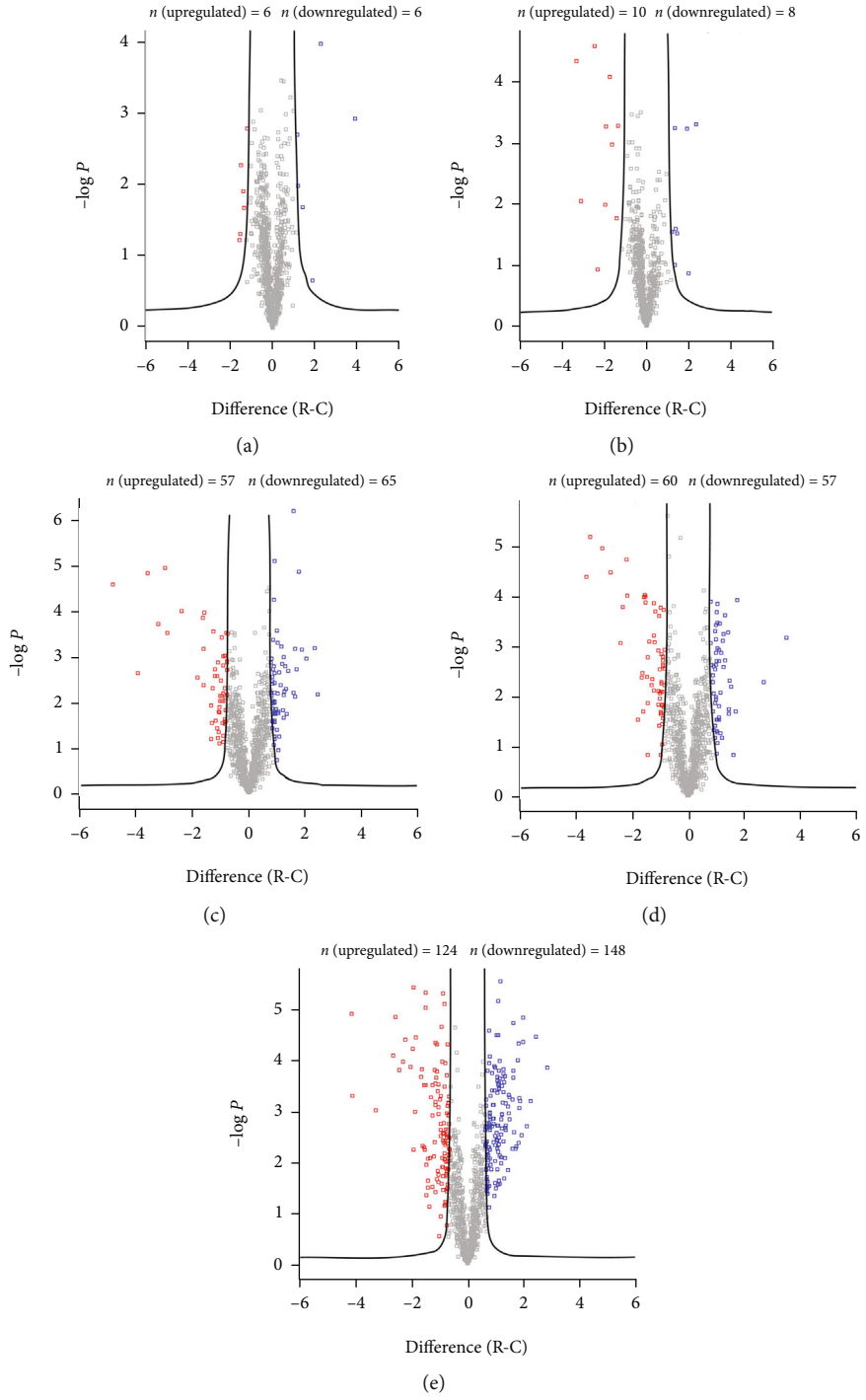

Figure 3: Volcano plots illustrate differentially abundant proteins. Protein abundance ($\log_2$ fold change) obtained by MS/MS analysis of cells in the control and irradiation groups was plotted against its statistical p value. The curve was derived at false discovery rate (FDR) = 0.05 and $s0 = 2.0$. Upregulated proteins are colored red, while downregulated proteins are colored blue.

the two compartments through a membranous orifice (Figure 5(d)). These structural features were conducive to DNA repair in *D. radiodurans* [30].

Notably, the protein CinA, whose function remains unknown, was upregulated after irradiation. It has been reported that a DNA damage/competence-inducible protein encoded by the cinA ortholog from *Streptococcus pneumonia* could interact physically with RecA [31, 32]. Combined with the PPIs of DAPs (Figure 6(a)), the observed upregulation of CinA may indicate a potential role in the DNA repair system, which needs further study. Altogether, the proteins of *D. radiodurans* that were upregulated in all the stages of PIR indicated extraordinary resistance to the lethal and mutagenic effects of ionizing radiation (Figure 7).

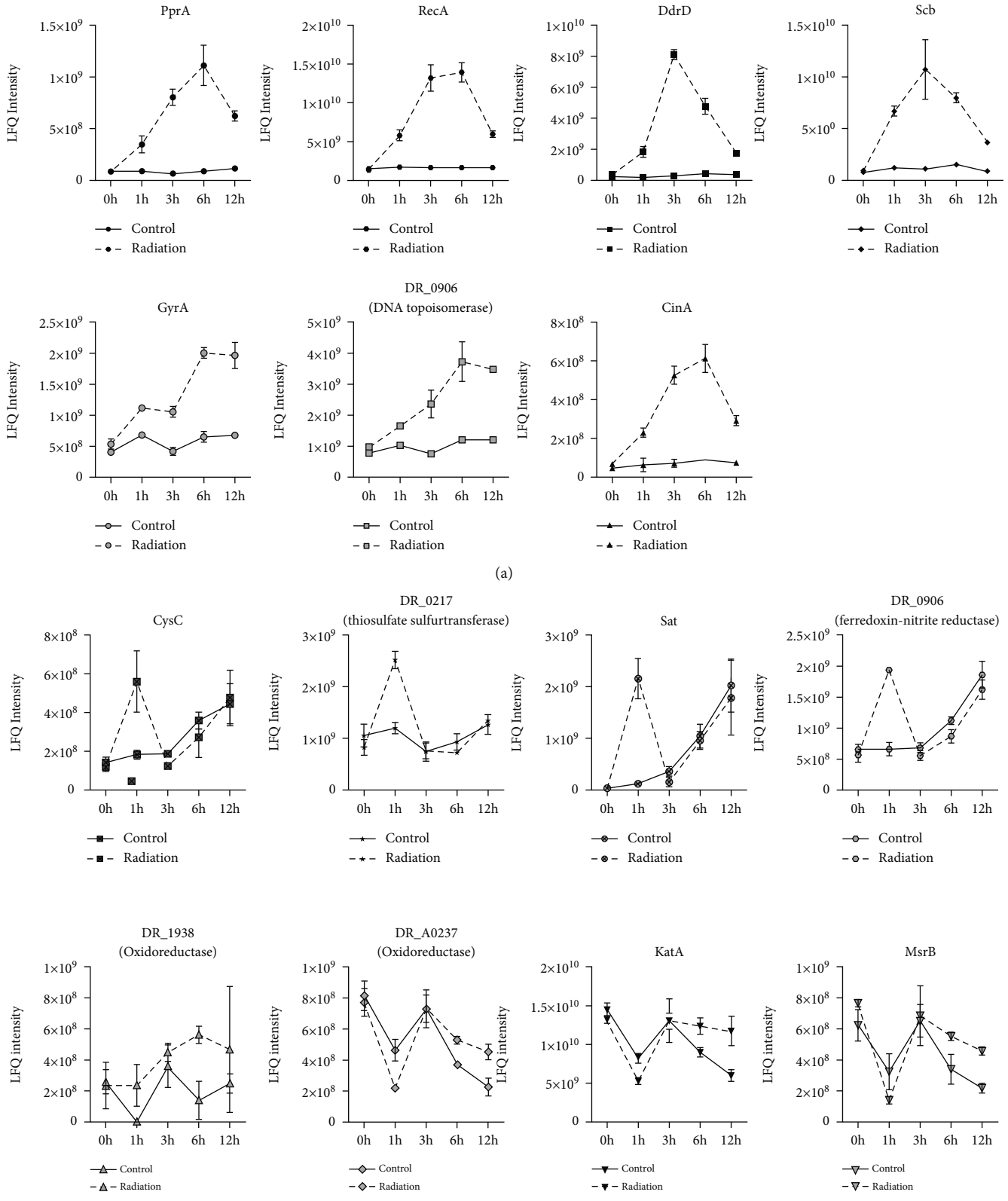

Figure 4: Specific examples of temporal protein profile data. (a) Differentially abundant proteins involved in the DNA damage response. (b) Differentially abundant proteins involved in the antioxidative response. Error bars represent the standard error of triplicate protein relative intensity measurements.

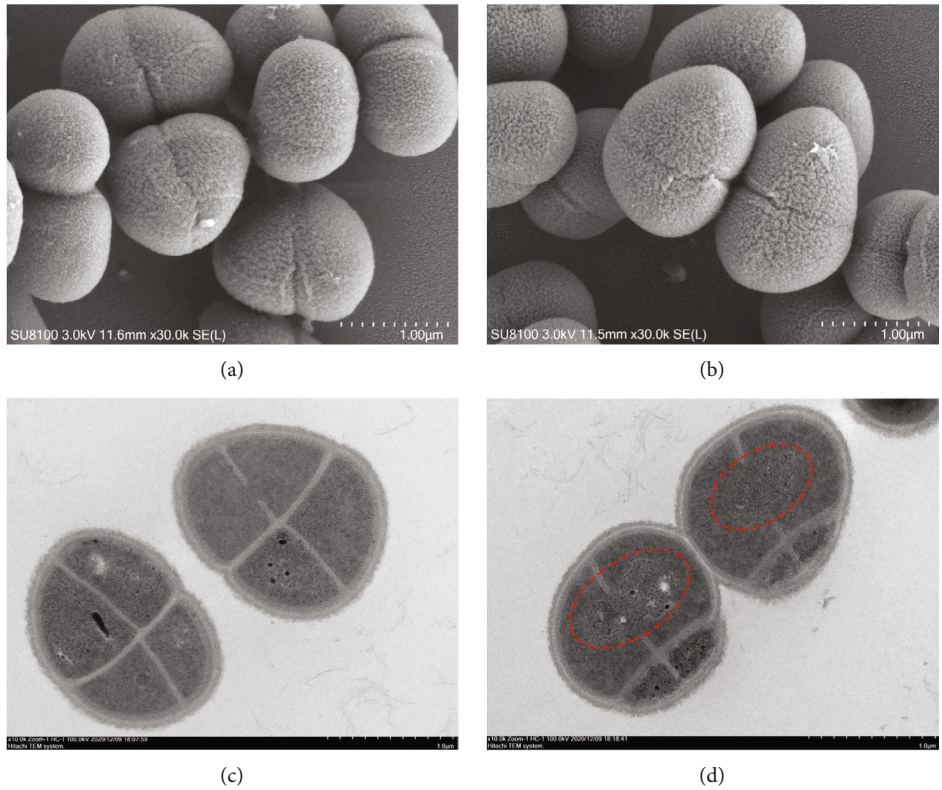

Figure 5: Morphology in *D. radiodurans* after irradiation. (a) SEM images of control cells; (b) SEM images of irradiated cells; (c) TEM images of control cells; (d) TEM images of irradiated cells. DNA spreading between the two compartments through a membranous orifice were marked in dashed red circle.

3.2. Antioxidative Response. Reactive oxygen species (ROS) generated by ionizing radiation (IR) are deleterious for all organisms, and *D. radiodurans* has evolved robust antioxidant systems to overcome ROS-mediated damage. Our comparative proteomic analysis revealed several differentially abundant proteins related to oxidative stress defense after gamma irradiation (Figure 7).

Proteins involved in the general stress response function to protect and repair damage to cellular structures, such as DNA, the cell envelope, and proteins, and to provide microorganisms the ability to recuperate from the stress they experience (Figure 4(b)). Oxidoreductase, which belongs to the short-chain dehydrogenase/reductase (SDR) family (DR_1938), was upregulated during PIR. Another oxidoreductase (DR_A0237), catalase (KatA), and peptide methionine sulfoxide reductase (MsrB) were differentially upregulated at both 6 h and 12 h. Ferredoxin-nitrite reductase (DR_A0013), thiosulfate sulfurtransferase (DR_0217), sulfate adenylyltransferase (Sat), and adenylyl-sulfate kinase (CysC) were differentially upregulated at 1 h. KatA is an important catalase in the disproportionation of H_2O_2 to water and oxygen. *D. radiodurans* with mutagenesis of KatA showed more sensitivity to irradiation [6]. KatA is a well-studied protein that protects *D. radiodurans* from oxidative stress [14]. Because of its sulfur-containing structure, methionine is relatively easily oxidized to yield methionine sulfoxide, leading to conformational changes or inactivation of a protein. Subsequently, methionine sulfoxide can be catalyzed by methionine sulfoxide reductases (Msr proteins) [33, 34]. Therefore, Msr proteins are critical antioxidant enzymes that alleviate the damage caused by oxidative stress [35]. Recent results found that MsrA/B were able to rescue oxidized RecA activities [36]. Moreover, the proteometabolomic response revealed that KatA and MsrA were upregulated under UVC and vacuum conditions [15]. As MsrA and MsrB have complementary stereospecificities in the repair of MetSO in oxidized proteins, we speculated that the upregulation of MsrB contributed to defense against oxidative stresses by reducing methionine sulfoxide residues.

Considering their temporal dynamics during PIR, these proteins upregulated at different time interval during PIR, which indicated multiple strategies were applied in response to oxidative stress. At early stage, enzymes participating in ferredoxin regulation played a role in homeostasis of intracellular metal to resist to ROS-mediated damage, while proteins in deletion of H_2O_2 and reversing oxidative forms of sulfur containing amino acids contributed to protection of the bacteria from oxidative stress at late stage.

3.3. Sulfur Metabolism and Phenylalanine Metabolism. In addition, KEGG pathway analysis revealed that proteins participating in sulfur metabolism and phenylalanine metabolism were enriched at time intervals of 1 h and 12 h, respectively. Both metabolisms play important roles in protein synthesis, as cysteine and methionine are two essential amino acids that contain sulfur, and phenylalanine is an essential aromatic amino acid.

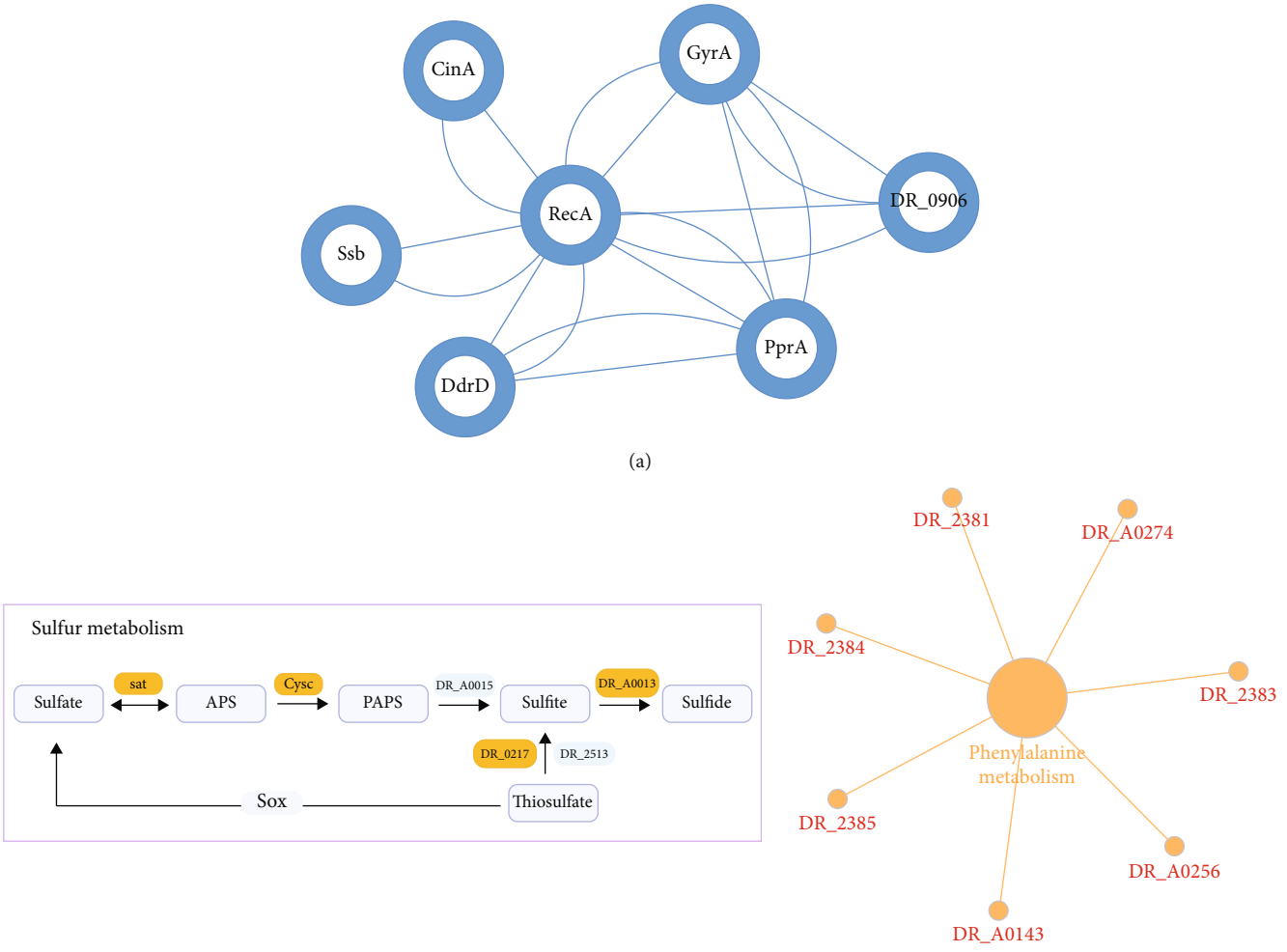

FIGURE 6: Protein illustration of *D. radiodurans* in response to gamma radiation. (a) Protein interactions of DAPs related to DNA repair. (b) Proteins involved in sulfur metabolism were upregulated (orange) at 1 h of PIR. (c) Proteins involved in phenylalanine metabolism were downregulated (red) at 12 h of PIR.

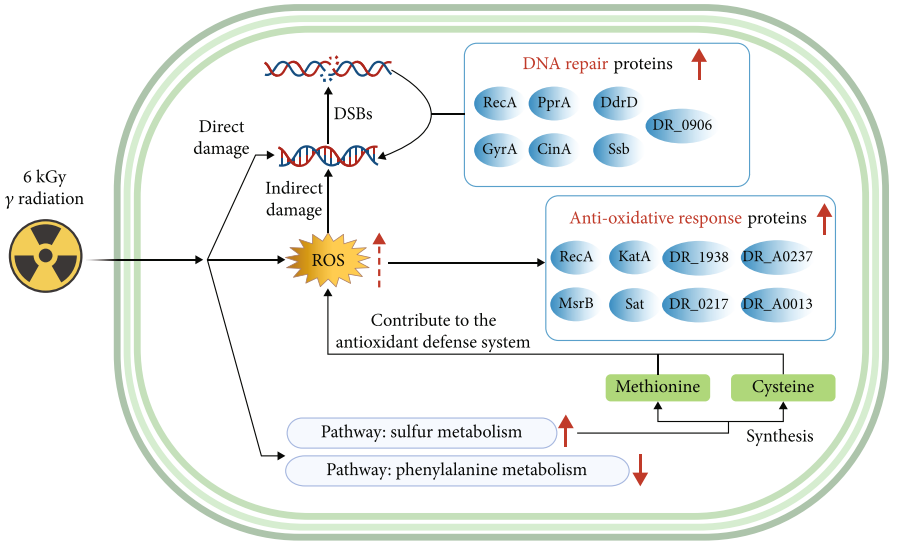

FIGURE 7: The proposed model elucidates the possible molecular mechanisms of robust radioresistance in *D. radiodurans*. Differentially abundant proteins in the blue ellipse are involved in DNA repair or antioxidative defense during PIR.

Cysteine biosynthesis by the sulfate assimilation pathway proceeds by intaking inorganic sulfate into the cell [37], and methionine synthesis is linked to cysteine synthesis [38]. Proteins involved in sulfur metabolism were highly overexpressed at 1 h. They reduce sulfate into sulfide to obtain energy, and sulfide is transferred to a serine moiety to produce cysteine. Meanwhile, methionine and cysteine, as sulfur-containing amino acids, greatly contribute to the antioxidant defense system and are key constituents in the regulation of cell metabolism. Sulfur metabolism plays significant roles in plant and bacterial oxidative stress tolerance [39–41], and we speculate that the overexpressed proteins also contribute to the antioxidative response. Further research is required to elucidate the relevance of these upregulated proteins (Figure 6).

Proteomic analysis also revealed that functional categories of phenylalanine metabolism were overrepresented in *D. radiodurans* during PIR at 12 h (Figure 6). These proteins participate in fatty acid metabolism and the phenylacetate degradation pathway, which are parts of phenylalanine metabolism. The decreased levels indicate the lower degradation of amino acids, which may be beneficial for protein synthesis and helpful for bacterial reproduction.

As shown in Figure 7, our findings showed multiple functional categories of differentially abundant proteins of *D. radiodurans* during PIR. Extensive research has found that the structure of DNA can be damaged directly by high-dose radiation directly or indirectly via consequent ROS accumulation [42, 43]. Thus, increased expression of proteins in the oxidative stress response and DNA repair system was observed. We hypothesized that the elevated level of sulfur metabolism might reduce ROS production and contribute to the antioxidant defense system, as differentially expressed proteins involved in the pathway also functioned in oxidative stress tolerance. Meanwhile, protein temporal dynamics also indicated different protein targets and protein regulation, as well as biological process to be protected at different time interval during PIR.

4. Conclusion

D. radiodurans is a robust bacterium with high resistance to irradiation. In this study, a comprehensive mapping of protein abundance dynamics during PIR was conducted to investigate its potential resistance capacity. The comparison between irradiation-treated cells and control cells showed a total of 413 DAPs. These proteins involved in DNA repair, antioxidative stress, sulfur metabolism, and phenylalanine metabolism. Several DAPs participated in DNA damage response during all the time intervals, and all the upregulated proteins were related to DNA repair, indicating its efficient DNA repair capacity after irradiation. In addition, proteins with antioxidative response showed upregulated at 1 h, 6 h, and 12 h of PIR. Moreover, proteins participate in sulfur metabolism were overexpressed at 1 h, while proteins related with phenylalanine metabolism were downregulated at 12 h of PIR. The expression level of proteins indicated that energy and material metabolism contribute to the response of *D. radiodurans* to gamma irradiation, and future experiments will be required to elucidate the molecular events.

Overall, these data revealed vivid temporal protein dynamics in *D. radiodurans* during PIR and provided insights to decipher molecular key components in dealing with increased ROS, which are helpful for understanding protein regulation in resistance to irradiation and may serve as a reference for radiation protection.

Data Availability

The mass spectrometry proteomics data have been deposited to the ProteomeXchange Consortium (http://proteomecentral.proteomexchange.org) via the PRIDE partner repository with the dataset identifier PXD027969.

Conflicts of Interest

The authors declare that they have no conflicts of interest.

Acknowledgments

This work was supported by the National Undergraduate Training Program for Innovation and Entrepreneurship of China (202010007748). We also gratefully acknowledge the support provided by the Analysis & Testing Center and Biological and Medical Engineering Core Facilities of Beijing Institute of Technology.

Supplementary Materials

Supplementary 1. Figure S1: growth curve of *D. radiodurans* after 6 kGy γ-irradiation. After irradiation, suspensions of the control and experimental groups were centrifuged (10000 × g, 5 min, 4°C) and transferred to fresh TGY at an initial OD600 of 0.1 to allow recovery. Cell turbidities were collected every 2 hours during PIR.

Supplementary 2. Tables S1-2: quantitative information across all samples.

Supplementary 3. Tables S3-7: differentially abundant proteins in the comparison control vs. radiation.

Supplementary 4. Table S8: protein IDs in clusters 1 and 2.

References

[1] K. W. Minton, "DNA repair in the extremely radioresistant bacterium Deinococcus radiodurans," *Molecular Microbiology*, vol. 13, no. 1, pp. 9–15, 1994.

[2] D. M. Sweet and B. E. Moseley, "Accurate repair of ultraviolet-induced damage in *Micrococcus radiodurans*," *Mutation Research*, vol. 23, no. 3, pp. 311–318, 1974.

[3] M. M. Cox and J. R. Battista, "*Deinococcus radiodurans*– the consummate survivor," *Nature Reviews. Microbiology*, vol. 3, no. 11, pp. 882–892, 2005.

[4] D. Slade and M. Radman, "Oxidative stress resistance in Deinococcus radiodurans," *Microbiology and Molecular Biology Reviews*, vol. 75, no. 1, pp. 133–191, 2011.

[5] H. Z. Qi, W. Z. Wang, J. Y. He, Y. Ma, F. Z. Xiao, and S. Y. He, "Antioxidative system of *Deinococcus radiodurans*," *Research in Microbiology*, vol. 171, no. 2, pp. 45–54, 2020.

[6] L. M. Markillie, S. M. Varnum, P. Hradecky, and K. K. Wong, "Targeted mutagenesis by duplication insertion in the radioresistant bacterium Deinococcus radiodurans: radiation sensitivities of catalase (katA) and superoxide dismutase (sodA) mutants," *Journal of Bacteriology*, vol. 181, no. 2, pp. 666–669, 1999.

[7] R. J. Dennis, E. Micossi, J. McCarthy et al., "Structure of the manganese superoxide dismutase from Deinococcus radiodurans in two crystal forms," *Acta Crystallographica Section F: Structural Biology and Crystallization Communications*, vol. 62, no. 4, pp. 325–329, 2006.

[8] M. Tanaka, I. Narumi, T. Funayama et al., "Characterization of pathways dependent on the uvsE, uvrA1, or uvrA2 gene product for UV resistance in Deinococcus radiodurans," *Journal of Bacteriology*, vol. 187, no. 11, pp. 3693–3697, 2005.

[9] N. P. Khairnar, V. A. Kamble, and H. S. Misra, "RecBC enzyme overproduction affects UV and gamma radiation survival of *Deinococcus radiodurans*," *DNA Repair*, vol. 7, no. 1, pp. 40–47, 2008.

[10] Y. Liu, J. Zhou, M. V. Omelchenko et al., "Transcriptome dynamics of Deinococcus radiodurans recovering from ionizing radiation," *Proceedings of the National Academy of Sciences of the United States of America*, vol. 100, no. 7, pp. 4191–4196, 2003.

[11] H. Luan, N. Meng, J. Fu et al., "Genome-wide transcriptome and antioxidant analyses on gamma-irradiated phases of Deinococcus radiodurans R1," *PLoS One*, vol. 9, no. 1, article e85649, 2014.

[12] C. Zhang, J. Wei, Z. Zheng, N. Ying, D. Sheng, and Y. Hua, "Proteomic analysis of Deinococcus radiodurans recovering from γ-irradiation," *Proteomics*, vol. 5, no. 1, pp. 138–143, 2005.

[13] B. Joshi, R. Schmid, K. Altendorf, and S. K. Apte, "Protein recycling is a major component of post-irradiation recovery in *Deinococcus radiodurans* strain R1," *Biochemical and Biophysical Research Communications*, vol. 320, no. 4, pp. 1112–1117, 2004.

[14] B. Basu and S. K. Apte, "Gamma radiation-induced proteome of *Deinococcus radiodurans* primarily targets DNA repair and oxidative stress alleviation," *Molecular & Cellular Proteomics*, vol. 11, no. 1, p. M111.011734, 2012.

[15] E. Ott, Y. Kawaguchi, D. Kölbl et al., "Proteometabolomic response of Deinococcus radiodurans exposed to UVC and vacuum conditions: initial studies prior to the Tanpopo space mission," *PLoS One*, vol. 12, no. 12, article e0189381, 2017.

[16] E. Ott, Y. Kawaguchi, N. Özgen et al., "Proteomic and metabolomic profiling of Deinococcus radiodurans recovering after exposure to simulated low earth orbit vacuum conditions," *Frontiers in Microbiology*, vol. 10, pp. 909–909, 2019.

[17] Y. Wang, P. Qin, J. Hong, N. Li, Y. Zhang, and Y. Deng, "Deep membrane proteome profiling of rat hippocampus in simulated complex space environment by SWATH," *Space: Science & Technology*, vol. 2021, article 9762372, 12 pages, 2021.

[18] F. Liu, R. Min, J. Hong, G. Cheng, Y. Zhang, and Y. Deng, "Quantitative proteomic analysis of ahpC/F and katE and katG knockout Escherichia coli—a useful model to study endogenous oxidative stress," *Applied Microbiology and Biotechnology*, vol. 105, no. 6, pp. 2399–2410, 2021.

[19] J. Yu and L. Lu, "BamA is a pivotal protein in cell envelope synthesis and cell division in *Deinococcus radiodurans*," *Biomembranes*, vol. 1861, no. 7, pp. 1365–1374, 2019.

[20] J. Li, Q. Li, X. Ma et al., "Biosynthesis of gold nanoparticles by the extreme bacterium *Deinococcus radiodurans* and an evaluation of their antibacterial properties," *International Journal of Nanomedicine*, vol. 11, pp. 5931–5944, 2016.

[21] S. Wang, W. Li, L. Hu, J. Cheng, H. Yang, and Y. Liu, "NAguideR: performing and prioritizing missing value imputations for consistent bottom-up proteomic analyses," *Nucleic Acids Research*, vol. 48, no. 14, pp. e83–e83, 2020.

[22] D. W. Huang, B. T. Sherman, and R. A. Lempicki, "Systematic and integrative analysis of large gene lists using DAVID bioinformatics resources," *Nature Protocols*, vol. 4, no. 1, pp. 44–57, 2009.

[23] R. D. Shereda, A. G. Kozlov, T. M. Lohman, M. M. Cox, and J. L. Keck, "SSB as an organizer/mobilizer of genome maintenance complexes," *Critical Reviews in Biochemistry and Molecular Biology*, vol. 43, no. 5, pp. 289–318, 2008.

[24] H. Lu, G. Gao, G. Xu et al., "*Deinococcus radiodurans* PprI switches on DNA damage response and cellular survival networks after radiation damage," *Molecular & Cellular Proteomics*, vol. 8, no. 3, pp. 481–494, 2009.

[25] D. Slade, A. B. Lindner, G. Paul, and M. Radman, "Recombination and replication in DNA repair of heavily irradiated *Deinococcus radiodurans*," *Cell*, vol. 136, no. 6, pp. 1044–1055, 2009.

[26] C. B. de la Tour, F. M. Passot, M. Toueille et al., "Comparative proteomics reveals key proteins recruited at the nucleoid of Deinococcus after irradiation-induced DNA damage," *Proteomics*, vol. 13, no. 23-24, pp. 3457–3469, 2013.

[27] I. Narumi, K. Satoh, S. Cui, T. Funayama, S. Kitayama, and H. Watanabe, "PprA: a novel protein from Deinococcus radiodurans that stimulates DNA ligation," *Molecular Microbiology*, vol. 54, no. 1, pp. 278–285, 2004.

[28] S. Kota, V. K. Charaka, and H. S. Misra, "PprA, a pleiotropic protein for radioresistance, works through DNA gyrase and shows cellular dynamics during postirradiation recovery in Deinococcus radiodurans," *Journal of Genetics*, vol. 93, no. 2, pp. 349–354, 2014.

[29] C. B. de la Tour, M. Mathieu, P. Servant, G. Coste, C. Norais, and F. Confalonieri, "Characterization of the DdrD protein from the extremely radioresistant bacterium Deinococcus radiodurans," *Extremophiles*, vol. 25, no. 4, pp. 343–355, 2021.

[30] S. Levin-Zaidman, J. Englander, E. Shimoni, A. K. Sharma, K. W. Minton, and A. Minsky, "Ringlike structure of the Deinococcus radiodurans genome: a key to radioresistance?," *Science*, vol. 299, no. 5604, pp. 254–256, 2003.

[31] B. Martin, P. Garcia, M. P. Castanié, and J. P. Claverys, "The recA gene of Streptococcus pneumoniae is part of a competence-induced operon and controls lysogenic induction," *Molecular Microbiology*, vol. 15, no. 2, pp. 367–379, 1995.

[32] H. R. Masure, B. J. Pearce, H. Shio, and B. Spellerberg, "Membrane targeting of RecA during genetic transformation," *Molecular Microbiology*, vol. 27, no. 4, pp. 845–852, 1998.

[33] W. Vogt, "Oxidation of methionyl residues in proteins: tools, targets, and reversal," *Free Radical Biology and Medicine*, vol. 18, no. 1, pp. 93–105, 1995.

[34] J. Gao, D. H. Yin, Y. Yao et al., "Loss of conformational stability in calmodulin upon methionine oxidation," *Biophysical Journal*, vol. 74, no. 3, pp. 1115–1134, 1998.

[35] B. Chen, L. M. Markillie, Y. Xiong, M. U. Mayer, and T. C. Squier, "Increased catalytic efficiency following gene fusion of bifunctional methionine sulfoxide reductase enzymes from

Shewanella oneidensis," *Biochemistry*, vol. 46, no. 49, pp. 14153–14161, 2007.

[36] C. Henry, L. Loiseau, A. Vergnes et al., "Redox controls RecA protein activity via reversible oxidation of its methionine residues," *eLife*, vol. 10, article e63747, 2021.

[37] M. A. Kertesz, "Riding the sulfur cycle – metabolism of sulfonates and sulfate esters in gram-negative bacteria," *FEMS Microbiology Reviews*, vol. 24, no. 2, pp. 135–175, 2000.

[38] F. C. Neidhart, J. L. Ingraham, K. B. Low, B. Magasanik, M. Schaechter, and H. E. Umbarger, "Escherichia coli and Salmonella: cellular and molecular biology," in *Biosynthesis of methionine*, ASM Press, Washington (DC), 2nd edition, 1996.

[39] N. A. Anjum, R. Gill, M. Kaushik et al., "ATP-sulfurylase, sulfur-compounds, and plant stress tolerance," *Plant Science*, vol. 6, no. 210, 2015.

[40] D. A. Podkopaeva, M. Grabovich, and G. A. Dubinina, "The functional role of reduced inorganic sulfur compounds in the metabolism of the microaerophilic bacterium Spirillum winogradskii," *Mikrobiologiia*, vol. 74, no. 1, pp. 17–25, 2005.

[41] R. Pinto, Q. X. Tang, W. J. Britton, T. S. Leyh, and J. A. Triccas, "The Mycobacterium tuberculosis cysD and cysNC genes form a stress-induced operon that encodes a tri-functional sulfate-activating complex," *Microbiology*, vol. 150, no. 6, pp. 1681–1686, 2004.

[42] J. Cadet and J. R. Wagner, "DNA base damage by reactive oxygen species, oxidizing agents, and UV radiation," *Cold Spring Harbor Perspectives in Biology*, vol. 5, no. 2, article a012559, 2013.

[43] M. E. Lomax, L. K. Folkes, and P. O'Neill, "Biological consequences of radiation-induced DNA damage: relevance to radiotherapy," *Clinical Oncology*, vol. 25, no. 10, pp. 578–585, 2013.

Hindawi
Oxidative Medicine and Cellular Longevity
Volume 2022, Article ID 3403009, 19 pages
https://doi.org/10.1155/2022/3403009

Research Article

Glutamine Transporter SLC1A5 Regulates Ionizing Radiation-Derived Oxidative Damage and Ferroptosis

Zhuhui Yuan,[1] **Tong Liu**,[2,3] **Xiao Huo**,[2,3] **Hao Wang**,[1] **Junjie Wang**,[1] **and Lixiang Xue**[2,3]

[1]*Department of Radiation Oncology, Peking University Third Hospital Cancer Center, Peking University Third Hospital, Haidian District, 49 Huayuan North Road, Beijing, China*
[2]*Center of Basic Medical Research, Institute of Medical Innovation and Research, Peking University Third Hospital Cancer Center, Peking University Third Hospital, Haidian District, 49 Huayuan North Road, Beijing 100191, China*
[3]*Biobank, Peking University Third Hospital Cancer Center, Peking University Third Hospital, Haidian District, 49 Huayuan North Road, Beijing 100191, China*

Correspondence should be addressed to Junjie Wang; junjiewang@pku.edu.cn and Lixiang Xue; lixiangxue@hsc.pku.edu.cn

Received 23 August 2022; Revised 13 September 2022; Accepted 21 September 2022; Published 10 October 2022

Academic Editor: Bing Wang

Ionizing radiation-derived oxidative stress and ferroptosis are one of the most important biological effects on destroying the liver tumor, whereas radioresistance of liver tumor remains a leading cause of radiotherapy (RT) failure mainly because of the protective antiferroptosis, in which oxidative stress and subsequent lipid peroxidation are the key initiators. Thus, it is of great importance to overcome ferroptosis resistance to improve the therapeutic efficacy of RT in liver tumor patients. Irradiation-resistant HepG2 cells (HepG2-IRR) were established by long-term exposure to X-ray (2 to 8 Gy), and targeted metabolomics analysis revealed an obvious increase in intracellular amino acids in HepG2-IRR cells upon ferroptosis stress. Among these amino acids with obvious changes, N-acetylglutamine, a derivative of glutamine, is essential for the redox homeostasis and progression of tumor cells. Interestingly, the treatment of glutamine starvation could promote the ferroptosis effect significantly, whereas glutamine supplementation reversed the ferroptosis effect completely. Consistent with the changes in amino acids pattern, the glutamine transporter SLC1A5 was verified in liver tumor samples from TCGA training and validation cohorts as an independent prognostic amino acid-ferroptosis gene (AFG). A risk score for screening prognosis based on the SLC1A5, SLC7A11, ASNS, and TXNRD1 demonstrated that a high-risk score was correlated with poor survival. *In vitro* studies had shown that the knockdown of SLC1A5 resulted in a significant decrease in cell viability and promoted lipid peroxidation and oxidative damage introduced by irradiation (10 Gy). Collectively, our findings indicated that SLC1A5 may act as a suppressor gene against ferroptosis and can be a potential target for ionizing radiation mediated effects.

1. Introduction

Oxidative stress is one of the most important mechanisms of ionization-induced cell damage, and ferroptosis, which is triggered by oxidative stress, has been identified as a crucial mechanism involved in tumor progression and radiosensitivity [1–3]. Recently, it has been found that ferroptosis can improve radiosensitivity *in vivo* and *in vitro* [4–8]. Specifically, the type of amino acid transporters expressed in tumor cells has been widely explored in regulating ferroptosis-related radiosensitivity [4–6, 9, 10]. The Xc- transport system that carries cysteine to synthesize glutathione (GSH) for controlling intracellular redox homeostasis and defending against ferroptosis [11] has been considered an important molecular mechanism of radioresistance. The regulation of glutamine decomposition may have an impact on the susceptibility of cells to ferroptosis. The most favorable evidence is that glutamine synthase 2 (GLS2) boosts ferroptosis by facilitating the conversion of glutamate to α-ketoglutarate [12]. In addition, reductive glutamine

metabolism is stimulated by the mTOR/PGC-1/SIRT3 pathway, one of the key signals in carcinogenesis, to decrease the oxidative stress [13]. Aberrant glutamine metabolism can act as a biological target for the radiosensitization of tumors [14]. Thus, the mechanisms of intracellular oxidative stress management upon ferroptosis activation tend to be important issues affecting radiosensitivity. The effects of amino acid metabolism implicated in redox and ferroptosis on radiosensitization require to be paid more attention.

In liver tumor, metabolic reprogramming results in tumor aggressiveness, rapid progression, and radioresistance. Amino acid metabolism and redox homeostasis, which support the requirements of exponential growth and proliferation, are critical for metabolic reprogramming [15]. According to recent studies, amino acid-derived metabolites were oncogenic in the liver. Glutamine is the predominant ingredient for nucleotide synthesis and protein synthesis, both of which are necessary for tumor cell proliferation and energy supply. Moreover, it is reported that glutamine can facilitate tumor cells to defend against oxidative stress and ferroptosis [16]. Using pharmacological approaches targeting glutamine uptake or utilization could trigger ferroptotic cell death and suppress cancer cell growth [17, 18]. However, it is still not clear which targets or pathways of amino acid metabolism are involved in ferroptosis and thereby impact irradiation response in liver tumor.

In this study, we first proved the presence of ferroptosis resistance and increased amino acid metabolism in innate or acquired radioresistant liver tumor cells. Secondly, ferroptosis was considerably promoted in liver tumor cells by glutamine starvation, whereas this effect was rescued by supplementing with glutamine. SLC1A5, as the glutamine transporter, was screened out to regulate ferroptosis response in liver tumor cell lines. Finally, through a variety of *in vitro* experiments, we identified the tumorigenic functions of SLC1A5 as well as its suppressive impact on oxidative stress-induced ferroptosis and RT. The clinical prognosis of liver tumor patients could be predicted using a risk signature based on SLC1A5-related genes. Overall, SLC1A5 may serve as a novel predictive biomarker and a possible therapeutic target for liver tumor patients who are treated with radiotherapy. Our research opens a new avenue for the treatment of radiotherapy-resistant liver tumor in patients with differential SLC1A5 expression in the future.

2. Methods and Materials

2.1. Reagents. The DMEM high-glucose culture medium was purchased from HyClone (Cat# SH30023.01), and fetal bovine serum was purchased from Gibco (Cat# 10099141). Trypsin was purchased from Invitrogen (Cat# 25200072). Erastin was obtained from Millipore (Cat# 329600). RSL3 (Cat# S8155), liproxstatin-1 (Cat# S7699), and ferrostatin-1 (Cat# S7243) were obtained from Selleck.

2.2. Cell Culture. Cells, including HepG2, SMMC-7721, Huh7, Huh6, and HT1080, were cultured in DMEM medium supplemented with 10% FBS, 100 IU penicillin, and 100 μg/ml streptomycin and incubated at 37°C in a 5% CO_2 humidified incubator.

2.3. Establishment of Radioresistant Liver Tumor Cell Line. Exponentially growing HepG2 cells were irradiated with 2, 4, 6, and 8 Gray (Gy) at a dose rate of 6 Gy/min. The radiation field was $10 * 10$ cm. The surviving sublines (HepG2-IRR) were then passaged at 37°C.

2.4. Targeted Metabolomics Analysis. Radioresistant HepG2 cells were exposed to oxidative stress by adding Erastin (50 μM) for 6 hours. Cells ($1.2 * 10^7$) were collected. Targeted metabolomics analysis was performed using the Q300 Kit (Metabo-Profile, Shanghai, China) as described previously [19]. Briefly, ultraperformance liquid chromatography coupled to a tandem mass spectrometry (UPLC-MS/MS) system (ACQUITY UPLC-Xevo TQ-S, Waters Corp., Milford, MA, USA) was used to quantitate all targeted metabolites in this study. The details of the untargeted metabolomics analysis are listed in Supplementary file 1.

2.5. Lipid Peroxidation Assay. Cells ($2.5 * 10^5$/well) were seeded in triplicate in 6-well plates 24 hours before treatment, pretreated with or without erastin for 24 h, and then irradiated with 10 Gy at a dose rate of 6 Gy/min. Fresh media containing 0.1X BODIPY 581/591 C11 dye (Abcam, Cat# ab243377) was added to each well after the cells had been treated for 24 hours. The cells were rinsed with PBS and trypsinized to obtain a cell suspension after incubation for 20 minutes in a humidified incubator (at 37°C, 5% CO_2). Lipid peroxidation levels were analyzed by flow cytometry using a Beckman Coulter CytoFLEX™ (CytoFLEX) and analyzed with FlowJo software.

2.6. Quantitative Real-Time Polymerase Chain Reaction (qRT-PCR). Total RNA was extracted according to the manufacturer's instructions using TRIzol® reagent (Invitrogen, Cat# 15596018). The HiScript III 1st Strand cDNA Synthesis Kit (Vazyme, Cat# R312-01) was used to reverse transcribe 1 g total RNA into single-strand complementary DNA (cDNA). Following the manufacturer's procedures, RT-qPCR was done in triplicate using SYBR Green PCR Master Mix. GAPDH was used as a reference to standardize the relative expression levels of SLC1A5. The $2^{-\Delta\Delta Ct}$ method was used to calculate gene expression. The sequences of the primers used for RT-qPCR were listed as follows:

(1) SLC1A5 forward: GTGTCCTCACTCTGGCCATC

(2) SLC1A5 reverse: CCCAGAGCGTCACCTTCTAC

2.7. CCK8 Assay. Cells ($1 * 10^4$/well) were seeded into 96-well plates. To determine the effect of treatment on cell viability, a 10% volume of CCK8 (Dojindo Laboratories, Cat# CK04) was added directly into the medium and incubated for 3 hours. Absorbance at wavelengths of 450 nm was measured. Results were normalized to untreated controls and shown as relative cell viability (%).

2.8. Data and Resources. The RNA-Seq data and clinical information for the liver hepatocellular carcinoma (LIHC)

Table 1: The clinical characteristics of liver tumor patients from TCGA dataset.

Characteristics	Training ($n = 168$)	Validation ($n = 166$)	Total ($n = 334$)	p value
Age				
Mean ± SD	59.45 ± 12.98	58.98 ± 13.69	59.21 ± 13.32	
Gender				1.00
FEMALE	53 (15.87%)	52 (15.57%)	105 (31.44%)	
MALE	115 (34.43%)	114 (34.13%)	229 (68.56%)	
Grade				0.94
G1	27 (8.08%)	25 (7.49%)	52 (15.57%)	
G2	80 (23.95%)	76 (22.75%)	156 (46.71%)	
G3	53 (15.87%)	56 (16.77%)	109 (32.63%)	
G4	5 (1.50%)	7 (2.10%)	12 (3.59%)	
Unknown	3 (0.90%)	2 (0.60%)	5 (1.50%)	
Stage				0.46
Stage I	80 (23.95%)	78 (23.35%)	158 (47.31%)	
Stage II	31 (9.28%)	43 (12.87%)	74 (22.16%)	
Stage III	3 (0.90%)	0 (0.0e+0%)	3 (0.90%)	
Stage IIIA	31 (9.28%)	28 (8.38%)	59 (17.66%)	
Stage IIIB	3 (0.90%)	4 (1.20%)	7 (2.10%)	
Stage IIIC	6 (1.80%)	3 (0.90%)	9 (2.69%)	
Stage IV	1 (0.30%)	0 (0.0e+0%)	1 (0.30%)	
Stage IVB	1 (0.30%)	1 (0.30%)	2 (0.60%)	
Unknown	12 (3.59%)	9 (2.69%)	21 (6.29%)	
T				0.28
T1	86 (25.75%)	79 (23.65%)	165 (49.40%)	
T2	32 (9.58%)	47 (14.07%)	79 (23.65%)	
T2a	1 (0.30%)	0 (0.0e+0%)	1 (0.30%)	
T2b	0 (0.0e+0%)	1 (0.30%)	1 (0.30%)	
T3	23 (6.89%)	20 (5.99%)	43 (12.87%)	
T3a	16 (4.79%)	8 (2.40%)	24 (7.19%)	
T3b	1 (0.30%)	4 (1.20%)	5 (1.50%)	
T4	7 (2.10%)	6 (1.80%)	13 (3.89%)	
TX	1 (0.30%)	0 (0.0e+0%)	1 (0.30%)	
Unknown	1 (0.30%)	1 (0.30%)	2 (0.60%)	
M				0.83
M0	120 (35.93%)	121 (36.23%)	241 (72.16%)	
M1	2 (0.60%)	1 (0.30%)	3 (0.90%)	
MX	46 (13.77%)	44 (13.17%)	90 (26.95%)	
N				0.24
N0	115 (34.43%)	119 (35.63%)	234 (70.06%)	
N1	3 (0.90%)	0 (0)	3 (0.90%)	
NX	50 (14.97%)	46 (13.77%)	96 (28.74%)	
Unknown	0 (0)	1 (0.30%)	1 (0.30%)	

project were derived from TCGA (https://portal.gdc.cancer.gov/, updated time of datasets: 20200814). We downloaded RNA-Seq data expressed as fragments per kilobase of exon per million reads mapped (FPKM) from TCGA database. Ensembl IDs were transformed into gene symbols. The median value was used as the gene symbol's expression profile when more than one ensemble ID matched the same gene symbol. The mRNA data of TCGA dataset contains 374 tumor samples and 50 normal samples. Tumor samples with missing clinical data or follow-up periods < 6 months were censored, and the remaining tumor sample in TCGA dataset was 334. Table 1 displays the clinical features of the liver tumor patients in TCGA. For gene expression analysis, All TCGA liver tumor patients were randomly divided into training cohort (number of patients: 168) and validation cohort (number of patients: 166). The patients in the

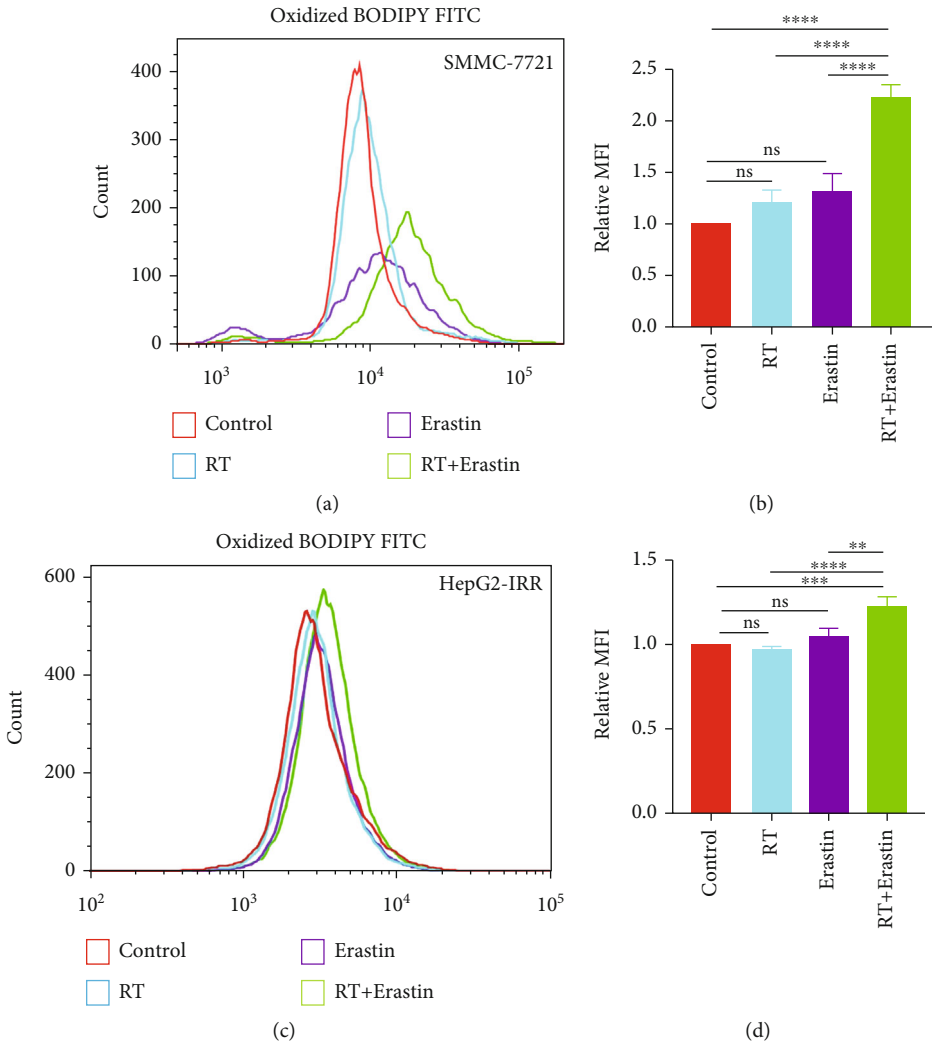

Figure 1: Continued.

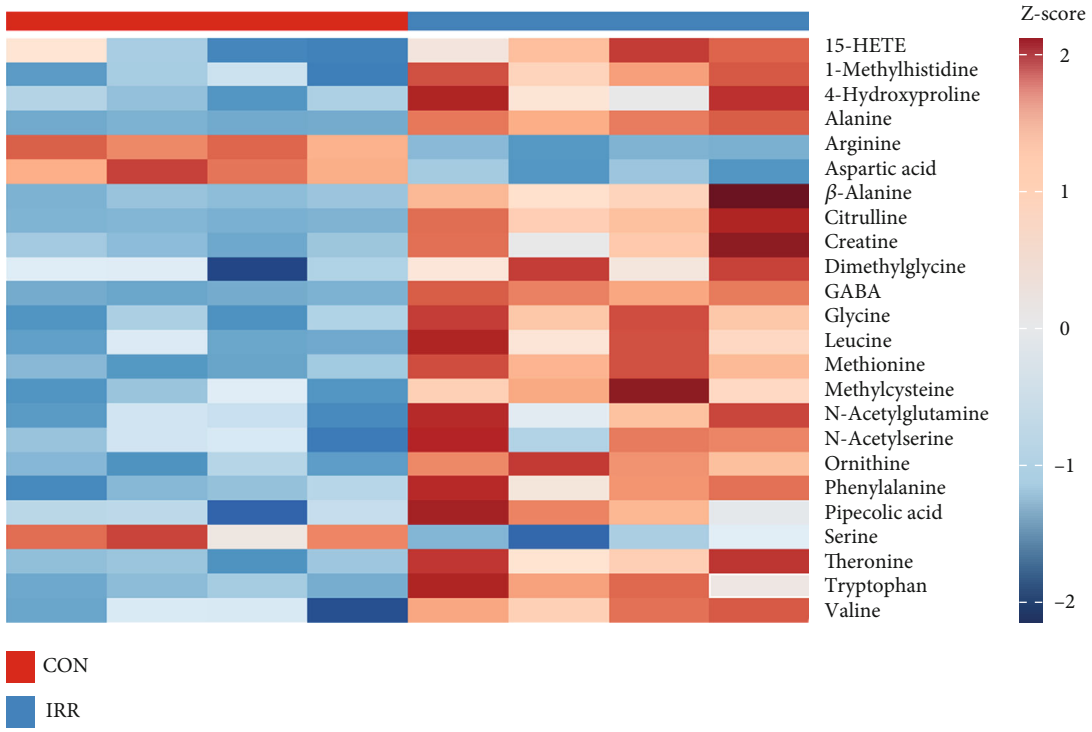

(e)

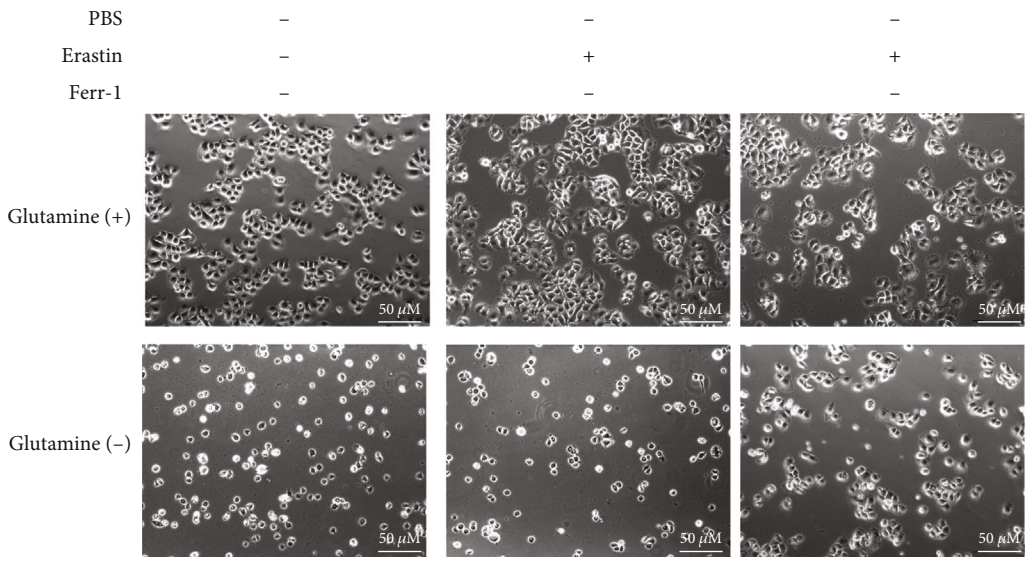

(f)

Figure 1: Continued.

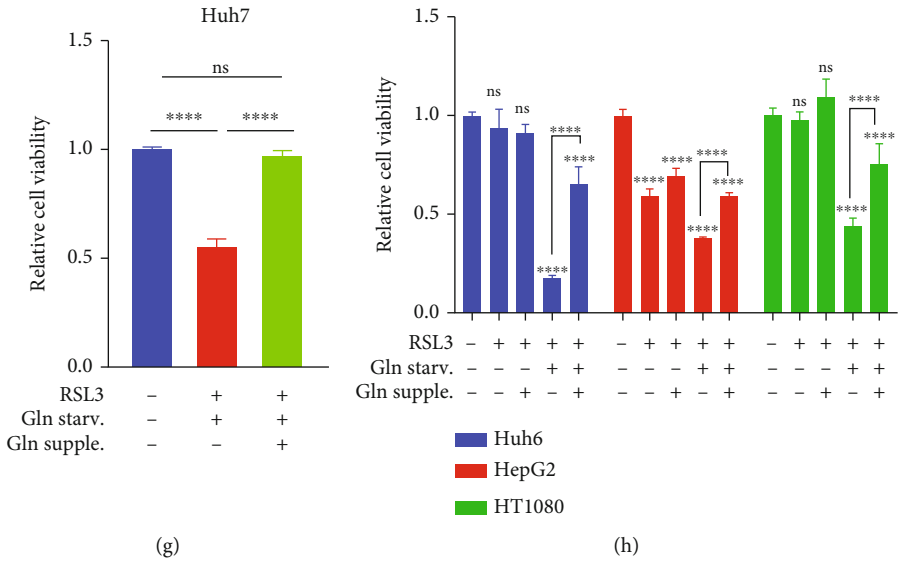

Figure 1: A combination of RT and ferroptosis inducer promotes ferroptotic cell death in the liver tumor cell lines. (a, b) Flow cytometry revealed a significant increase in normalized MFI of lipid peroxidation in SMMC-7721 cells treated with RT (8 Gy) after pretreatment with erastin (25 μM). (c, d) In HepG2-IRR cells, RT (8 Gy) in combination with Erastin (25 μM) enhances the normalized MFI of lipid peroxidation as determined by flow cytometry. (e) After Erastin (25 μM) stimulation, the hierarchical clustering of targeted metabolic comparing HepG2-IRR cells and wild-type HepG2 cells indicates a noticeable increase in amino acid content. (f) Glutamine is essential for SMMC-7721 cell survival, and glutamine starvation induces ferroptosis in SMMC-7721 cells which can be reversed by ferr-1. Erastin: 25 μM; Ferr-1: 1 μM. Magnification: 20X; scale bar: 50 μM. (g, h) The sensitized ferroptosis effect of glutamine deprivation is reversed by glutamine supplementation. Huh7, Huh6, HepG2, and HT1080 cell lines are more susceptible to ferroptotic cell death after being treated with RSL3 (2.5 μM) and glutamine deprivation for 24 hours, and glutamine supplementation can entirely reverse this effect. Abbreviations: RT: radiotherapy; IRR: irradiation-resistant; MFI: mean fluorescence intensity; AFGs: amino acid-ferroptosis genes. $^{*}p < 0.05$; $^{**}p < 0.01$; $^{***}p < 0.001$; $^{****}p < 0.0001$.

training and validation cohort were further divided into the high- and low-risk groups based on the median value of the risk score. The RNA-Seq data of GSE94550 and GSE123062 were derived from GEO datasets (https://www.ncbi.nlm.nih.gov/geo/) and analyzed with GEO2R (https://www.ncbi.nlm.nih.gov/geo/geo2r/, adjust p value less than 0.05 were considered differentially expressed).

2.9. Cox Regression Analysis. Cox regression analysis was performed with the "survival" package in R using TCGA datasets. The AFGs that differed in expression between tumor tissue and its surrounding normal tissues and had p values less than 0.05 were classified as prognostic related-amino acid-ferroptosis genes (AFGs).

2.10. Statistical Analysis. Statistical analysis was performed using R (version 3.6.3, http://www.r-project.org/) and GraphPad Prism 8.0 (GraphPad Prism Software Inc., San Diego, CA, USA). Unpaired Student's t-tests or one-way analyses of variance with a Bonferroni post hoc test for multiple group comparisons were used to identify significant differences between the groups. $p < 0.05$ was a statistically significant difference. For mRNA seq data from TCGA, genes with $|\log FC| \geq 1$ and FDR < 0.05 (FC means fold change; FDR means false discovery rate) were considered significantly differentially expressed.

3. Results

3.1. The Content of Amino Acids Is Increased in Radioresistant Liver Tumor Cells upon Oxidative Stress. Since irradiation can give rise to ferroptosis to eliminate tumor cells, we first sought to detect if the innate or acquired resistance of liver tumor cells to irradiation could attenuate ferroptosis stress. HepG2 and SMMC-7721 cell lines are commonly utilized liver tumor cell lines in radiobiological and ferroptosis studies [20, 21]. As shown in Figures 1(a)–1(d), RT or Erastin (one of the commonly used ferroptosis inducers) alone increased the mean fluorescence intensity (MFI) of lipid peroxidation (LPO) slightly, a standard marker of ferroptosis activation detected by BODIPY581/591 probe [22], whereas the combination of RT and Erastin increased MFI significantly in SMMC-7721 cells and radioresistant HepG2 cells (HepG2-IRR) which we had reported previously [23]. These findings suggested that liver tumor cells, whether they have intrinsic or acquired radioresistance, display limited sensitivity to ferroptosis stress; however, liver tumor cells' response to ferroptosis can be improved by amplifying ferroptosis stress, such as utilizing a combination method. Therefore, to improve the clinical outcome of liver tumor patients receiving RT, it is essential to explore the critical factor(s) that have an impact on ferroptosis response.

The transportation and *in vivo* utilization of amino acids play a significant role in ferroptosis and RT response as

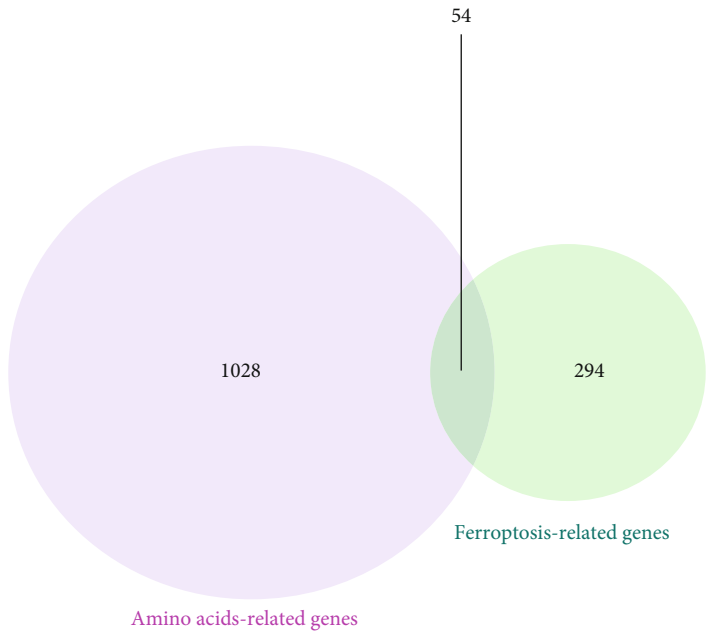

(a)

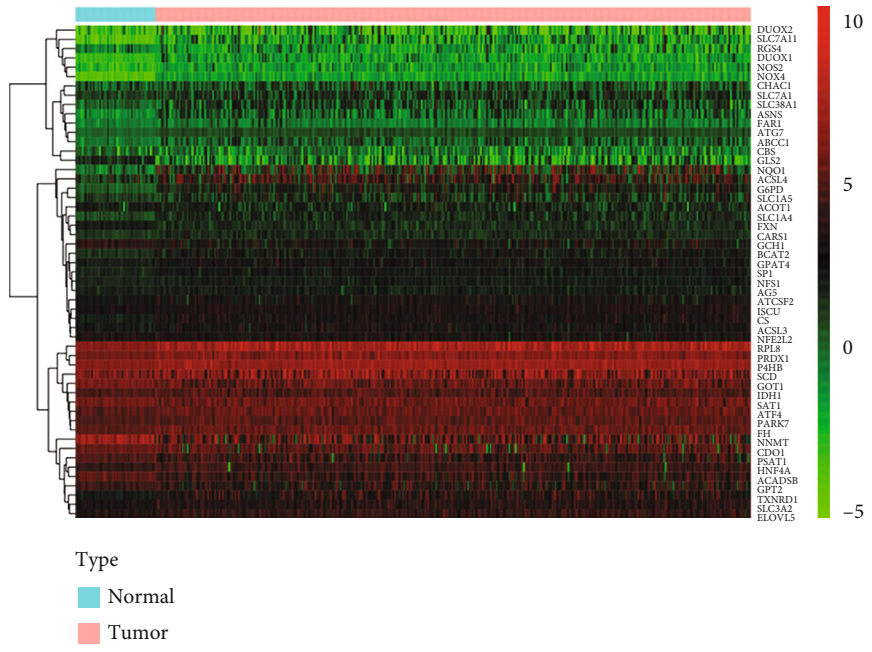

(b)

Figure 2: Continued.

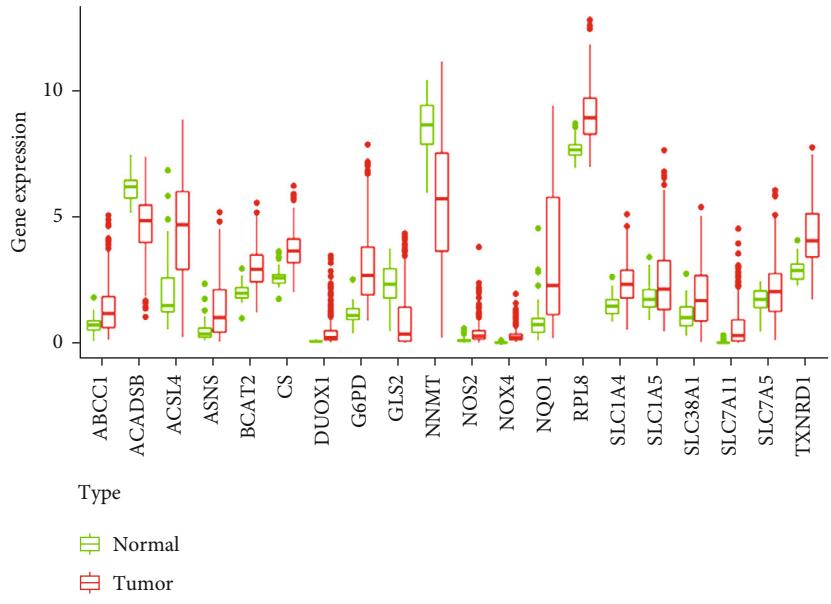

(c)

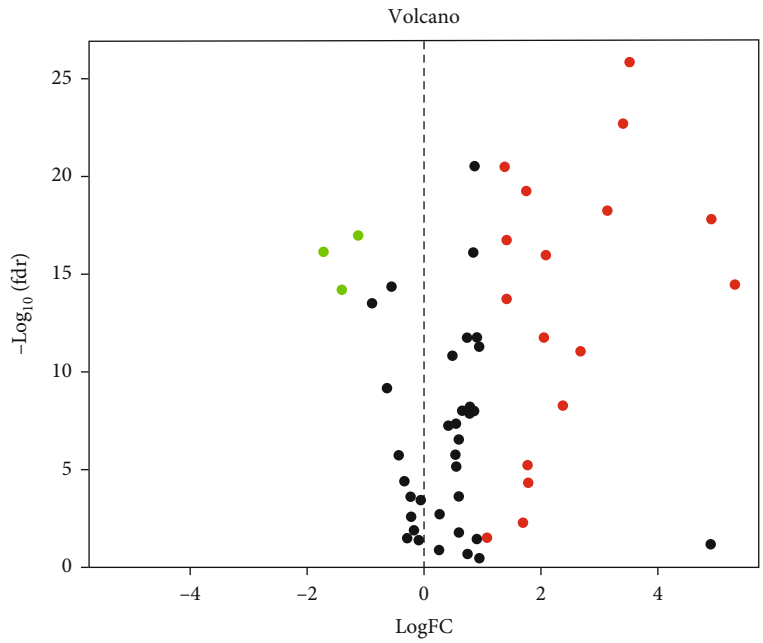

(d)

Figure 2: Continued.

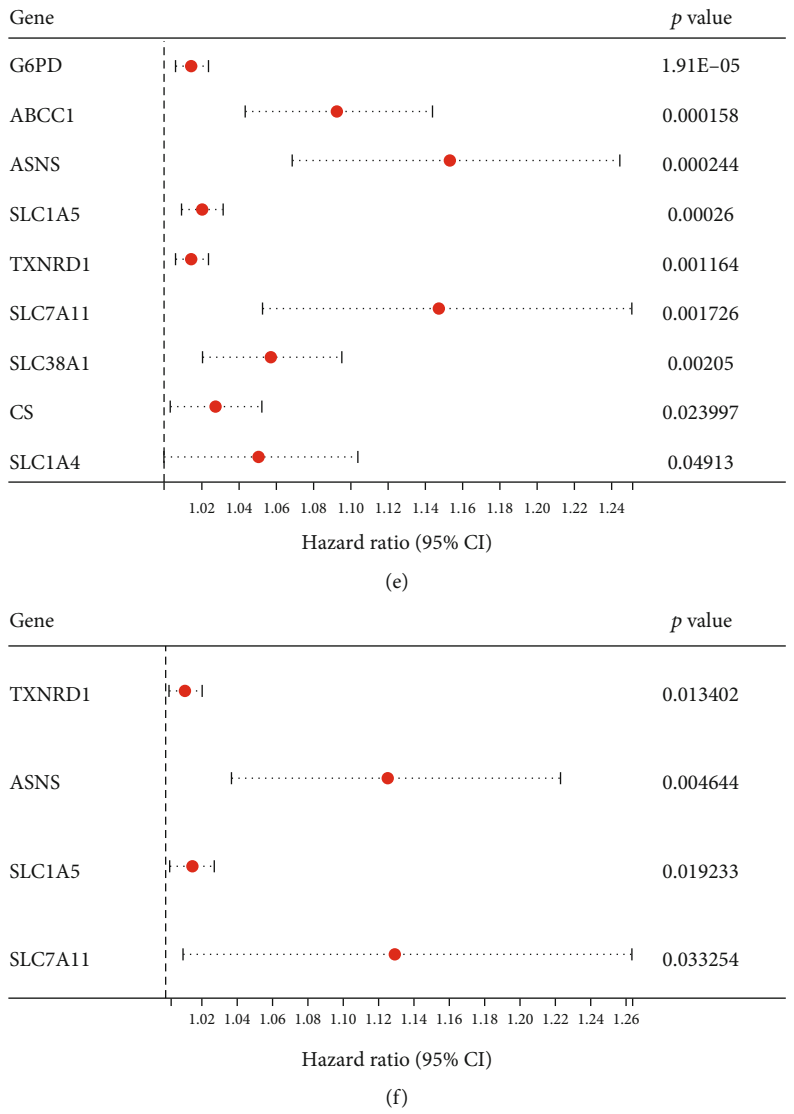

Figure 2: The expression of thirty-four intersecting genes in the tumor and surrounding normal tissues of the liver. (a) Venn diagram indicates 54 intersecting genes (AFGs) involved in both ferroptosis and amino acid metabolism. (b) Hierarchical clustering of the 54 intersecting genes in liver tumor tissue and normal tissue from TCGA database. (c) The expression difference of the 54 intersecting genes between liver tumor tissue and normal tissues is depicted by a volcano heat map. A total of 20 intersecting genes shows a significant difference. The intersecting genes with increasing levels in tumor tissues are shown in the right panel (red), whereas the intersecting genes with lower levels in tumor tissues are shown in the left panel (green). (d) The expression of the 20 AFGs in tumor and normal tissues of the liver. (e) The findings of the univariate Cox regression analysis between 20 AFG expressions and OS is shown in forest plots. Nine genes correlated with OS are detected. There are 3 downregulated DEGs (NNMT, GLS2, and ACADSB) and 17 upregulated DEGs (SLC1A5, SLC1A4, SLC7A11, etc.). (f) Multivariate Cox analysis shows eight AFGs negatively correlated with OS in liver tumor. AFGs: amino acid-ferroptosis genes.

known. To verify whether amino acid metabolism alterations have an impact on ferroptosis and RT response in liver tumor cells, we performed targeted metabolomics to evaluate significantly altered metabolites. Upon treatment of Erastin, targeted metabolomics revealed that the content of amino acids (AA) differed significantly in HepG2-IRR cells (FDR-corrected $p < 0.05$; FC > 1.5) compared to wild-type HepG2 cells (Supplementary Figure S1), especially N-acetylglutamine, glycine, leucine, methionine, threonine, tryptophan, and valine (Figure 1(e)). N-acetylglutamine is a derivative of glutamine, and glutamine is essential for the proliferation and development of tumor cells. Consistent with this, SMMC-7721 cells survived in the absence of glutamine either in the ferroptosis condition or the basal condition (Figure 1(f)), and this effect was significantly reversed by a ferroptosis-specific inhibitor (Ferr-1). Additionally, compared to another commonly used ferroptosis inducer—RSL3, glutamine deprivation combined with RSL3 significantly promoted ferroptotic cell death, and glutamine supplementation significantly

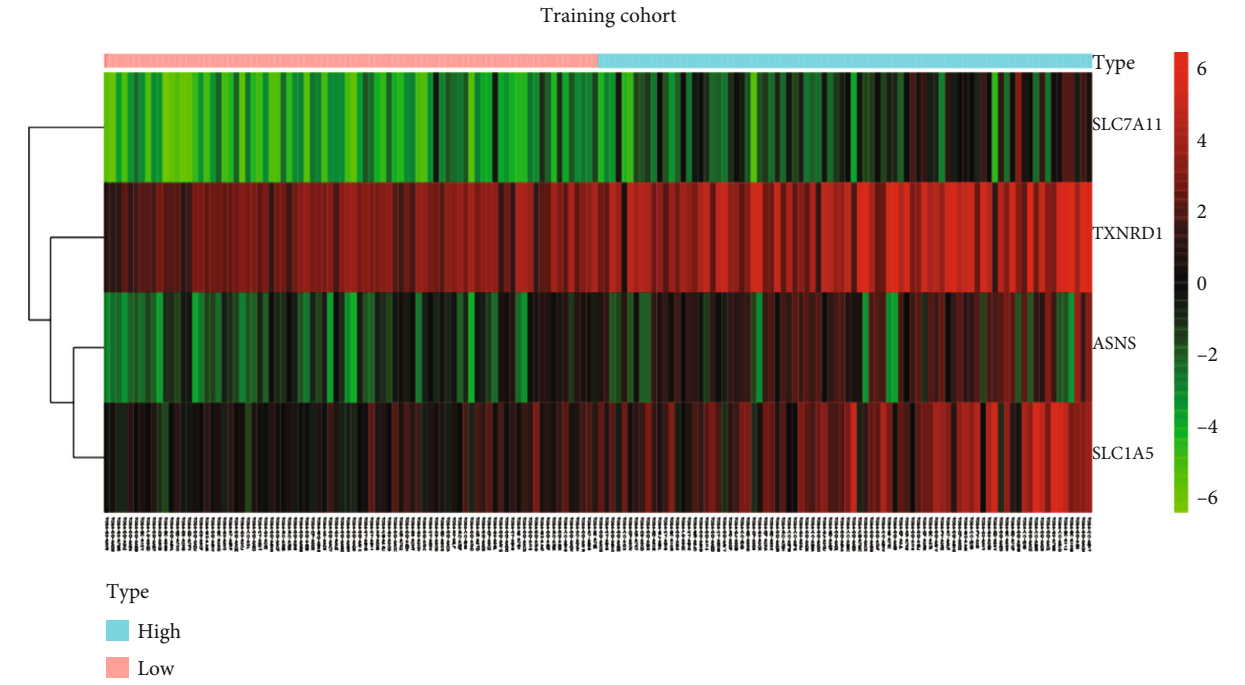

(a)

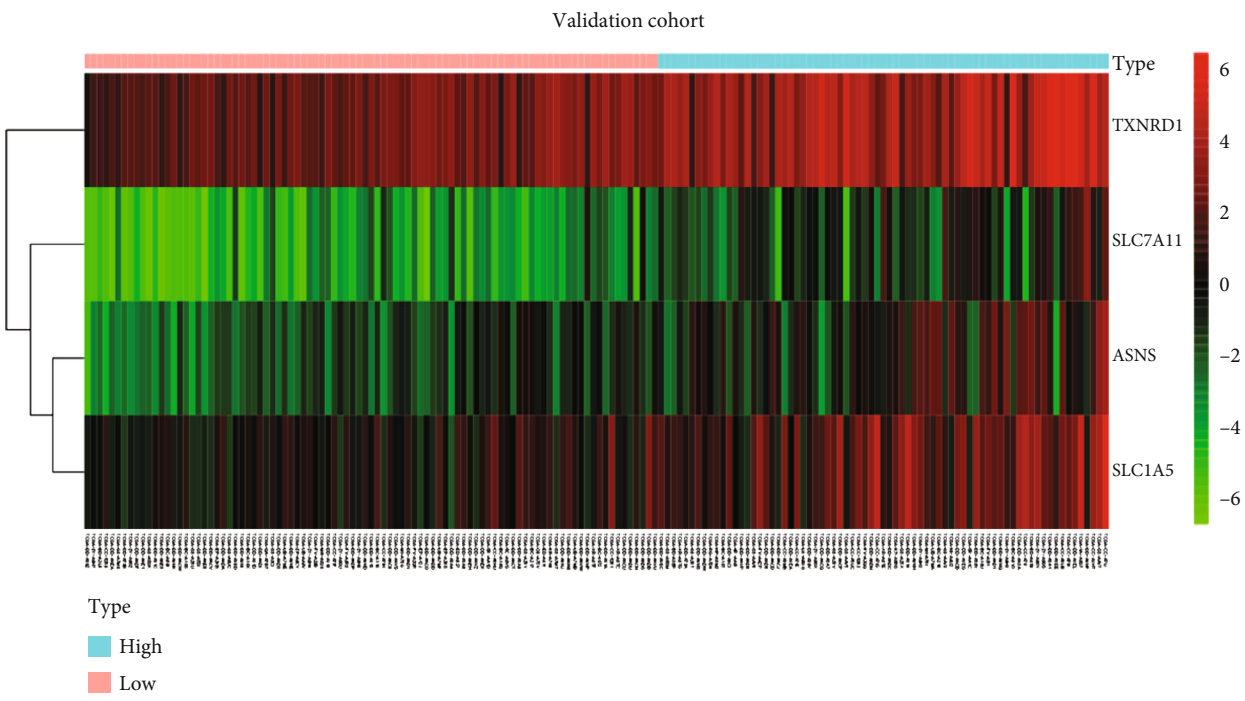

(b)

Figure 3: Continued.

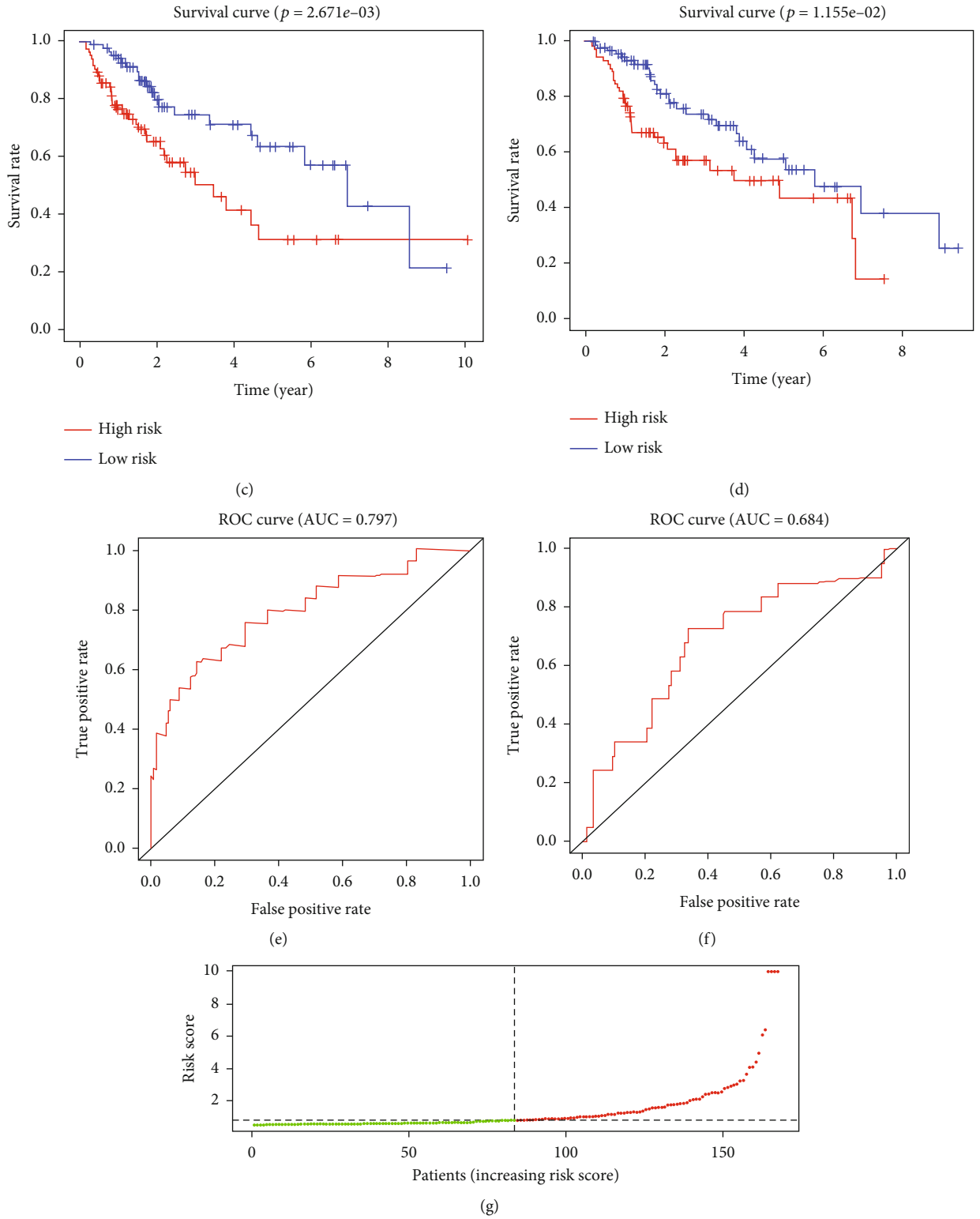

Figure 3: Continued.

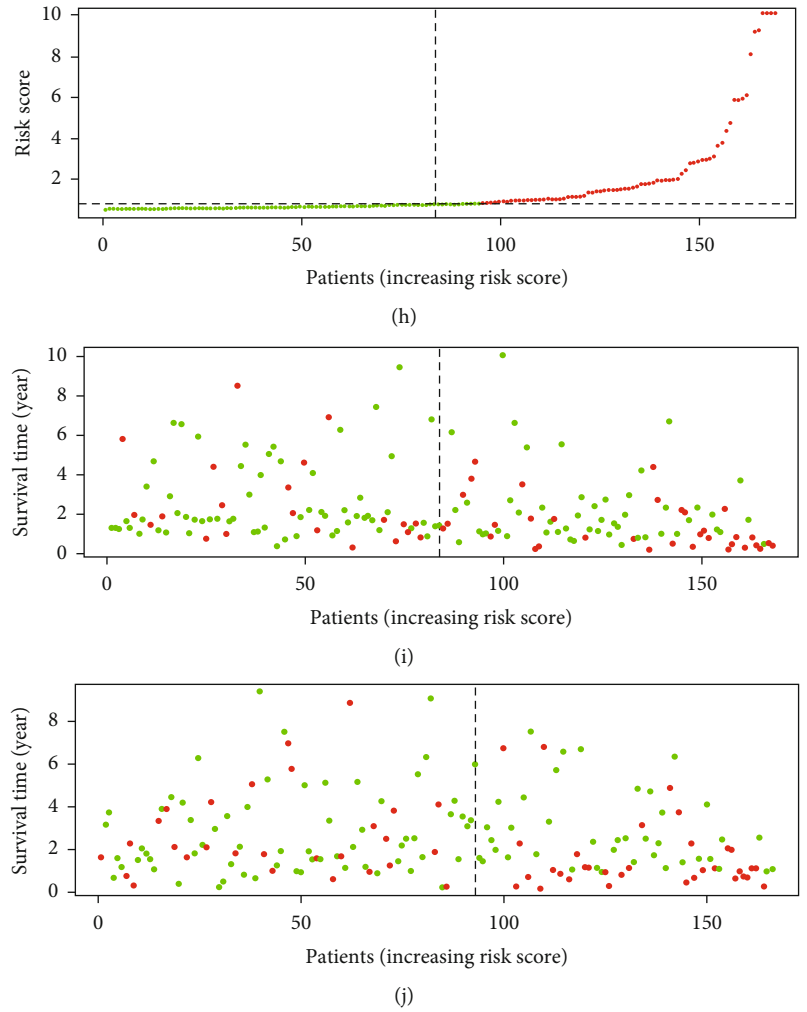

Figure 3: liver tumor patients with a high-risk score suggest a lower RT response and a higher survival risk, compared with liver tumor patients with a low-risk score. (a, b) According to the results of cox regression, 4 AFGs are screened to establish a prognostic model. The 4 AFGs are all highly expressed in liver tumor tissues. (c, d) Kaplan-Meier survival curves comparing liver tumor patients' OS based on the expression of the five AFGs indicate that the five AFGs are negatively associated with OS in liver tumor. The Kaplan-Meier graphs demonstrate the difference in OS between the high-risk and low-risk groups in the training cohort (a) and validation cohort (b). Patients in the high-risk group show poor survival compared with low-risk group patients. AUC of time-dependent ROC curves verifies the prognostic performance of the risk score in the training cohort (e) and validation cohort (f). The distribution and median value of the risk scores in the training cohort (g) and validation cohort (h). The distributions of OS status, OS, and risk score in the training cohort (i) and validation cohort (j). AFGs: amino acid-ferroptosis genes.

reversed ferroptotic cell death triggered by the combination of glutamine deprivation and RSL3 (Figures 1(g) and 1(h)). These findings strongly indicated that glutamine is required for tumor cell proliferation and that glutamine deficiency can lead to ferroptotic cell death [24].

3.2. Glutamine Membrane Transporter SLC1A5 Is Upregulated in Liver Tumor and Indicates a Poor Prognosis. To validate the effect of glutamine on ferroptosis and explore the intrinsic origins, we next downloaded the transcriptome data of liver tumor and the corresponding clinical data from TCGA database to detect the potential regulated gene for amino acid metabolism-mediated ferroptosis response.

Firstly, to obtain the list of the genes involved in both amino acid metabolism and ferroptosis, we merged the ferroptosis genes (Supplementary file 2) from FerrDb databases and amino acid metabolism-related genes (Supplementary file 3) from the GSEA datasets. The Venn diagram suggested 54 genes associated with amino acid metabolism related-ferroptosis genes (AFGs) (Figure 2(a)). The expression of the 54 genes between liver tumor tissues and surrounding normal tissues in TCGA dataset is shown in Figure 2(b). According to the threshold of logFC ($|\log FC| \geq 1$) and FDR (FDR < 0.05), 20 AGFs were expressed differentially (DEGs, Figures 2(c) and 2(d) and Supplementary file 4): there were 3 downregulated DEGs (NNMT, GLS2, and ACADSB) and 17 upregulated DEGs (SLC1A5, SLC1A4, SLC7A11, etc.).

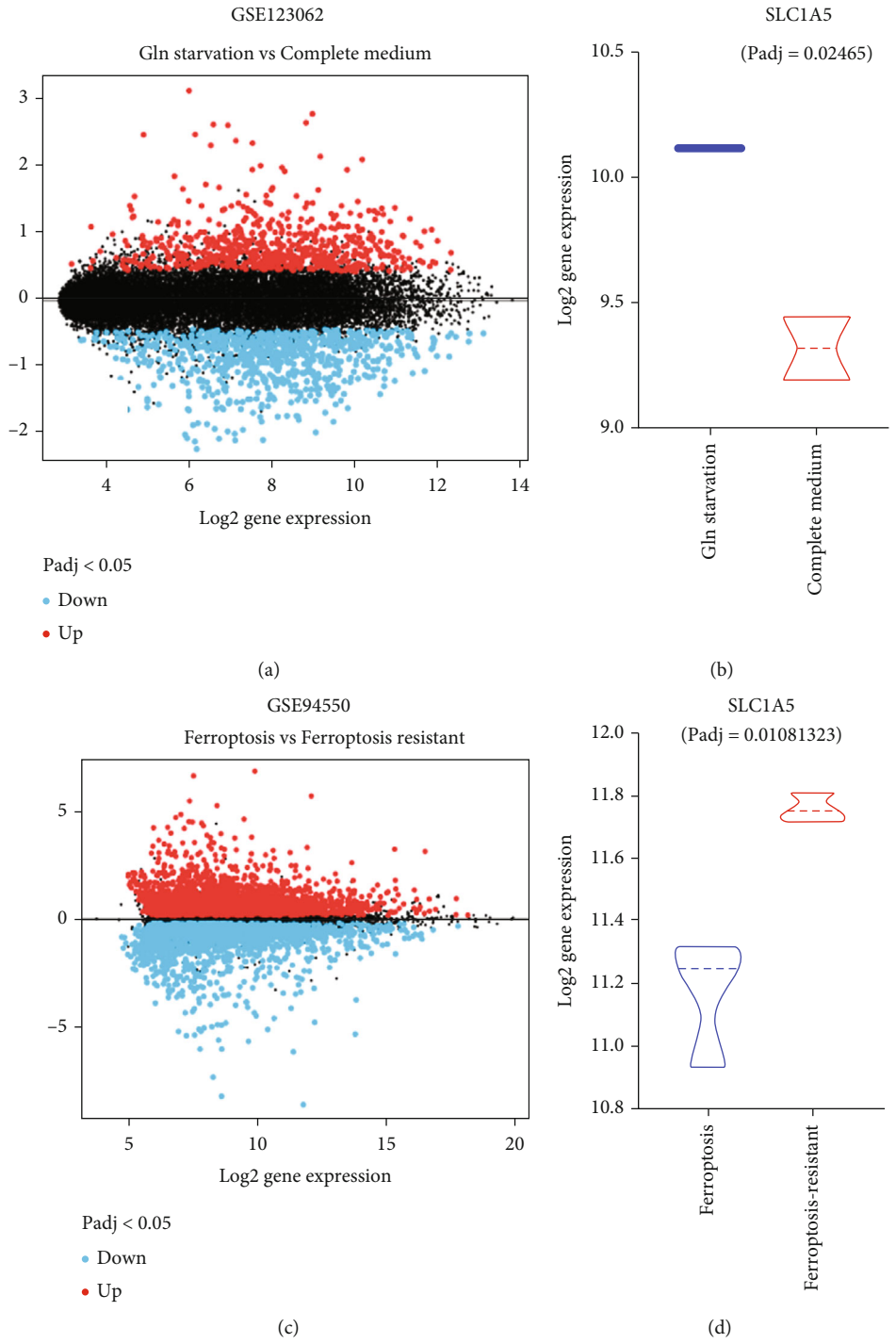

Figure 4: SLC1A5 is associated with glutamine starvation and ferroptosis response in the liver tumor. (a, b) SLC1A5 reactively increases when liver tumor cells suffer glutamine starvation (GSE123062). The volcano map displays the differently expressed genes between liver tumor cells treated with glutamine and those treated without glutamine (a). SLC1A5 is upregulated during glutamine starvation (b). (c, d) Huh7 cells with response to ferroptosis inducer sorafenib have lower expression level of SLC1A5, compared to those without response to ferroptosis.

Next, we evaluated the correlation between AFGs and overall survival (OS) data from TCGA dataset. COX regression analysis showed 9 AFGs with $p < 0.05$ (Figure 2(e)) as the potential prognostic AFGs. Moreover, multivariate Cox regression analysis was performed to explore the independent prognostic genes (Figure 2(f), TXNRD1, ASNS, SLC7A11, and SLC1A5) and construct a four-gene risk signature model (Figures 3(a)–3(j), and Supplementary file 5).

Among the four independent prognostic genes, SLC1A5 is the critical transporter for glutamine uptake and a

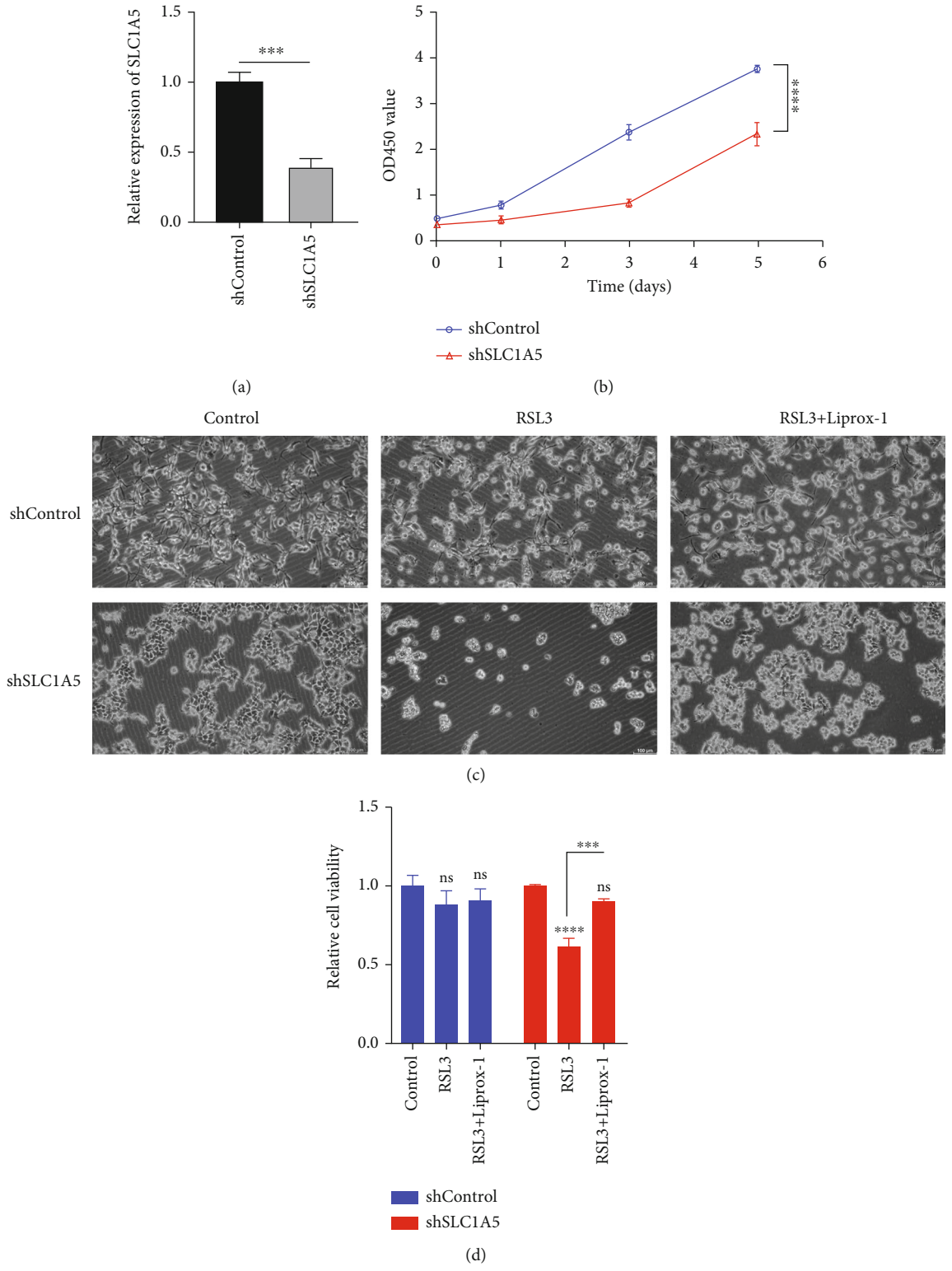

Figure 5: Continued.

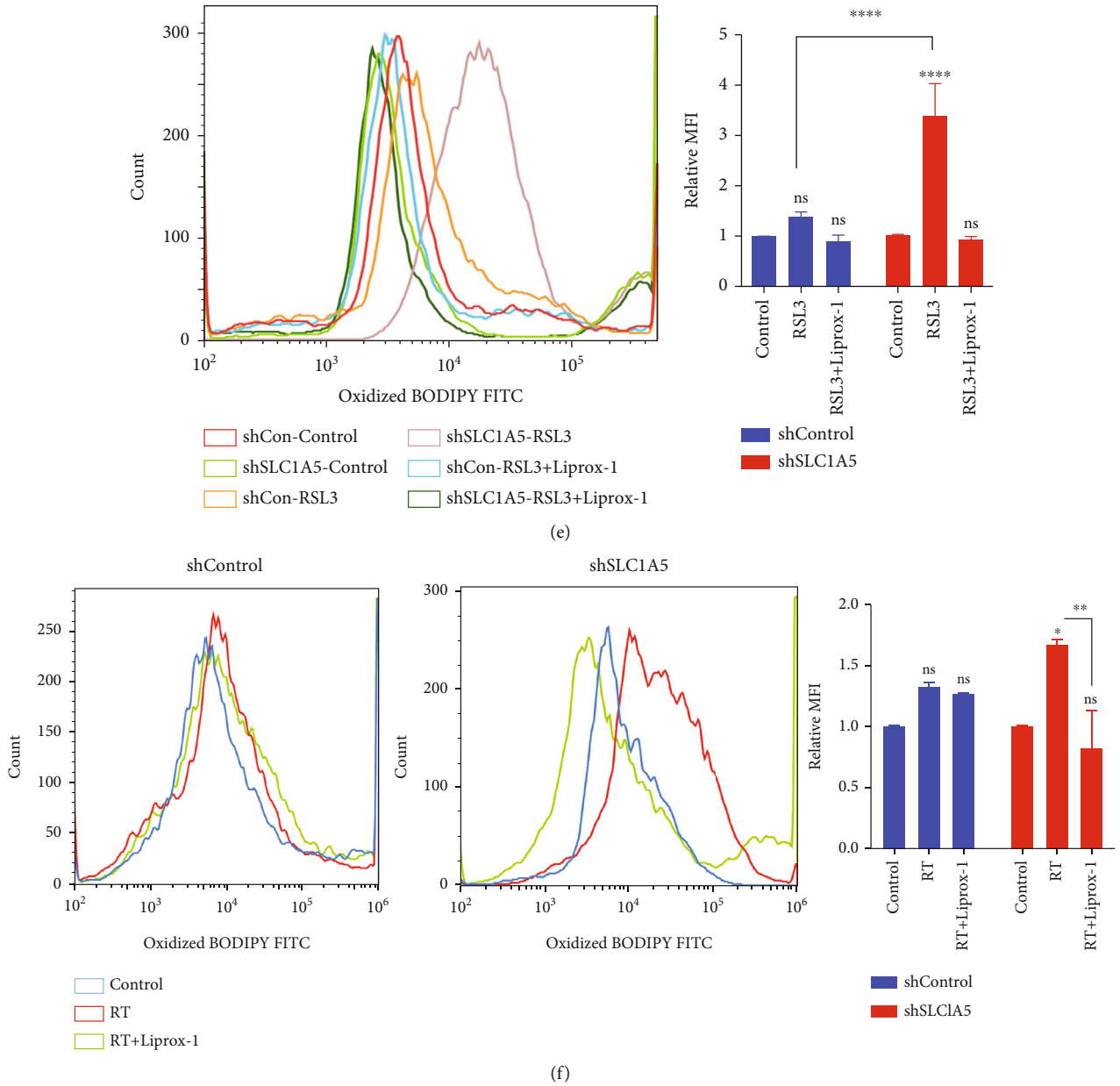

Figure 5: Glutamine transporter SLC1A5 affected ferroptosis response in liver tumor cell lines. (a) The knockdown efficiency of SLC1A5 in Huh7 cells was determined by qPCR. (b) In shSLC1A5 cells, the results of CCK8 demonstrated a significant reduction in tumor cell proliferation. (c) After RSL3 stimulation (2.5 μM for 6 hours), the level of cell viability in shSLC1A5 Huh7 cells was much lower than it was in shControl cells. (d) In shSLC1A5 cells, the MFI of LPO increased substantially, and the elevated MFI of LPO was reversed by a ferroptosis inhibitor. (e) After Erastin stimulation (25 μM for 24 hours), the level of cell viability in shSLC1A5 Huh7 cells was much lower than it was in shControl cells. Lirpoxstatin-1 could reverse the enhanced ferroptosis effect induced by knock-down of SLC1A5. (f) shSLC1A5 dramatically improved the liver tumor cells' sensitivity to irradiation-induced LPO accumulation. RT: 8 Gy. AFGs: amino acid-ferroptosis genes; ferr-1: ferrostatin-1. $^{*}p < 0.05$; $^{**}p < 0.01$; $^{***}p < 0.001$; $^{****}p < 0.0001$.

suppressor gene in ferroptosis. In liver tumor tissue, the expression of SLC1A5 was significantly higher than in normal liver tissues (Figures 2(b) and 2(c)). As shown in Figures 4(a) and 4(b), SLC1A5 reactively increased when liver tumor cells suffered glutamine starvation. Moreover, Huh7 cells with response to ferroptosis inducer sorafenib had lower expression level of SLC1A5, compared to those without response to ferroptosis ($p = 0.01081323$, Figures 4(c) and 4(d)). Collectively, these findings suggested that SLC1A5 is upregulated in liver tumors, and the expression level of SLC1A5 is correlated with liver tumor patients' prognosis.

Gene risk signature reveals that high expression of SLC1A5 is tightly related to a high risk of death.

To further evaluate the predictive power of SLC1A5 in prognostics of liver tumor patients, all TCGA liver tumor patients were randomly divided into training cohort ($n = 168$) and validation cohort ($n = 166$). The patients in the training and validation cohort were further divided into

the high- and low-risk groups based on the median value of the risk score. In the training cohort, there were 84 patients in each of the high- and low-risk groups. In the validation cohort, 73 patients were in the high-risk group and 93 patients were in the low-risk group. The risk scores of all liver tumor patients were calculated as follows: TXNRD1 ∗ 0.011594283 + ASNS ∗ 0.11892719 + SLC1A5 ∗ 0.014906744 + SLC7A11 ∗ 0.122043117. The expression of the four AFGs in training and validation cohorts is shown in Figures 3(a) and 3(b). The Kaplan-Meier (KM) survival curves demonstrated that the prognosis of liver tumor patients in the low-risk group was significantly higher than that in the high-risk group in both the train and validation cohorts (Figures 3(c) and 3(d)). In the training and validation cohorts, the areas under the curves (AUCs) of the time-dependent receiver operating characteristic (ROC) curves of the predicted 1-year risk OS were 0.797 and 0.684, respectively (Figures 3(e) and 3(f)). Between the two groups, there were significant differences in the survival curve and status (Figures 3(g) and 3(h)). The death cases in the high-risk group are significantly higher than those in the low-risk group.

3.3. Loss of SLC1A5 Is Involved in Radiosensitization. To further confirm the function of SLC1A5 at a cellular level, we utilized lentivirus transduction to knock down SLC1A5 using an shRNA vector that specifically targets SLC1A5 (shSLC1A5) in Huh7 cells. As shown in Figure 5(a), shSLC1A5 resulted in a 70% reduction of SLC1A5 mRNA when compared to a control shRNA vector in Huh7 cells. In shSLC1A5 cells, the results of CCK8 demonstrated a significant reduction in tumor cell proliferation (Figure 5(b)). The results showed that SLC1A5 deletion abolished Huh7 cell growth *in vitro*.

Next, we explored the effect of SLC1A5 on ferroptosis and radiosensitivity. After ferroptosis stimulation, the level of cell viability in SLC1A5 null Huh7 cells was much lower than it was in shRNA control cells (Figures 5(c) and 5(e)). In SLC1A5 null cells, the MFI of LPO increased substantially, and the elevated MFI of LPO was reversed by a ferroptosis inhibitor (Figure 5(d)). Moreover, the absence of SLC1A5 dramatically improved the liver tumor cells' sensitivity to irradiation-induced LPO accumulation (Figure 5(f)). Collectively, these results indicated that SLC1A5 was a ferroptosis suppressor gene in liver tumor cells, and deletion of SLC1A5 may boost RT response by enhancing the ferroptosis effect.

4. Discussion

Recently, the effects of ferroptosis in radiotherapy have attracted much interest. Previous investigations highlighted the fatal consequences of lipid peroxides introduced by ferroptosis and irradiation, as well as the synergistic effect of ferroptosis on radiotherapy [4, 6, 25]. According to some research, amino acids may influence tumor response to irradiation via modulating ferroptosis signals [6, 26, 27]. However, ferroptosis-dependent radiosensitivity is a complicated issue, and the mechanism governing amino acid metabolism in ferroptosis remains obscure. We verified that amino acids played a significant role in ferroptosis-regulated radiosensitivity and identified 4 independently prognostic AFGs (SLC1A5, SLC7A11, ASNS, and TXNRD1) as prospective candidates for predicting ferroptosis and irradiation response. Amino acid transportation and metabolism regulate ferroptosis and provide new opportunities for developing radiation-resistant targeted therapies for liver tumor.

In the current study, we discovered that liver tumor cells resisted irradiation by increasing their amino acid content to defend against ferroptosis. These findings were consistent with previous investigations. Patients with nonalcoholic steatohepatitis (NASH), one of the precancerous diseases of liver tumor, showed a high concentration of glutamate in circulation [28]. Increased glutamine was primarily used to generate GSH to overcome oxidative stress, particularly in liver tumor patients with a history of NASH. Since both RT and ferroptosis have a fatal effect on tumor cells by increasing oxidative stress, a high number of intracellular antioxidants can prevent ferroptotic cell death and promote liver tumor progression. Our findings not only investigated the metabolic characteristics of radioresistance liver tumor cells upon ferroptosis stress but also demonstrated that glutamine was required for liver tumor cells' survival. Glutamine deprivation induced ferroptosis in liver tumor cells, which would be reversed by ferroptosis inhibitors, indicating that targeting glutamine uptake could be a therapeutic strategy for liver tumor treatment. These findings could pave the way for a new approach to adjuvant therapy that targets or alters amino acid metabolism to improve radiation response in liver tumor. Focusing on the impact of glutamine starvation on ferroptosis, however, should take into account the number and kind of deficient amino acids, time window, and heterogeneity of tumors or tumor cell lines. Based on the presence of transferrin and the stress of multiple amino acid deprivation, Gao et al.'s work showed that glutamine was required for inducing ferroptosis in MEF cells [29]. It should be noted that Gao et al.'s study uses a design of multiple amino acid deprivation rather than a single amino acid deprivation and that the time window is 12 hours, indicating an early response to nutrient stress. In contrast, we just deplete glutamine and assess the tumor cells' response 24 hours later, which may reflect an intermediate or advanced response to nutrient stress. Therefore, distinct phenotypes in tumor cells may be induced depending on the type of deficient amino acids and the time window. Additionally, the heterogeneity of various tumors or diverse tumor cell lines may also play a significant role in how cancers respond to amino acid deprivation. For example, the sensitivity of a panel of lung cancer cell lines to glutamine deprivation varied significantly, with some cells exhibiting almost total independence [30]. Additionally, basal-type cells tend to be glutamine-dependent, whereas luminal-type cells tend to be glutamine-independent in breast cancer cells, demonstrating systematic distinctions in glutamine dependence [31]. However, in the current study, the HT1080 cell line and diverse liver tumor cell lines (HepG2, Huh7, and SMMC-7721) show vulnerability to ferroptosis caused by glutamine starvation. Similar results were also reported in Wappler et al.'s [32] investigation: chemoresistance was

entirely reversed in glutamine-depleted cholangiocarcinoma. Qing et al. [33] also demonstrated that glutamine deprivation induces cell death in neuroblastoma. Therefore, more research is needed to better determine how glutamine deprivation affects ferroptosis in various tumor types. SLC1A5 is a critical glutamine transporter involved in ferroptosis. In the current study, we found that knockdown of SLC1A5 increased liver tumor cells' response to irradiation-induced oxidative damage at a dose of 10 Gy. SLC1A5 has been regarded as an oncogene by the mTORC1 signaling pathways or KRAS mutation in certain tumors [34, 35], and loss of SLC1A5 may inhibit tumor growth. Furthermore, targeting SLC1A5 has been shown to sensitize ferroptosis in melanoma [18]. In liver tumor, some studies demonstrated the role of SLC1A5 as a risk factor [36–38], which were consistent with our findings. These findings indicate that targeting SLC1A5 tends to be an effective approach to improve liver tumor patients' prognosis. However, it is worth noting that SLC1A5 is not the only glutamine transporter. Indeed, SLC38A1 has been identified as a rescue transporter for compensating glutamine uptake [39, 40]. SLC1A5 and SLC38A1 cotransport polarized Na^+ and glutamine, and SLC1A5 has been identified as amino acid harmonizer, whereas SLC38A1 has been recognized as an amino acid loader in cancer cells [40]. However, the roles of SLC1A5 and SLC38A1 in different tumor types are still under debate. However, in some tumor cell lines, such as 143B osteosarcoma cells, loss of SLC1A5 did not suppress tumor growth, but instead elicit an amino acid starvation response and up-regulation of SLC38A1, indicating that SLC38A1 may act as a rescue transporter when SLC1A5 is blocked [40]. Therefore, the functional complementarity between SLC1A5 and SLC38A1 is intertwined, and targeting both SLC1A5 and SLC38A1 could be further evaluated for their tumor suppression capability. Besides, when evaluating the impact of SLC1A5 and SLC38A1 on ferroptosis, different tumor types and heterogeneity should also be carefully considered.

We also found a SLC1A5-based risk signature for predicting prognosis. In ferroptosis, SLC7A11 is one of the most important suppressor genes [6, 41, 42]. SLC7A11 and SLC3A2 compose the cystine antiporter system Xc-. Cystine is utilized for GSH synthesis [43]. Irradiation has been shown to suppress SLC7A11 protein expression by activating TP53 and inducing ferroptosis cell death [26]. Moreover, ferroptosis inducers inhibited SLC7A11 in a synergistic effect with RT [6]. In addition, tumors with a high level of SLC7A11 showed endogenous resistance to ferroptosis and RT. Within our four-factor risk-predicting model, TXNRD1 is a selenocysteine-containing flavoenzyme, and the enzyme activity is mainly affected by intracellular ROS [44]. Though TXNRD1 was increased in response to cysteine starvation [45], whether TXNRD1 would affect amino acid transportation or synthesis remains unclear. The research about the role of TXNRD1 in amino acid transportation or synthesis is worthy of further studies.

There are some limitations to this study. First, prospective studies should be conducted to confirm these findings, especially the predictive capability of the proposed model. Secondly, the suppressive effect of SLC1A5 on ferroptosis should be explored in further studies, particularly considering the interaction of SLC1A5 and SLC38A1. Besides that, whether the tumor microenvironment responded similarly or differently to SLC1A5 inhibition should be validated *in vivo* and *in vitro*. Next, the role of SLC1A5 on the biological effect of high-dose and low-dose irradiation should be elucidated in further studies.

5. Conclusion

Taken together, changes in amino acid metabolism hints that amino acid transportation may be crucial indicators. Given the importance of glutamine for liver tumor cells, efforts toward the qualification of biomarkers for liver tumor in clinical practice are urgent. Moreover, pharmaceutical techniques to induce ferroptosis and boost radiation response could be developed by targeting amino acid metabolism, such as transportation mediated by SLC1A5.

Data Availability

The datasets analyzed during the current study are available from the corresponding author on reasonable request.

Ethical Approval

The study is based on an analysis of available TCGA data that does not need any ethics committee's agreement and does not violate the rights of other persons or institutions.

Conflicts of Interest

The authors declare that they have no competing interests.

Authors' Contributions

Zhuhui Yuan and Tong Liu contributed equally to this work.

Acknowledgments

This work was supported by the National Natural Science Foundation of China (Nos. 82272745, 82073057, 81972966, and 82073335), the Beijing Natural Science Foundation (No. 7202228), and the Clinical Medicine plus X Project of Peking University (No. PKU2020LCXQ024).

Supplementary Materials

Figure S1: the pie graph of targeted metabolomics. HepG2 cell line and HepG2-IRR cells were treated with Erastin (50 μM) for 6 hours, and cells were collected for targeted metabolomics. The content of amino acids (AA) accounting for 25% was the most abundant metabolites in HepG2-IRR cells (FDR-corrected $p < 0.05$; FC > 1.5), compared to wild-type HepG2 cells. Fatty acids account for 21% in HepG2-IRR cells after Erastin stimulation. Supplementary 1. The materials and protocol of targeted metabolomics. In brief, HepG2 cell line and HepG2-IRR cells were treated with Erastin (50 μM) for 6 hours, and cells were collected for targeted metabolomics. An ultraperformance liquid chromatography coupled to tandem mass spectrometry (UPLC-MS/MS)

system was used to quantitate metabolites. Supplementary 2. The list of amino acid metabolism genes. Supplementary 3. The list of ferroptosis-related genes. Supplementary 4. Twenty amino acid-ferroptosis genes were identified as prognostic factors for predicting the prognosis of liver tumor patients. Supplementary 5. SLC1A5, SLC7A11, TXNRD1, and ASNS are the independent prognostic factors for liver tumor patients. *(Supplementary Materials)*

References

[1] P. Koppula, G. Lei, Y. Zhang et al., "A targetable CoQ-FSP1 axis drives ferroptosis- and radiation-resistance in KEAP1 inactive lung cancers," *Nature Communications*, vol. 13, no. 1, p. 2206, 2022.

[2] F. Wu, Y. Du, J. Yang et al., "Peroxidase-like active nanomedicine with dual glutathione depletion property to restore oxaliplatin chemosensitivity and promote programmed cell death," *ACS Nano*, vol. 16, no. 3, pp. 3647–3663, 2022.

[3] C. Zhang, X. Liu, S. Jin, Y. Chen, and R. Guo, "Ferroptosis in cancer therapy: a novel approach to reversing drug resistance," *Molecular Cancer*, vol. 21, no. 1, p. 47, 2022.

[4] G. Lei, Y. Zhang, P. Koppula et al., "The role of ferroptosis in ionizing radiation-induced cell death and tumor suppression," *Cell Research*, vol. 30, no. 2, pp. 146–162, 2020.

[5] M. Yang, X. Wu, J. Hu et al., "COMMD10 inhibits HIF1α/CP loop to enhance ferroptosis and radiosensitivity by disrupting Cu-Fe balance in hepatocellular carcinoma," *Journal of Hepatology*, vol. 76, no. 5, pp. 1138–1150, 2022.

[6] X. Lang, M. D. Green, W. Wang et al., "Radiotherapy and immunotherapy promote tumoral lipid oxidation and ferroptosis via synergistic repression of SLC7A11," *Cancer Discovery*, vol. 9, no. 12, pp. 1673–1685, 2019.

[7] L. F. Ye, K. R. Chaudhary, F. Zandkarimi et al., "Radiation-Induced Lipid Peroxidation Triggers Ferroptosis and Synergizes with Ferroptosis Inducers," *ACS chemical biology*, vol. 15, no. 2, pp. 469–484, 2020.

[8] G. Lei, Y. Zhang, T. Hong et al., "Ferroptosis as a mechanism to mediate p53 function in tumor radiosensitivity," *Oncogene*, vol. 40, no. 20, pp. 3533–3547, 2021.

[9] Z. Zhang, M. Lu, C. Chen et al., "Holo-lactoferrin: the link between ferroptosis and radiotherapy in triple-negative breast cancer," *Theranostics*, vol. 11, no. 7, pp. 3167–3182, 2021.

[10] Y. Shibata, H. Yasui, K. Higashikawa, N. Miyamoto, and Y. Kuge, "Erastin, a ferroptosis-inducing agent, sensitized cancer cells to X-ray irradiation via glutathione starvation *in vitro* and *in vivo*," *PloS one*, vol. 14, no. 12, article e0225931, 2019.

[11] L. Zhang, C. S. Hobeika, D. Khabibullin et al., "Hypersensitivity to ferroptosis in chromophobe RCC is mediated by a glutathione metabolic dependency and cystine import via solute carrier family 7 member 11," *Proceedings of the National Academy of Sciences of the United States of America*, vol. 119, no. 28, article e2122840119, 2022.

[12] S. Suzuki, D. Venkatesh, H. Kanda et al., "GLS2 Is a Tumor Suppressor and a Regulator of Ferroptosis in Hepatocellular Carcinoma," *Cancer Research*, vol. 82, no. 18, pp. 3209–3222, 2022.

[13] X. Fu, K. Li, Y. Niu et al., "The mTOR/PGC-1α/SIRT3 pathway drives reductive glutamine metabolism to reduce oxidative stress caused by ISKNV in CPB cells," *Microbiology Spectrum*, vol. 10, no. 1, article e0231021, 2022.

[14] A. Mukha, U. Kahya, A. Linge et al., "GLS-driven glutamine catabolism contributes to prostate cancer radiosensitivity by regulating the redox state, stemness and ATG5-mediated autophagy," *Theranostics*, vol. 11, no. 16, pp. 7844–7868, 2021.

[15] V. Trézéguet, H. Fatrouni, and A. J. Merched, "Immuno-metabolic modulation of liver oncogenesis by the tryptophan metabolism," *Cell*, vol. 10, no. 12, p. 3469, 2021.

[16] F. Huang, R. Yang, Z. Xiao et al., "Targeting ferroptosis to treat cardiovascular diseases: a new continent to be explored," *Frontiers in Cell and Development Biology*, vol. 9, article 737971, 2021.

[17] S. Delgir, M. Bastami, K. Ilkhani, A. Safi, F. Seif, and M. R. Alivand, "The pathways related to glutamine metabolism, glutamine inhibitors and their implication for improving the efficiency of chemotherapy in triple-negative breast cancer," *Mutation Research, Reviews in Mutation Research*, vol. 787, article 108366, 2021.

[18] M. Luo, L. Wu, K. Zhang et al., "miR-137 regulates ferroptosis by targeting glutamine transporter SLC1A5 in melanoma," *Cell Death and Differentiation*, vol. 25, no. 8, pp. 1457–1472, 2018.

[19] G. Xie, L. Wang, T. Chen et al., "A metabolite array technology for precision medicine," *Analytical Chemistry*, vol. 93, no. 14, pp. 5709–5717, 2021.

[20] K. Li, K. Xu, Y. He et al., "Functionalized tumor-targeting nanosheets exhibiting Fe(II) overloading and GSH consumption for ferroptosis activation in liver tumor," *Small*, vol. 17, no. 40, article e2102046, 2021.

[21] X. Ren, Y. Li, Y. Zhou et al., "Overcoming the compensatory elevation of NRF2 renders hepatocellular carcinoma cells more vulnerable to disulfiram/copper-induced ferroptosis," *Redox Biology*, vol. 46, article 102122, 2021.

[22] X. Chen, R. Kang, G. Kroemer, and D. Tang, "Broadening horizons: the role of ferroptosis in cancer," *Nature Reviews Clinical Oncology*, vol. 18, no. 5, pp. 280–296, 2021.

[23] J. Wen, K. Xiong, A. Aili et al., "PEX5, a novel target of microRNA-31-5p, increases radioresistance in hepatocellular carcinoma by activating Wnt/β-catenin signaling and homologous recombination," *Theranostics*, vol. 10, no. 12, pp. 5322–5340, 2020.

[24] Y. P. Kang, A. Mockabee-Macias, C. Jiang et al., "Non-canonical glutamate-cysteine ligase activity protects against ferroptosis," *Cell Metabolism*, vol. 33, no. 1, pp. 174–189.e7, 2021.

[25] D. Shen, J. Luo, L. Chen et al., "PARPi treatment enhances radiotherapy-induced ferroptosis and antitumor immune responses via the cGAS signaling pathway in colorectal cancer," *Cancer Letters*, vol. 550, p. 215919, 2022.

[26] L. Jiang, N. Kon, T. Li et al., "Ferroptosis as a p53-mediated activity during tumour suppression," *Nature*, vol. 520, no. 7545, pp. 57–62, 2015.

[27] H. Ogiwara, K. Takahashi, M. Sasaki et al., "Targeting the vulnerability of glutathione metabolism in ARID1A-deficient cancers," *Cancer Cell*, vol. 35, no. 2, pp. 177–190.e8, 2019.

[28] Y. Zhou, M. Orešič, M. Leivonen et al., "Noninvasive detection of nonalcoholic steatohepatitis using clinical markers and circulating levels of lipids and metabolites," *Clinical Gastroenterology and Hepatology*, vol. 14, no. 10, pp. 1463–1472.e6, 2016.

[29] M. Gao, P. Monian, N. Quadri, R. Ramasamy, and X. Jiang, "Glutaminolysis and transferrin regulate ferroptosis," *Molecular Cell*, vol. 59, no. 2, pp. 298–308, 2015.

[30] A. P. van den Heuvel, J. Jing, R. F. Wooster, and K. E. Bachman, "Analysis of glutamine dependency in non-small cell

lung cancer: GLS1 splice variant GAC is essential for cancer cell growth," *Cancer Biology & Therapy*, vol. 13, no. 12, pp. 1185–1194, 2012.

[31] H. N. Kung, J. R. Marks, and J. T. Chi, "Glutamine synthetase is a genetic determinant of cell type-specific glutamine independence in breast epithelia," *PLoS Genetics*, vol. 7, no. 8, article e1002229, 2011.

[32] J. Wappler, M. Arts, A. Röth et al., "Glutamine deprivation counteracts hypoxia-induced chemoresistance," *Neoplasia*, vol. 22, no. 1, pp. 22–32, 2020.

[33] G. Qing, B. Li, A. Vu et al., "ATF4 regulates *MYC*-mediated neuroblastoma cell death upon glutamine deprivation," *Cancer Cell*, vol. 22, no. 5, pp. 631–644, 2012.

[34] A. K. Najumudeen, F. Ceteci, S. K. Fey et al., "The amino acid transporter SLC7A5 is required for efficient growth of KRAS-mutant colorectal cancer," *Nature Genetics*, vol. 53, no. 1, pp. 16–26, 2021.

[35] Y. Pan, M. Han, X. Zhang et al., "Discoidin domain receptor 1 promotes hepatocellular carcinoma progression through modulation of SLC1A5 and the mTORC1 signaling pathway," *Cellular Oncology (Dordrecht)*, vol. 45, no. 1, pp. 163–178, 2022.

[36] H. Zhang, R. Liu, L. Sun, W. Guo, and X. Hu, "The effect of ferroptosis-related genes on prognosis and tumor mutational burden in hepatocellular carcinoma," *Journal of Oncology*, vol. 2021, Article ID 7391560, 12 pages, 2021.

[37] G. Hu, X. Huang, B. Zhang, P. Gao, W. Wu, and J. Wang, "Identify an innovative ferroptosis-related gene in hepatocellular carcinoma," *Journal of Clinical Laboratory Analysis*, vol. 36, no. 9, article e24632, 2022.

[38] Z. A. Chen, H. Tian, D. M. Yao, Y. Zhang, Z. J. Feng, and C. J. Yang, "Identification of a ferroptosis-related signature model including mRNAs and lncRNAs for predicting prognosis and immune activity in hepatocellular carcinoma," *Frontiers in Oncology*, vol. 11, article 738477, 2021.

[39] J. Zhang, N. N. Pavlova, and C. B. Thompson, "Cancer cell metabolism: the essential role of the nonessential amino acid, glutamine," *The EMBO Journal*, vol. 36, no. 10, pp. 1302–1315, 2017.

[40] A. Broer, F. Rahimi, and S. Broer, "Deletion of amino acid transporter ASCT2 (SLC1A5) reveals an essential role for transporters SNAT1 (SLC38A1) and SNAT2 (SLC38A2) to sustain glutaminolysis in cancer cells," *The Journal of Biological Chemistry*, vol. 291, no. 25, pp. 13194–13205, 2016.

[41] L. A. Timmerman, T. Holton, M. Yuneva et al., "Glutamine sensitivity analysis identifies the xCT antiporter as a common triple-negative breast tumor therapeutic target," *Cancer Cell*, vol. 24, no. 4, pp. 450–465, 2013.

[42] X. Liu, K. Olszewski, Y. Zhang et al., "Cystine transporter regulation of pentose phosphate pathway dependency and disulfide stress exposes a targetable metabolic vulnerability in cancer," *Nature Cell Biology*, vol. 22, no. 4, pp. 476–486, 2020.

[43] J. L. Parker, J. C. Deme, D. Kolokouris et al., "Molecular basis for redox control by the human cystine/glutamate antiporter system xc^-," *Nature Communications*, vol. 12, no. 1, p. 7147, 2021.

[44] R. Gencheva and E. S. J. Arner, "Thioredoxin reductase inhibition for cancer therapy," *Annual Review of Pharmacology and Toxicology*, vol. 62, no. 1, pp. 177–196, 2022.

[45] S. Liu, W. Wu, Q. Chen et al., "TXNRD1: a key regulator involved in the ferroptosis of CML cells induced by cysteine depletion in vitro," *Oxidative Medicine and Cellular Longevity*, vol. 2021, Article ID 7674565, 12 pages, 2021.

Hindawi
Oxidative Medicine and Cellular Longevity
Volume 2022, Article ID 5424411, 17 pages
https://doi.org/10.1155/2022/5424411

Research Article

Curcumin Enhanced Ionizing Radiation-Induced Immunogenic Cell Death in Glioma Cells through Endoplasmic Reticulum Stress Signaling Pathways

Zenghe Xiu,[1] Ting Sun,[2] Ying Yang,[1] Yuping He,[1] Shuangyu Yang,[1] Xuefei Xue,[1] and Wei Yang[1]

[1]*State Key Laboratory of Radiation Medicine and Protection, School of Radiation Medicine and Protection, Collaborative Innovation Center of Radiation Medicine of Jiangsu Higher Education Institutions, Soochow University, Suzhou, Jiangsu, China*
[2]*Neurosurgery and Brain and Nerve Research Laboratory, The First Affiliated Hospital of Soochow University, Suzhou, Jiangsu, China*

Correspondence should be addressed to Ting Sun; sunting1979st@aliyun.com and Wei Yang; detachedy@aliyun.com

Received 29 June 2022; Revised 8 September 2022; Accepted 13 September 2022; Published 4 October 2022

Academic Editor: Bing Wang

Objective. Local radiotherapy may cause distant tumor regression via inducing immunogenic cell death (ICD). Here, we investigated the effect of curcumin on ionizing radiation-induced immunogenic cell death in normoxic or hypoxic glioma cells and its mechanism in vitro and vivo. *Methods*. Hypoxic or normoxic glioma cell apoptosis and the cell surface exposure of calreticulin (CRT) were detected by flow cytometry. Extracellular ATP and HSP70 were measured by chemiluminescence assay and ELISA, respectively. Endoplasmic reticulum (ER) stress protein levels were detected by western blot. Moreover, the induction of bona fide ICD was detected by vaccination assays in mice bearing glioma model. Spleen lymphocytes and tumor-infiltrating lymphocyte subsets were analyzed by flow cytometry and immunohistochemistry. *Results*. Curcumin incubation before X-ray irradiation significantly increased radiation-induced apoptosis rate in normoxic or hypoxic glioma cells. Curcumin enhanced radiation-induced CRT exposure, release of HSP70 and ATP, and ER stress signaling activity. After treatment with ER stress pathway inhibitors, cell apoptosis and CRT exposure induced by the combination treatment of curcumin and X-ray were reduced. In vaccination experiments, glioma cells irradiated by X-ray produced a strong immunogenic response rejecting tumor formation in 70% mice. In comparison, cells treated by curcumin and X-ray produced a stronger immune response rejecting tumor formation in 90% mice. The combination treatment increased the percentage of tumor-infiltrating CD4+, CD8+ T lymphocytes, and CD11c+ dendritic cells compared to X-ray irradiation alone. *Conclusion*. Ionizing radiation-induced normoxic or hypoxic glioma immunogenic cell death could be further enhanced by curcumin through activating the ER stress PERK-eIF2α and IRE1α-XBP1 signaling pathways.

1. Introduction

Glioma is the deadliest subtype of primary brain tumor, whose overall survival is about 15 months [1, 2]. Even though glioma is treated with the combination of conventional therapies, the efficacy is still limited. Hypoxia exists in almost all solid tumors, including glioma. DNA damage resistance and oxidative stress resistance caused by hypoxia can significantly reduce cancer cell death induced by radiotherapy [3, 4].

Immunogenic cell death (ICD) is different from general apoptosis. Some physical factors, including ionizing radiation (IR), and chemical factors induce endoplasmic reticulum (ER) stress via reactive oxygen species (ROS), leading to the cell surface exposure or release of damage-associated molecular patterns (DAMPs) and triggering antitumor

immune response [5, 6]. DAMPs are endogenous molecules; however, when they are exposed to the surface of dying cells or released, they can perform immunoregulatory functions. There are some DAMPs closely related to ICD. ER chaperone calreticulin (CRT) exposed on cell surface, an "eat me" signal, can be recognized by phagocytic cell surface CD91 receptor, thereby promoting the phagocytosis of dying cells [7]. Other cytoplasmic or ER chaperone molecules, such as heat shock protein (HSP) 70/90, can also act as an "eat me" signal through cell membrane exposure [8]. ATP acts as a strong "find-me" signal via binding to P2Y2 purine receptor to attract monocytes or acts as a proinflammatory molecule to bind to P2X7 receptor on innate immune cells [9]. On the contrary, CD47, a "don't eat me" signal, is a transmembrane protein that can bind to a variety of ligands and regulate tumor development [10].

Curcumin, an active phenolic substance, is a multifunctional molecule with antioxidant, antibacterial, anti-inflammatory, and immunomodulatory effects. Curcumin can regulate cell apoptosis via various pathways and affect the metastasis and proliferation of tumors [11]. Curcumin can suppress HIF-1 activity in a variety of tumor cells and improve tumor hypoxia [12, 13].

In this study, to investigate the effect of curcumin on the IR-induced immunogenic cell death in glioma cells and its mechanism, we detected the apoptosis of human glioma U251 cells and mouse glioma GL261 cells, the release of ICD-related DAMPs, and the activation of ER stress pathways after the combination treatment of curcumin and X-ray irradiation under normoxic and hypoxic condition. Furthermore, animal models using C57BL/6J mice implanted with GL261 cells were conducted to verify whether curcumin could enhance IR-induced ICD in vivo through ER stress pathways.

2. Materials and Methods

2.1. Cell Culture. Mouse glioma GL261 and human glioma U251 cell lines were purchased from the Shanghai Institutes for Biological Sciences, Chinese Academy of Sciences, and were cultured in DMEM with 10% FBS. Hypoxia cells were treated with 1% O_2, 5% CO_2, and 94% N_2 in a hypoxia workstation (Invivo2 1000, Ruskinn).

2.2. X-Ray Irradiation. Cells were exposed to 10 Gy (normoxia)/25 Gy (hypoxia) X-ray (160 kV, 1.16 Gy/min) by a linear accelerator (RadSource, RS2000) at room temperature.

2.3. Flow Cytometry. Cells were digested and collected after curcumin and IR treatment. The spleen and tumor were cut into tissue pieces, and cell suspension was made with trypsin. Cells were stained using PE-Annexin V/7-AAD apoptotic Kit (BioLegend) according to the manufacturer's instructions. Cells were incubated with antibodies for 30 min at room temperature. The primary antibodies include PE-conjugated anti-CRT rabbit antibody (1 : 50, Cell Signaling), anti-CD47 antibody (1 : 100, Biorbyt), FITC-conjugated anti-CD45 mouse antibody (1 : 100, eBioscience), APC-conjugated anti-CD3 mouse antibody (1 : 100, eBioscience), and V450-conjugated anti-CD8 mouse antibody (1 : 100, eBioscience). Labeled cells were analyzed by a flow cytometric Becton Dickinson FACScan (BD Biosciences).

2.4. Calreticulin Exposure. Cells were stained with Calreticulin-PhycoErythrin antibody (1 : 50, Cell Signaling) and then washed and resuspended in FACS buffer for assessing with flow cytometry. For confocal microscopy (Olympus FV1200), 3×10^5/ml cells were seeded on sterile coverslips and incubated with CRT antibody (1 : 1000, Cell Signaling) for 12 h, then incubated with Alexa Fluor 555 secondary antibodies and Hoechst 33342 (Beyotime) for 1 h, and assessed by confocal microscopy. The wavelengths of excite light and emit light are 488 nm and 575 nm, respectively.

2.5. Western Blot. Cell lysates were prepared in RIPA lysis buffer containing phenylmethylsulfonyl fluoride (PMSF). The protein samples were separated by 10% sodium dodecyl sulfate-polyacrylamide gel (SDS-PAGE) and then were transferred onto the polyvinylidene fluoride (PVDF) membrane. The membrane was then blocked with 5% nonfat dry milk for 1 h. Primary rabbit antibodies include anti-β-actin (1 : 1000, Cell Signaling), anti-CHOP (1 : 1000, Cell Signaling), anti-PERK (1 : 1000, Cell Signaling), phospho-PERK (1 : 1000, Invitrogen), IRE1-α (1 : 1000, Cell Signaling), p-IRE1-α (1 : 1000; Invitrogen), and splicing XBP1 (1 : 1000, Cell Signaling). HRP-conjugated anti-rabbit secondary antibodies were used, and the chemiluminescent signal was detected by using electrochemiluminescence (ECL) reagents.

2.6. Enzyme-Linked Immunosorbent Assay (ELISA). After irradiation, glioma cells were cultured in normoxia or hypoxia for 24 h, and then, the cell culture supernatants were centrifuged at 500 g for 5 min at room temperature and stored at -80°C. The extracellular HSP70 protein contents were detected using a HSP70 ELISA kit (Shanghai sig Biotechnology Co., Ltd.) according to the corresponding manufacturer's instructions.

2.7. ATP Assays. Supernatants of irradiated glioma cells were used to assess extracellular ATP with a luciferase assay kit (Beyotime, Shanghai) following the manufacturer's instructions. In brief, ATP detection working solutions were prepared and seeded (100 μl/well) into 96-well plates. Then, 50 μl of standard or sample was added into each well. The plates were put into the microplate reader, and the detector is 1 mm away from the liquid level to detect the luminescence value.

2.8. DC Generation and Maturation. Peripheral blood was collected from healthy donors and PBMCs were isolated by gradient centrifugation at 400-500 g for 20-25 min at 18-20°C. PBMCs were resuspended and seeded (2×10^6 cells/ml/well) into 6-well plates. After incubation in 37°C for 2 h, nonadherent cells were removed, and complete medium (10% FBS, 800 U/ml GM-CSF, 500 U/ml IL-4 growth factor) was provided. The medium was replaced every 2-3 days. On

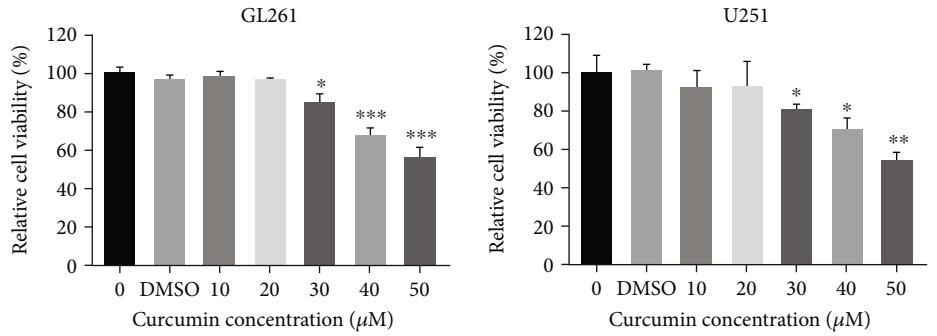

(a)

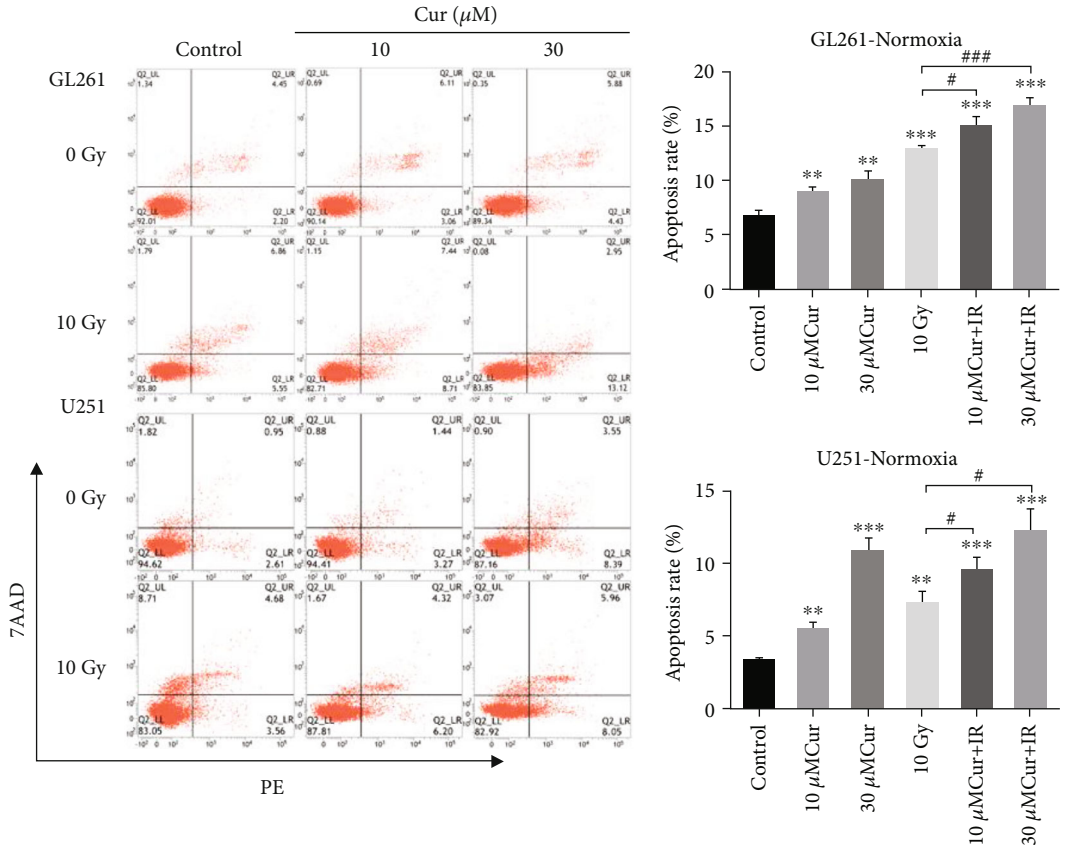

(b)

Figure 1: Continued.

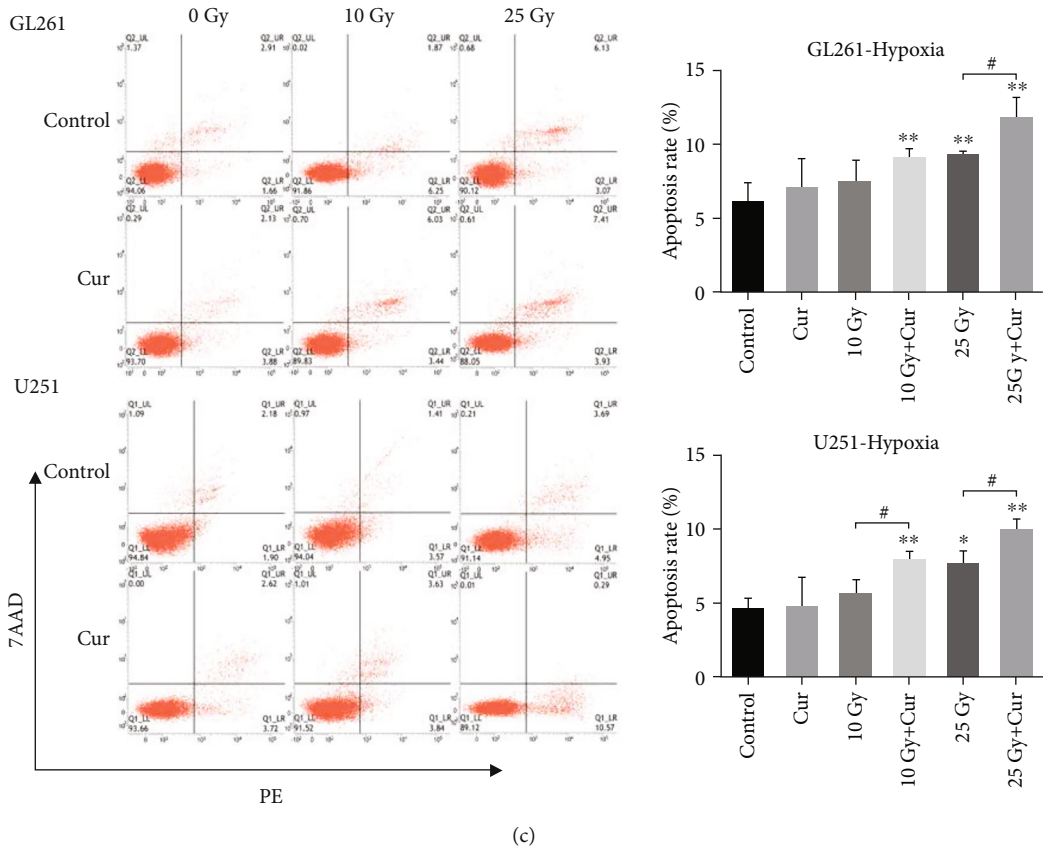

Figure 1: Curcumin enhanced apoptosis induced by IR in normoxic and hypoxic glioma cells. (a) The survival rates of GL261 and U251 cells after treatment with various concentrations of curcumin for 24 h. (b) Under normoxic conditions, GL261 and U251 cells were treated with 10 and 30 μM curcumin and incubated for 24 h after 10 Gy IR. Cell apoptosis was detected by flow cytometry after 7AAD/PE staining. (c) Under hypoxic conditions, GL261 and U251 cells were treated with/without 30 μM curcumin and incubated for 24 h after 10 Gy/25Gy IR. Cell apoptosis was assessed by flow cytometry after 7AAD/PE staining. $^{*}P < 0.05$, $^{**}P < 0.01$, and $^{***}P < 0.001$ vs. control; $^{\#}P < 0.05$ and $^{\#\#\#}P < 0.001$ vs. IR.

the 6th day, 10 ng/ml TNF-*a* was added to the medium, and then, mature DCs were harvested 2 days later.

2.9. DC Chemotaxis Assay. U251 cells were seeded (1×10^5 cells/500 μl) in the lower chamber after 10 Gy or 25 Gy X-ray irradiation. Mature DCs (3×10^5 cells/200 μl) were added into the upper chamber (8.0 μm, LABSELECT, China). After incubation for 12 h and 24 h, DCs attached to the bottom of the upper chamber were fixed with 4% paraformaldehyde and stained with 0.1% crystal violet.

2.10. DC Phagocytosis Assay. U251 cells incubated with or without 15 μM curcumin were marked red by CellTrace kit (Invitrogen) according to the instruction manual. Mature DCs were stained green using the same kit. U251 cells (2×10^4 cells/500 μl) and mature DCs (4×10^4 cells/500 μl) were mixed together and incubated in 35 mm dishes for 8 h.

2.11. Prophylactic Vaccinations. The 6-8-week-old male C57BL/6J mice with the body weight of 18-20 g (Experimental Animals Center of Shanghai Institute of Life Science) were fed and housed in SPF condition. The mice were randomly divided into control group, curcumin group, X-ray treatment group, and curcumin combined with X-ray treatment group. GL261 cells were treated with PBS, curcumin (30 μM), X-ray (10 Gy), and X-ray (10 Gy) and curcumin for 24 h, respectively. Then, 1×10^6 GL261 cells were injected into the left hind limb of the mice subcutaneously. One week later, 3×10^6 live GL261 cells were injected into the right hind limb subcutaneously. The tumor volumes at the right were measured with calipers every three days and calculated as (length^2 × width)/2, and the tumor formation rates were also calculated.

2.12. Hypoxic Transplanted Tumor Model. For in vivo implantation, GL261 cells were injected subcutaneously at 3×10^6 cells in 0.1 ml PBS in the right hind limb of male C57BL/6J mice. Cobalt chloride was used to simulate hypoxia in xenograft tumors in vivo. After tumorigenization of mice, $CoCl_2$ aqueous solution with a concentration of 260 mg/l was prepared as drinking water for mice. When the diameter of tumor reached about 6-8 mm, the hypoxic transplanted tumors were subjected to 25 Gy X-ray irradiation (6 MV, 100 cGy/min) by a PRIMUS accelerator (SIEMENS Medical Solutions, Erlangen, Germany) at room temperature, while the normoxic transplanted tumors were subjected to 10 Gy X-ray irradiation. The mice in combined therapy group were intraperitoneally injected with 200 μl

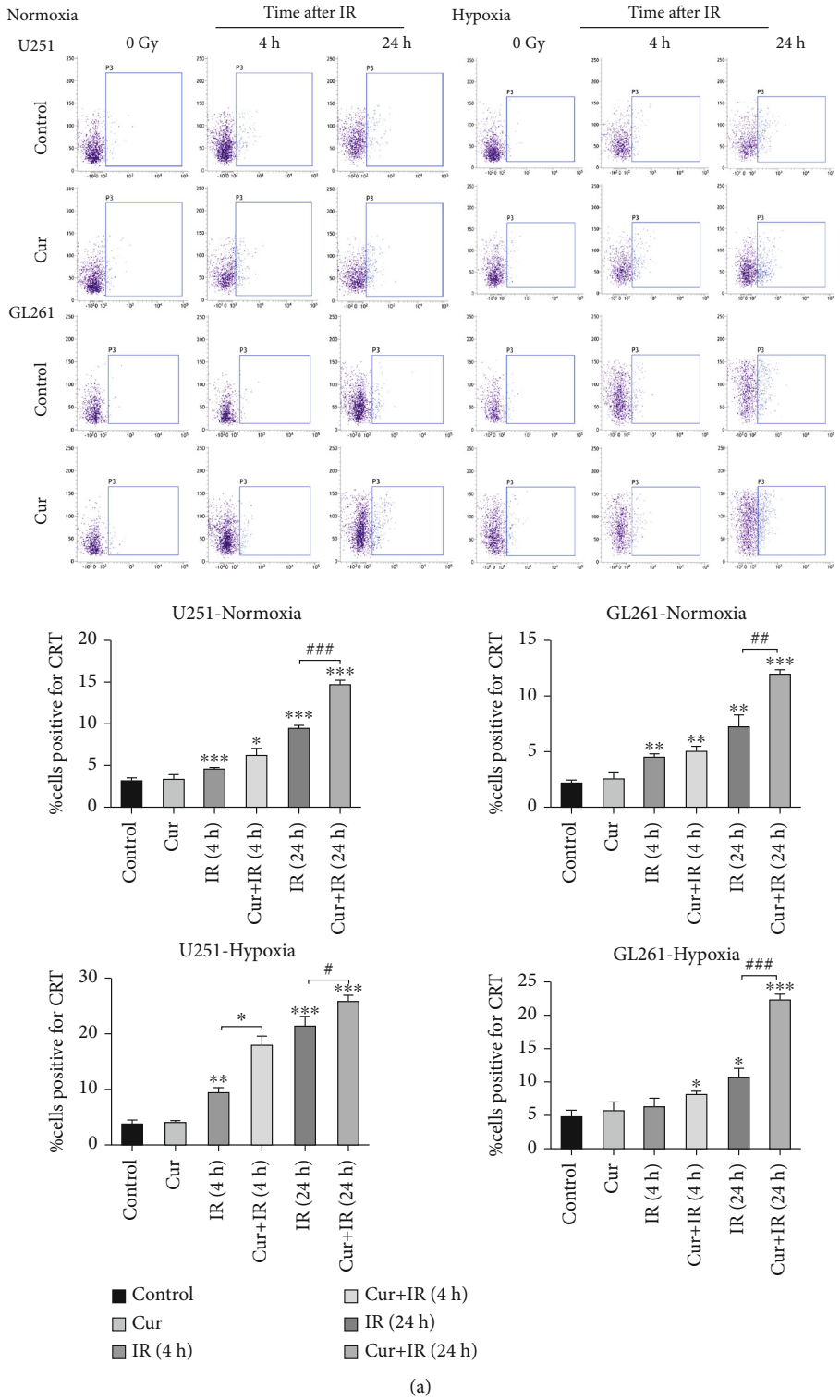

Figure 2: Continued.

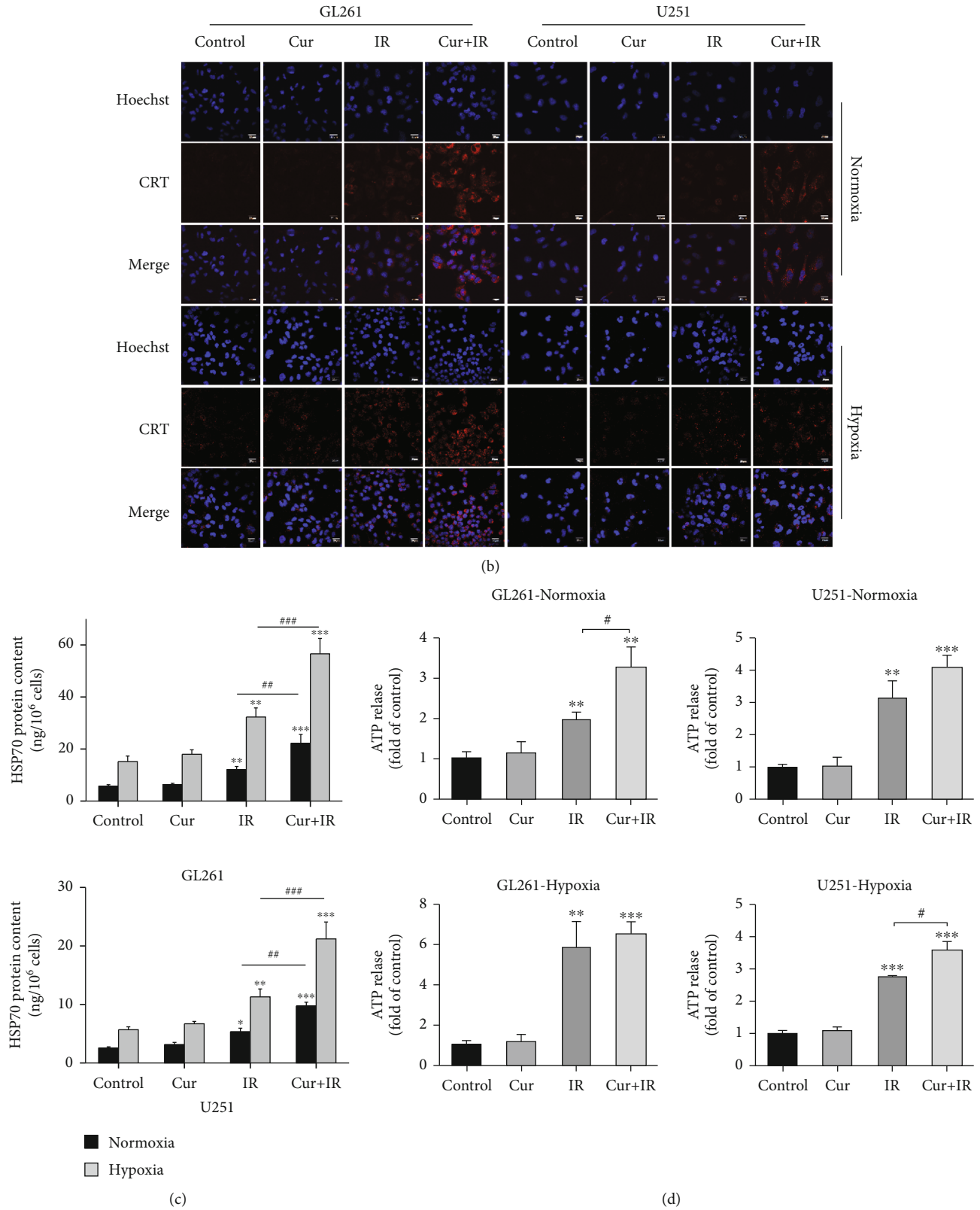

Figure 2: Continued.

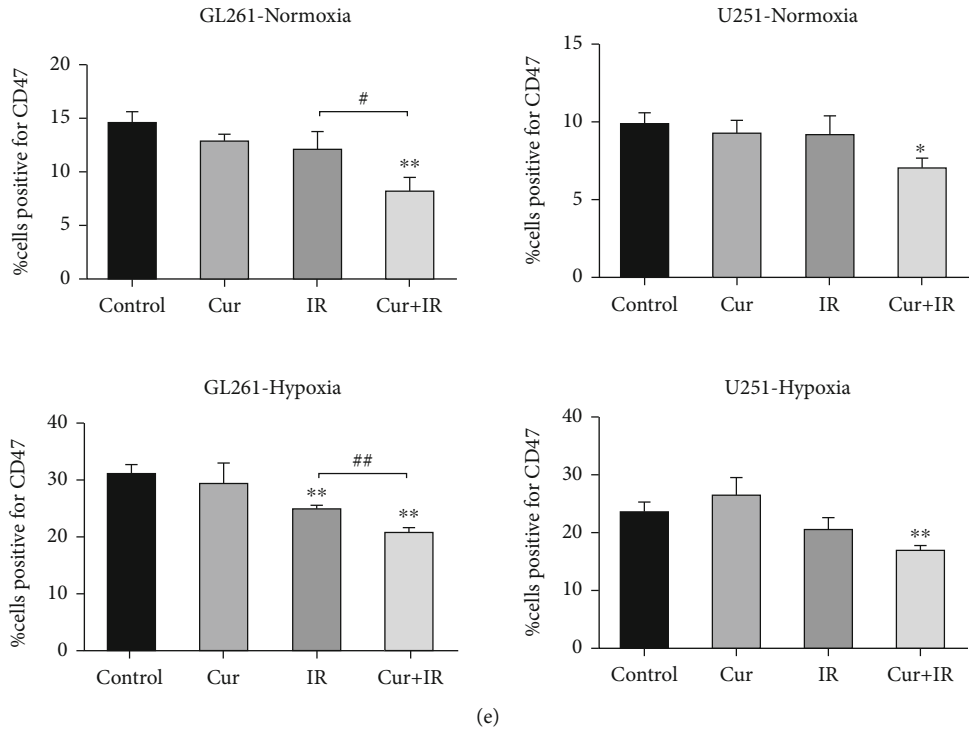

(e)

Figure 2: Curcumin enhanced IR-induced ICD-related DAMPs exposure or release. CRT exposure was assessed by flow cytometry (a) and immunofluorescence (b). HSP70 release (c) and ATP release (d) were detected by ELISA and chemiluminescent assay, respectively. (e) CD47 exposure was assessed by flow cytometry. $^{*}P < 0.05$, $^{**}P < 0.01$, and $^{***}P < 0.001$ vs. control; $^{\#}P < 0.05$, $^{\#\#}P < 0.01$, and $^{\#\#\#}P < 0.001$ vs. IR.

curcumin (50 μM) 24 hours before irradiation. All animal experimental protocols were approved by the institutional animal care and use committee and complied with the code of ethics for animal experimentation.

2.13. Immunohistochemical (IHC) Staining. The mice were sacrificed 48 hours after irradiation. Tumor tissues and spleen tissues were fixed in paraffin, imbedded, and cut for 4 mm sections. Tumor sections were incubated with primary antibodies, including anti-mouse CD4 (1 : 100, Cell Signaling), CD8 (1 : 100, Cell Signaling), CD11c (1 : 100, Cell Signaling), FoxP3 (1 : 100, Cell Signaling), CHOP (1 : 100, Cell Signaling), phospho-PERK (1 : 100, Invitrogen), p-IRE1-α (1 : 100; Invitrogen), and splicing XBP1 (1 : 100, Cell Signaling) antibodies, at 4°C overnight, and biotin-labeled secondary antibody for 30 min at 37°C. The final signal was developed using the 3,3′-diaminobenzidine (DAB) substrate, and the sections were observed under optical microscope. The percentage of positive cells was calculated as number of positive (brown) cells/total number of cells × 100 in 9 randomly selected fields (400×).

2.14. Statistical Analysis. GraphPad Prism 8 software was used for statistical analyses. The unpaired two-tailed t -test was used for comparison of data between two groups. For comparisons among more than two groups, one-way analysis of variance (ANOVA) followed by the Bonferroni posttest was performed. $P < 0.05$ was considered statistically significant.

3. Results

3.1. Curcumin Enhanced Apoptosis Induced by IR in Normoxic and Hypoxic Glioma Cells. GL261 and U251 cells were treated with various concentrations of curcumin for 24 h. The viability of glioma cells decreased (Figure 1(a)), while the apoptosis rate of glioma cells increased (Figures 1(b) and 1(c)) with the increase of curcumin concentration. 10 Gy IR alone could induce apoptosis of normoxic glioma cells but could not significantly induce apoptosis of hypoxic glioma cells. Compared with 10 Gy IR alone, treatment with 30 μM curcumin for 24 h before irradiation significantly increased the apoptosis of normoxic or hypoxic glioma cells. For hypoxic glioma cells, the apoptosis rate induced by 10 Gy IR+30 μM curcumin was similar to that induced by 25 Gy IR alone.

3.2. Curcumin Enhanced IR-Induced ICD-Related DAMP Exposure or Release. We detected CRT exposure on glioma cell surface using flow cytometry and immunofluorescence assay, respectively. The data showed CRT exposure on the surface of the cell membrane can be induced by IR. It occurred as early as 4 h after IR and was more significant at 24 h after IR (Figure 2(a)). Curcumin alone did not induce CRT cell surface exposure, whereas in normoxic and hypoxic glioma cells treated with curcumin prior to IR, CRT exposure was enhanced compared to IR alone (Figure 2(b)). Further, we assessed the release of ATP and HSP70 at 24 h after IR by chemiluminescent assay and ELISA, respectively. Compared with IR, both the

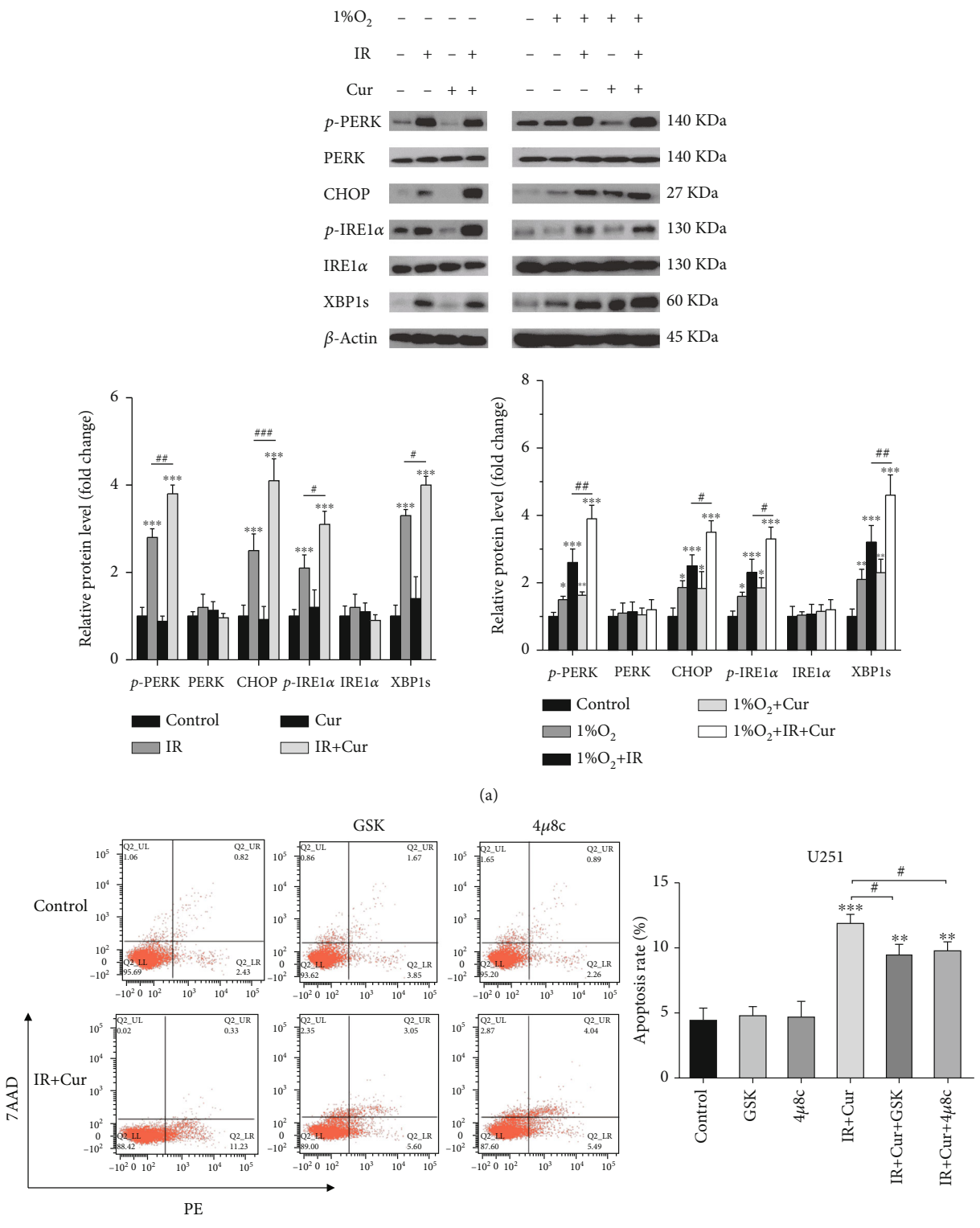

Figure 3: Continued.

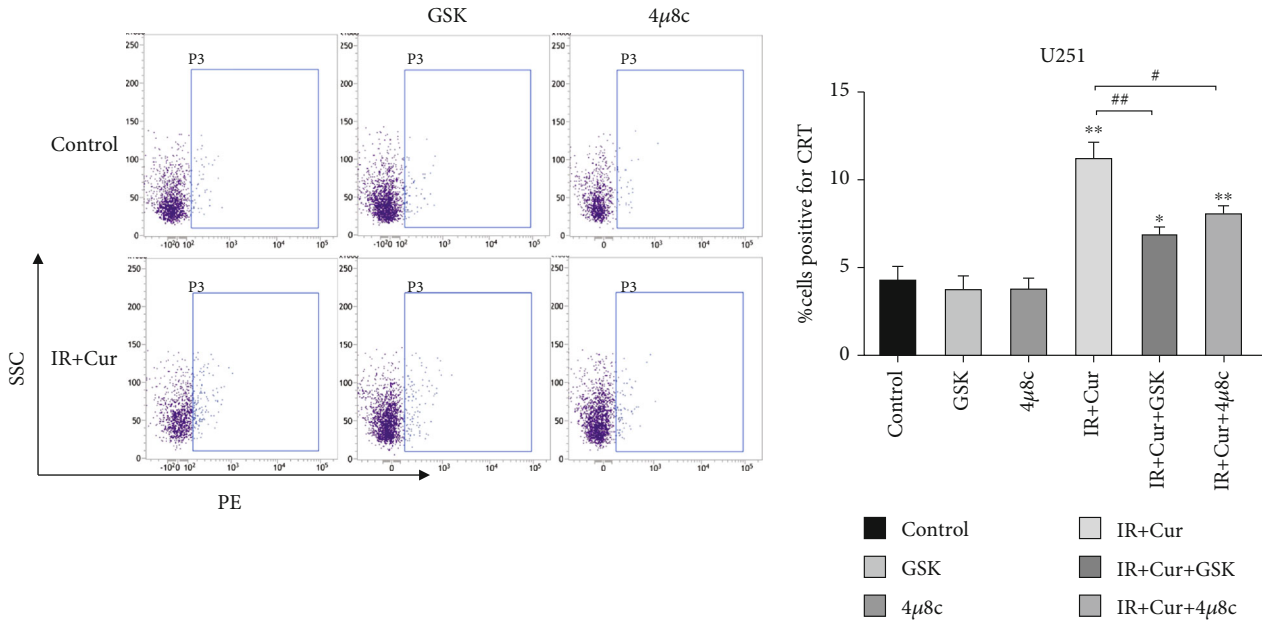

(c)

Figure 3: Curcumin enhanced IR-induced ICD by activating ER stress. (a) Curcumin increased the expressions of ER stress-related proteins in normoxic and hypoxic glioma. Cells were irradiated with 10 Gy/25 Gy IR after treatment with or without 30 μM curcumin for 24 h, and then, indicated protein expressions were assessed by WB. (b) Cell apoptosis was assessed with or without pretreatment with 2 μM GSK2606414 or 10 μM 4u8c for 1 h before irradiation. (c) Calreticulin exposure was analyzed by flow cytometry. $^{*}P < 0.05$, $^{**}P < 0.01$, and $^{***}P < 0.001$ vs. control; $^{\#}P < 0.05$ and $^{\#\#}P < 0.01$ vs. IR.

extracellular ATP and HSP70 were increased in the curcumin+IR group under normoxic or hypoxic condition (Figures 2(c) and 2(d)). These data indicated that the combination treatment of curcumin and IR promoted ATP and HSP70 release from the dying cells. In addition, CD47 on cell membrane was declined after combination treatment in normoxic and hypoxic glioma compared to IR alone (Figure 2(e)).

3.3. Curcumin Enhanced IR-Induced ICD by Activating ER Stress. ICD is related to ER stress, which is controlled by three unfolded protein response (UPR) sensors, protein kinase RNA-like ER kinase (PERK), inositol-requiring protein 1-α (IRE1-α), and activating transcription factor 6 (ATF6) [8]. To investigate the role of ER stress in IR-induced ICD, we used GSK2606414, a specific pharmacological inhibitor of PERK phosphorylation, and 4μ8c, a specific inhibitor of IRE1-α, to block UPR. As shown in Figure 3(a) and Supplementary Figure 1, treatment with curcumin for 24 hours prior to IR significantly increased PERK and IRE1α phosphorylation, as well as CHOP and XBP1 protein expression compared to IR alone. Hypoxia induced mild ER stress in glioma cells. These results indicated that PERK and IRE1α signaling pathways were activated by IR, which could be enhanced by curcumin. Furthermore, the addition of ER stress inhibitors reduced apoptosis and calreticulin exposure on the cell surface (Figures 3(b) and 3(c)). These results suggested that curcumin enhance IR-induced ICD via ER stress PERK and IRE1α signaling pathways.

3.4. Curcumin Augmented Chemotaxis and Phagocytosis of DCs to Irradiated Glioma Cells. U251 cells treated jointly by curcumin and IR attracted more DCs than the cells treated by IR alone (Figure 4(a)). The enhancement effect of curcumin on chemotaxis of DCs to irradiated glioma cells was observed at 12 h after irradiation and was more obvious at 24 h after irradiation under hypoxic condition. Next, DCs were labeled green and irradiated U251 cells were labeled red, and then, they were intermixed directly into complete medium to imitate the real intercellular response. As observed in Figure 4(b), DCs began to attached to U251 cells treated with IR alone; meanwhile, cells in the curcumin+IR group could be detected swallowed by DCs after coculture in normoxic or hypoxic condition for 8 h. These results suggested that curcumin accelerate the recognition and phagocytosis of irradiated glioma cells by DCs.

3.5. Curcumin Enhanced IR-Induced Glioma ICD In Vivo. In order to determine whether IR combined with curcumin can induce ICD in glioma, vaccination experiments in mouse models are required, which is the gold standard method for ICD [14]. Glioma cells treated with curcumin and/or X-rays were injected into the left hind limb of immunocompetent syngeneic mice subcutaneously. One week later, glioma cells were injected into the opposite hind limb, and mice were monitored for the rate of tumor formation and tumor size. As shown in Figure 5(b), it was found that all (5/5) mice in the control group developed tumors 12 days after inoculation with live tumor cells, with a tumor formation rate of 100%. Compared with the control group, X-ray-

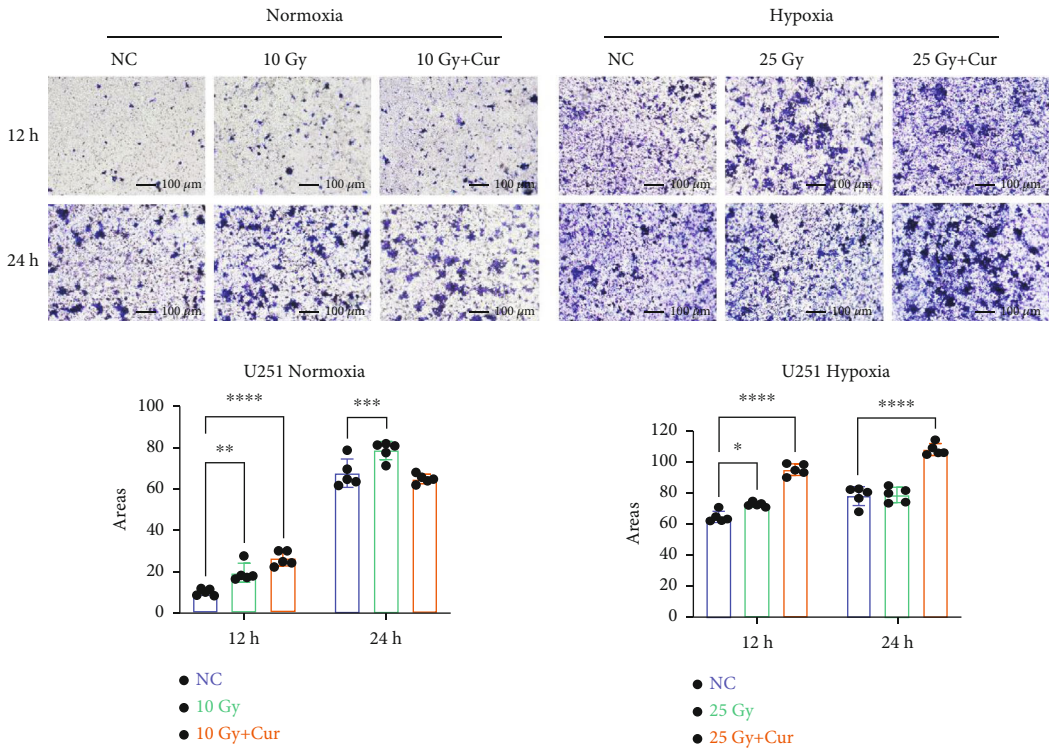

(a)

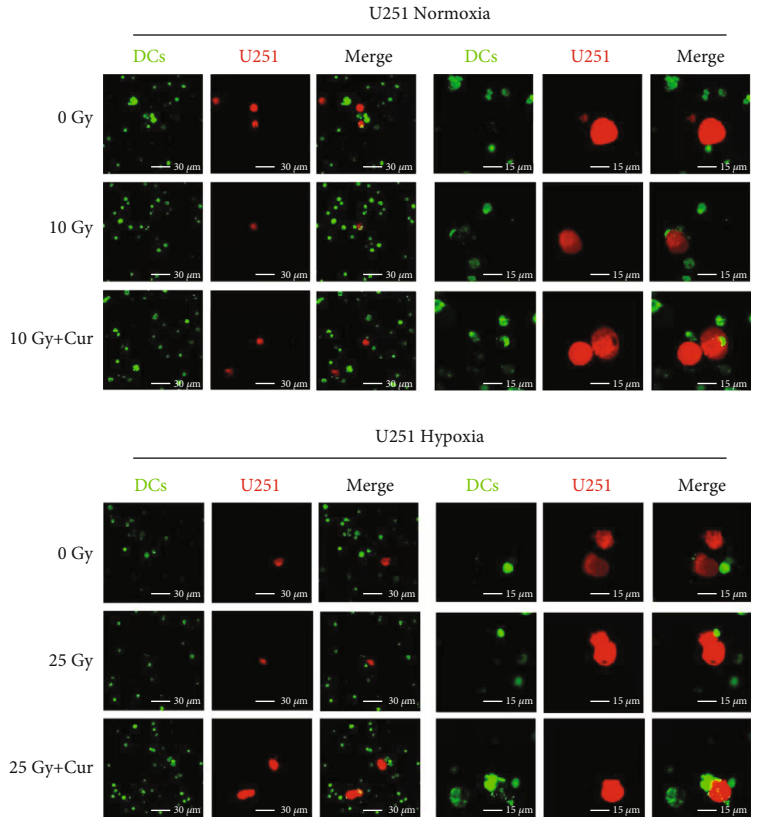

(b)

Figure 4: Curcumin augmented chemotaxis and phagocytosis of DCs to irradiated glioma cells. (a) U251 cells treated jointly by curcumin and IR attracted more DCs than the cells treated by IR alone. (b) Curcumin accelerated the recognition and phagocytosis of irradiated glioma cells by DCs. Cells in green represents DC cells, while cells in red represents U251 cells. The magnification of the photos on the right is twice bigger than the left ones.

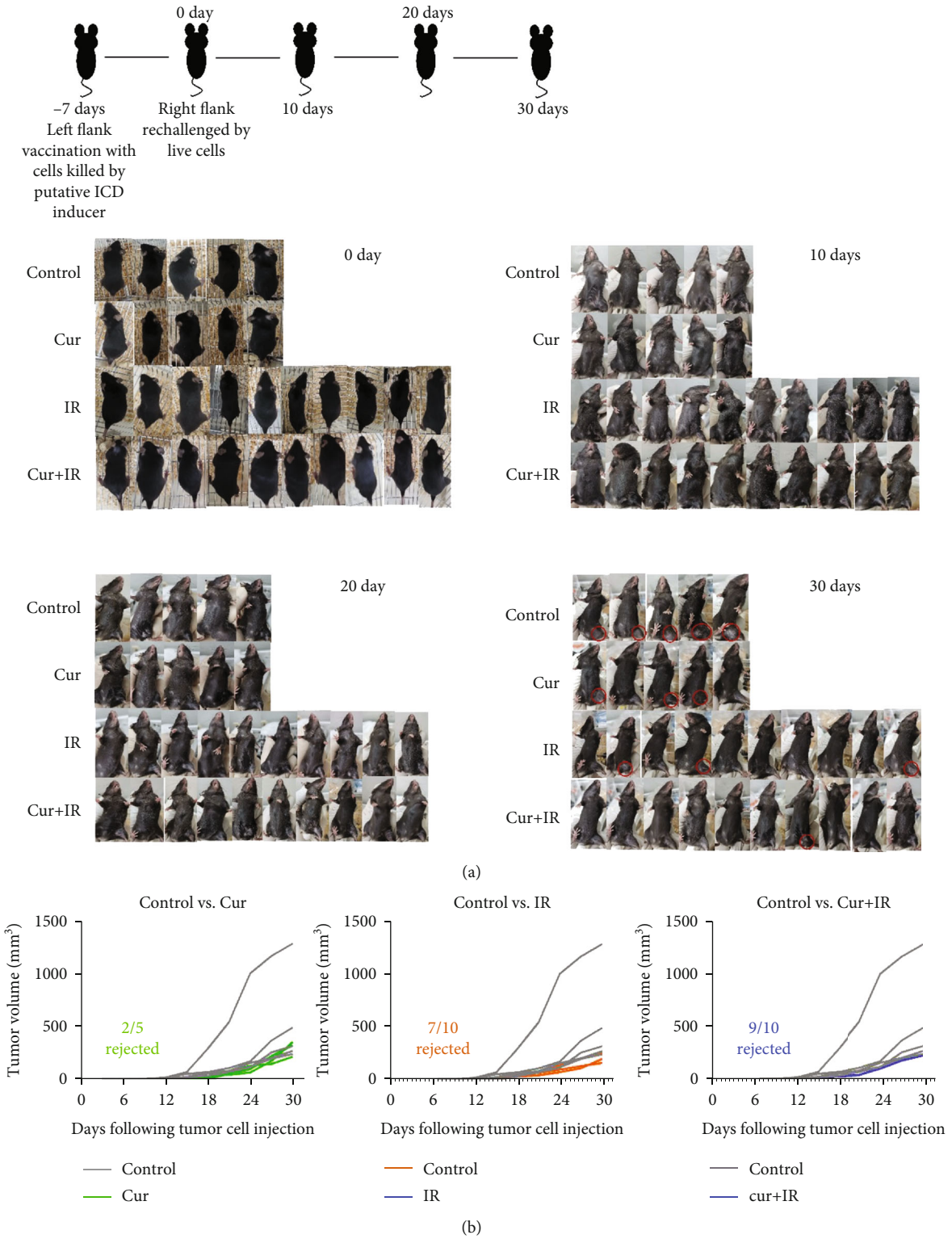

Figure 5: Continued.

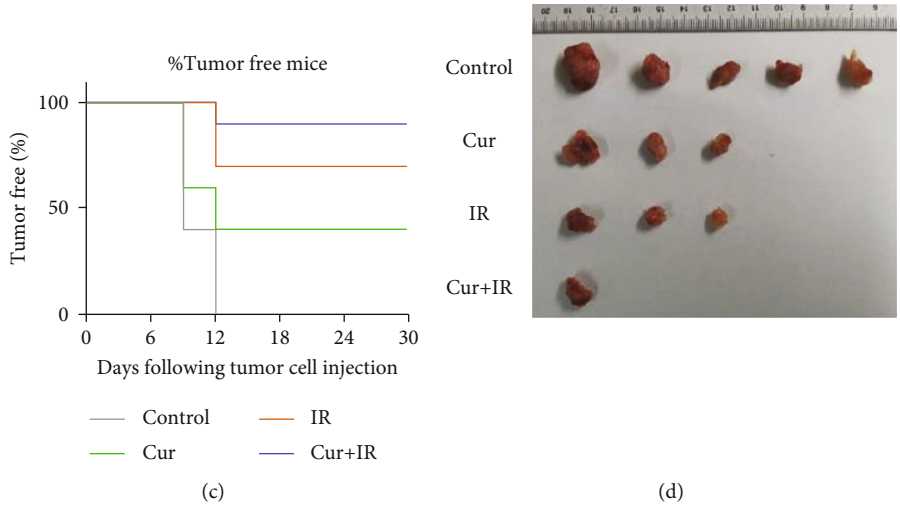

Figure 5: Curcumin enhanced IR-induced glioma ICD in vivo. (a) The schematic diagram and schedules of vaccination experiment. Tumors formed subcutaneously in mice 30 days after inoculation were shown in red circles. (b) Mice were subcutaneously injected with and glioma cells treated with 30 μM curcumin, 10 Gy X-ray, and both, respectively, and the control group was injected with PBS. One week later, tumor cells were injected into the contralateral side, and the tumor size was measured every 3 days. Each line represents a tumor-forming mouse. (c) Kaplan-Meier curves for the percentage of tumor free mice after inoculation with live tumor cells. All treatments significantly delayed or rejected tumor growth compared to control. $^{*}P < 0.05$, $^{**}P < 0.01$, and $^{***}P < 0.001$ vs. control; $^{\#}P < 0.05$, and $^{\#\#}P < 0.01$ vs. IR. (d) Tumor photos 30 days after inoculation.

irradiated glioma cells induced antitumor immunity in 70% (7/10) of the mice, rejecting tumor formation. Compared with IR alone, 90% (9/10) of the mice treated with the combination of IR and curcumin did not form tumors, and the tumors that did form appeared later and were smaller than those in the control group (Figures 5(c) and 5(d)). These data indicated that the combination treatment of IR and curcumin induced stronger tumor immune rejection in mice than IR alone, suggesting that curcumin enhance IR-induced glioma ICD in vivo.

3.6. Curcumin Enhanced IR-Mediated Immune Cell Infiltration in Tumor Tissue. As shown in Figure 6(a), curcumin treatment before local irradiation of the tumor site induced the production of more CD8+ T cells in the spleen, and the number of tumor-infiltrating CD8+ T lymphocytes was also significantly increased. However, tumor-infiltrating CD8+ T cells did not increase in the hypoxic tumor model, probably due to the killing effect of high-dose radiation on T lymphocytes. Next, we detected the CD4+ and CD8+ T cell subsets, as well as the dendritic cell marker CD11c and regulatory T cell (Treg) marker FoxP3 expression in spleen tissues and tumor tissues by immunohistochemistry. As shown in Figure 6(b), curcumin further increased IR-induced infiltration of CD4+ T cells, CD8+ T cells, and CD11c+ dendritic cells in the spleen tissues and decreased immunosuppressive FoxP3+ regulatory T cells. In normoxic tumor tissues (Figure 6(c)), the infiltration of CD4+ T cells, CD8+ T cells, and CD11c+ dendritic cells was more significant in the combined treatment group than the IR alone group, while the infiltration of FoxP3+ regulatory T cells showed no significant changes. In the hypoxic xenograft tissues, CD4+ T cells and CD11c+ dendritic cells were increased in the combined treatment group than the IR alone group, but CD8+ T cells and FoxP3+ regulatory T cells showed no significant changes between them. As shown in Figure 6(d), curcumin further increased IR-induced ER stress marker p-PERK, CHOP, p-IRE1α, and XBP1 expression in both normoxic tumor tissues and hypoxic tumor tissues. This in vivo result verified the role of ER stress signaling in curcumin's enhancing effect on IR-induced ICD in glioma.

4. Discussion

Glioma is a common primary intracranial tumor with a 5-year relative survival rate of about 5% [15]. Although surgery, chemotherapy, radiotherapy, and other treatments can be used, glioma is still one of the poorest prognosis malignant tumors due to its high invasiveness and recurrence [16]. Curcumin is a kind of natural flavonoid, which can not only reduce the toxicity of radiotherapy to normal tissues but also increase the radiotherapy-induced death of cancer cells [17, 18]. Curcumin can make glioma and other tumors sensitive to radiotherapy and chemotherapy drugs [19]. This study proved that curcumin could increase the radiation-induced apoptosis in normoxic or hypoxic glioma cells.

ICD is a special regulated apoptotic cell death [20, 21]. Different from the general case in which apoptosis is immune silences, this type of apoptosis induces ROS production and ER stress by some chemical and physical factors and releases certain molecules to activate the immune system [22, 23]. ICD is accompanied by exposure or release of DAMPs including CRT, ATP, and HSP70/90 [22, 24–27]. These molecules can recruit antigen presenting cells (APC) to deliver antigens to the host immune system and initiate antitumor immunity [6, 28]. Our experimental results showed that curcumin significantly enhanced IR-induced

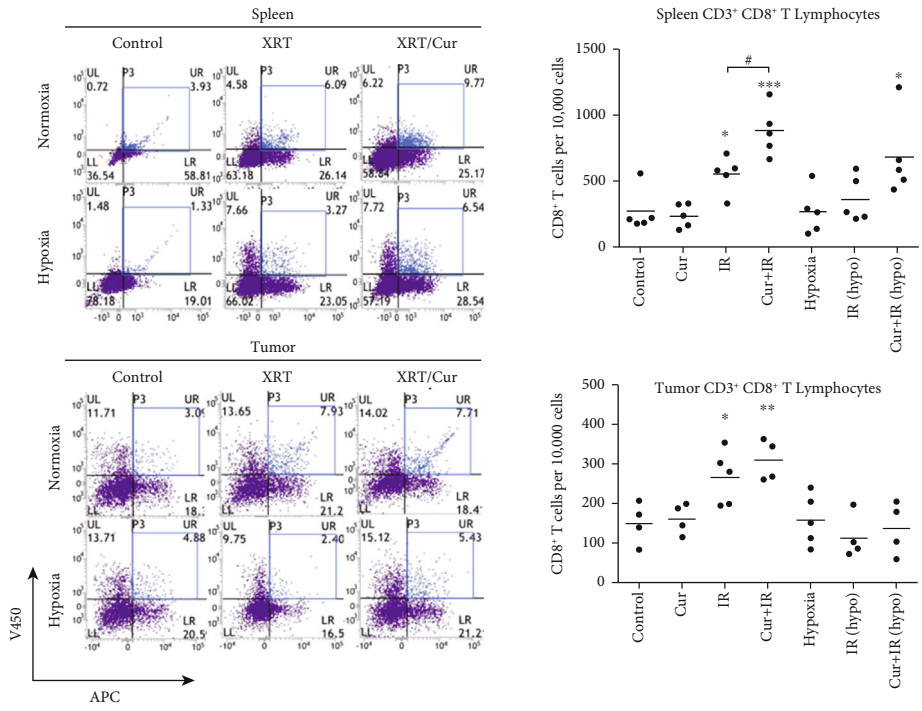

(a)

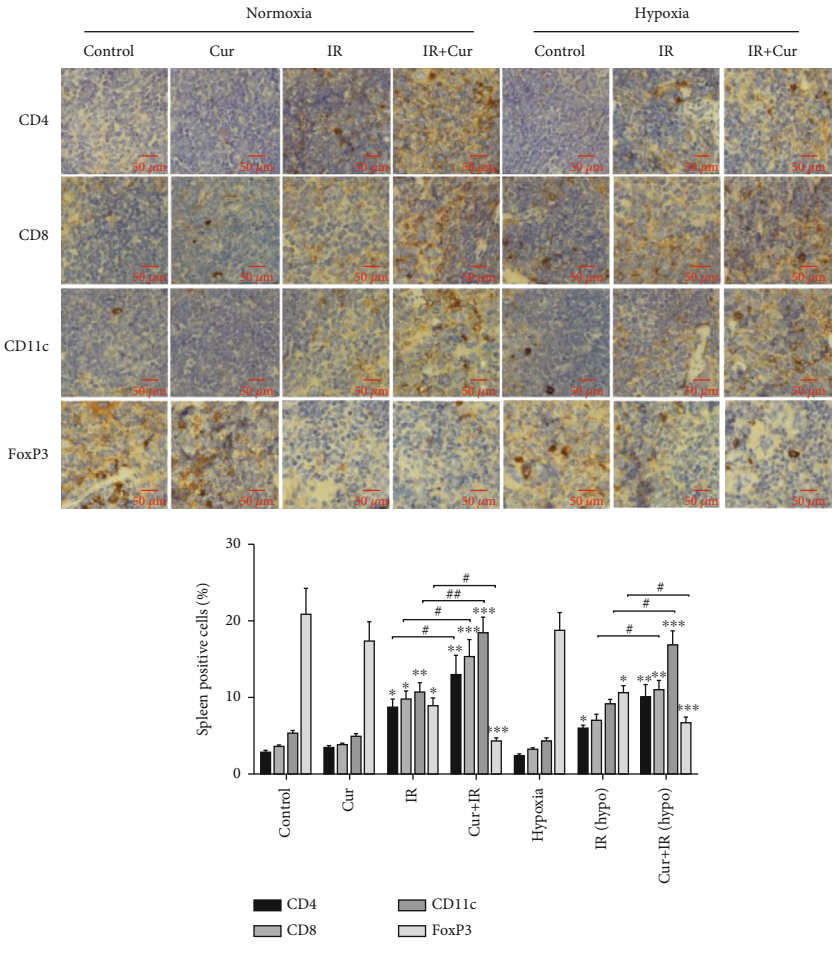

(b)

Figure 6: Continued.

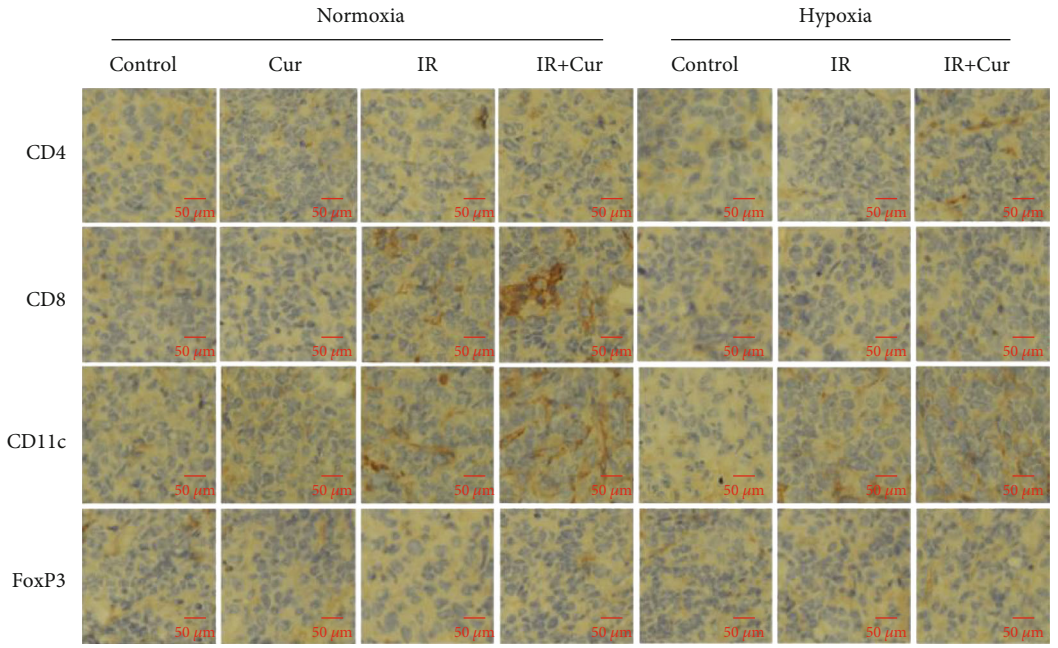

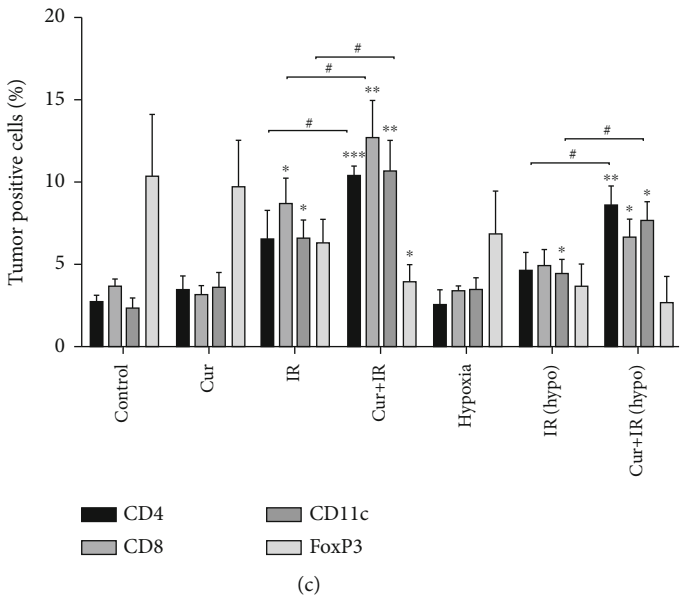

(c)

Figure 6: Continued.

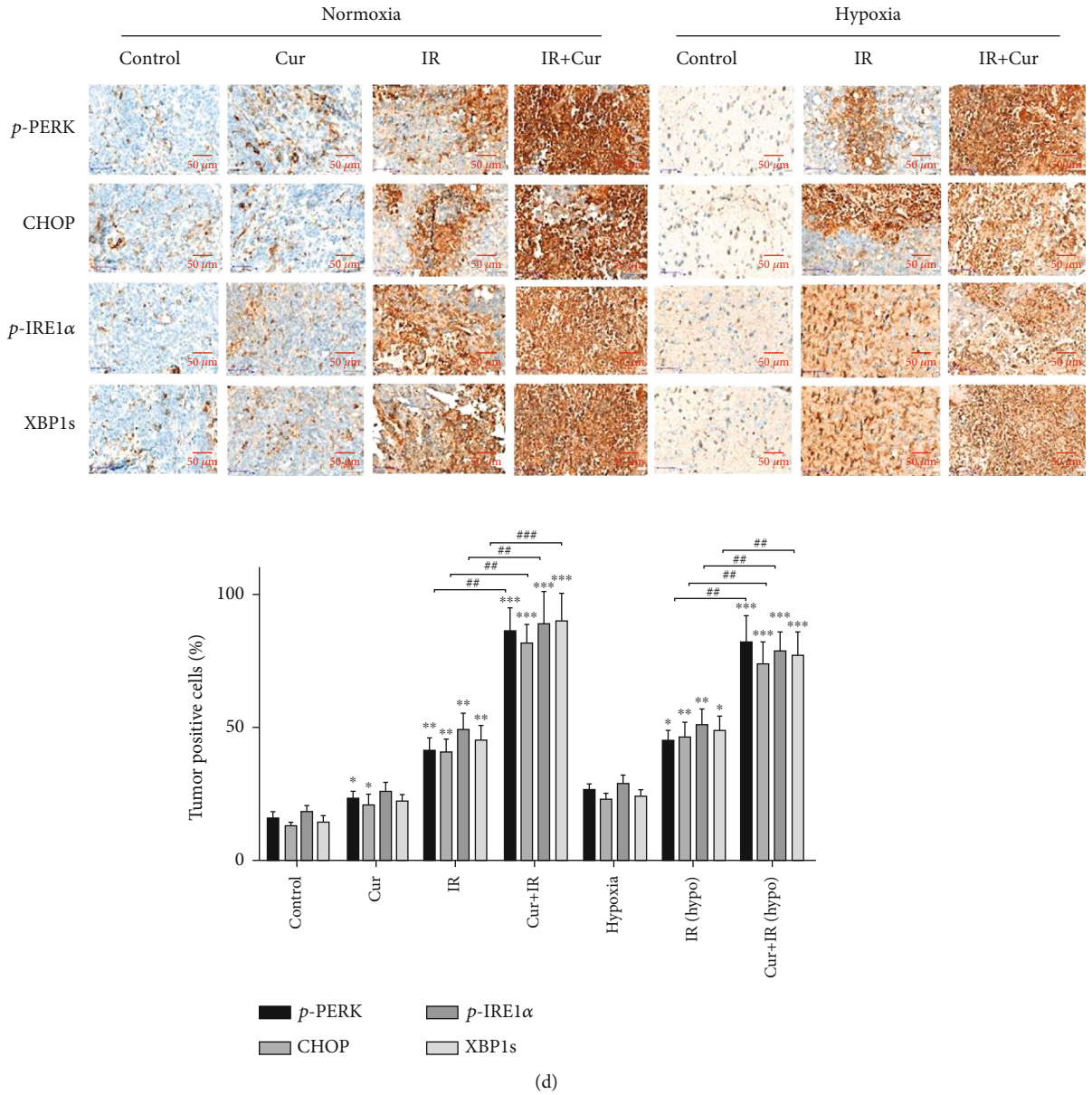

Figure 6: Curcumin enhanced IR-mediated immune cell infiltration in tumor tissue. (a) Mice with normoxic or hypoxic tumor grafts were treated with curcumin and X-ray, and then, tumor and spleen cells were collected. CD3+ and CD8+ T cells were detected by flow cytometry. The number of CD8+ T cells per 10,000 cells was counted. (b) For immunohistochemical staining, immune subsets were shown using anti-CD4, CD8, CD11c, and FoxP3 antibodies in the spleen. (c) For immunohistochemical staining, immune subsets were shown using anti-CD4, CD8, CD11c, and FoxP3 antibodies in tumor tissues. (d) ER stress marker p-PERK, CHOP, p-IRE1α, and XBP1 expression were detected by immunohistochemical staining in tumor tissues. $^{*}P < 0.05$, $^{**}P < 0.01$, and $^{***}P < 0.001$ vs. control; $^{\#}P < 0.05$, $^{\#\#}P < 0.01$, and $^{\#\#\#}P < 0.001$ vs. IR.

calreticulin exposure, which was a powerful "eat me" signal that interacted with phagocytes to assist in phagocytosis of cancer cells [24]. We also found that IR could induce ATP and HSP70 release from glioma cells and curcumin significantly promoted the IR-induced release. Our results showed that hypoxia induced more CD47 production. It was worth noting that curcumin could reduce CD47 expression on the irradiated glioma cell surface, alleviate the "don't eat me" signal, and help to activate a stronger immune response. Although curcumin was not an immunogenic cell death inducer in itself, it could significantly enhance the irradiation-induced DAMP exposure or release.

The occurrence of ICD requires ER stress. ER function can be disturbed by a variety of pathological stimuli, such as hypoxia, irradiation, oxidative stress, nutrient or glucose deficiency, and viral infection [29]. These disturbances can alter or break endoplasmic reticulum homeostasis, resulting in ER stress and the production of misfolded proteins. In the absence of ER stress, the BiP protein, also known as glucose regulatory protein GRP78, binds to three sensors, PERK,

IRE1, and ATF6, keeps these proteins in an inactive state, and prevents them from activating [30]. However, in the break of endoplasmic reticulum homeostasis or Ca2+ imbalance, BiP isolates from these sensors and these three transmembrane proteins are activated through dimerization and autophosphorylation, leading to the activation of downstream UPR signaling pathway [31]. When cells fail to respond to ER stress, apoptosis is activated. The C/EBP homologous protein (CHOP) plays a vital role by regulating antiapoptotic and proapoptotic proteins to induce apoptosis [32, 33]. We found that irradiation induced the activation of PERK and IRE1 signaling pathways and upregulated the downstream proapoptotic transcription factor CHOP and the transcription activator XBP1s. These could be further enhanced by curcumin. GSK2606414, a PERK specific inhibitor, is effective in preventing PERK autophosphorylation [34]. 4μ8C can bind to the IRE1 active site and selectively inactivate XBP1 splicing and IRE1-mediated mRNA degradation [35]. We found that cell apoptosis and CRT exposure induced by the combination treatment of curcumin and X-ray reduced after PERK or IRE1 inhibition with corresponding inhibitor. The results indicated that the combination treatment of curcumin and IR induced immunogenic cell death of glioma cells through ER stress PERK-eIF2α and IRE1α-XBP1 signaling pathways.

Vaccination trials can verify the occurrence of ICD in vivo [14]. This experiment required immune-complete homologous host mice. Tumor cells were treated with a potential ICD inducer in vitro and used as a vaccine and then inoculated with tumor cells 1-2 weeks later to monitor tumor formation rate and tumor size. If there is no tumor, it indicates that antitumor immune rejection has occurred in vivo. The ability of mice to reject tumors represents the degree of ICD [7, 36, 37]. Because the traditional in vitro hypoxia method (1% O_2, 5% CO_2, and 94% N_2) was not suitable for hypoxic tumor bearing mouse model, we used cobalt chloride ($CoCl_2$) chemical simulation to induce hypoxia in vivo. $CoCl_2$ can stabilize HIF-1α and produce a reaction similar to hypoxia [38]. Therefore, as a drug to simulate hypoxia, $CoCl_2$ is often used to induce hypoxia in vitro and in vivo [39]. We confirmed the occurrence of irradiation-induced ICD in glioma cells through in vivo vaccination experiments, and curcumin could further enhance irradiation-induced ICD via ER stress pathways and produce immune response. Compared to irradiation alone, the combination treatment of curcumin and radiation promoted the infiltration of CD4+ T cells, CD8+ T cells, and CD11c+ dendritic cells in the spleen and tumor tissues of mice and effectively enhanced the antitumor immunity.

5. Conclusions

In conclusion, IR combined with curcumin induced normoxic or hypoxic glioma cells ICD in vitro and in vivo, providing a new avenue for enhancing DC activation and antitumor immunity. These data provide a rationale for curcumin combined with radiotherapy and/or immunotherapy for glioma patients who failed conventional radiotherapy and chemotherapy.

Data Availability

Research data are stored in an institutional repository and will be shared upon request to the corresponding author.

Conflicts of Interest

The authors declare no conflict of interest.

Acknowledgments

We are grateful to Collaborative Innovation Center of Radiological Medicine of Jiangsu Higher Education Institutions and a project funded by the Priority Academic Program Development of Jiangsu Higher Education Institutions (PAPD). This work was supported by the National Natural Science Foundation of China (Nos. 32171234, 31870844, and 81874080).

Supplementary Materials

Supplementary Figure 1: full membrane western blot images of ER stress PERK and IRE1α signaling pathway-associated proteins. *(Supplementary Materials)*

References

[1] R. Stupp, W. P. Mason, M. J. van den Bent et al., "Radiotherapy plus concomitant and adjuvant temozolomide for glioblastoma," *The New England Journal of Medicine*, vol. 352, no. 10, pp. 987–996, 2005.

[2] R. G. Verhaak, K. A. Hoadley, E. Purdom et al., "Integrated genomic analysis identifies clinically relevant subtypes of glioblastoma characterized by abnormalities in PDGFRA, IDH1, EGFR, and NF1," *Cancer Cell*, vol. 17, no. 1, pp. 98–110, 2010.

[3] P. Vaupel, A. Mayer, and M. Höckel, "Tumor hypoxia and malignant progression," *Methods in Enzymology*, vol. 381, pp. 335–354, 2004.

[4] B. G. Wouters and J. M. Brown, "Cells at intermediate oxygen levels can be more important than the "hypoxic fraction" in determining tumor response to fractionated radiotherapy," *Radiation Research*, vol. 147, no. 5, pp. 541–550, 1997.

[5] P. Vandenabeele, K. Vandecasteele, C. Bachert, O. Krysko, and D. V. Krysko, "Immunogenic apoptotic cell death and anticancer immunity," *Advances in Experimental Medicine and Biology*, vol. 930, pp. 133–149, 2016.

[6] B. Montico, A. Nigro, V. Casolaro, and J. Dal Col, "Immunogenic apoptosis as a novel tool for anticancer vaccine development," *International Journal of Molecular Sciences*, vol. 19, no. 2, p. 594, 2018.

[7] M. Obeid, A. Tesniere, F. Ghiringhelli et al., "Calreticulin exposure dictates the immunogenicity of cancer cell death," *Nature Medicine*, vol. 13, no. 1, pp. 54–61, 2007.

[8] A. D. Garg, S. Martin, J. Golab, and P. Agostinis, "Danger signalling during cancer cell death: origins, plasticity and regulation," *Cell Death and Differentiation*, vol. 21, no. 1, pp. 26–38, 2014.

[9] F. Ghiringhelli, L. Apetoh, A. Tesniere et al., "Activation of the NLRP3 inflammasome in dendritic cells induces IL-1beta-dependent adaptive immunity against tumors," *Nature Medicine*, vol. 15, no. 10, pp. 1170–1178, 2009.

[10] H. L. Matlung, K. Szilagyi, N. A. Barclay, and T. K. van den Berg, "The CD47-SIRPα signaling axis as an innate immune checkpoint in cancer," *Immunological Reviews*, vol. 276, no. 1, pp. 145–164, 2017.

[11] E. Abdollahi, A. A. Momtazi, T. P. Johnston, and A. Sahebkar, "Therapeutic effects of curcumin in inflammatory and immune-mediated diseases: a nature-made jack-of-all-trades?," *Journal of Cellular Physiology*, vol. 233, no. 2, pp. 830–848, 2018.

[12] S. Kizaka-Kondoh, M. Inoue, H. Harada, and M. Hiraoka, "Tumor hypoxia: a target for selective cancer therapy," *Cancer Science*, vol. 94, no. 12, pp. 1021–1028, 2003.

[13] S. S. Zheng, X. H. Chen, X. Yin, and B. H. Zhang, "Prognostic significance of HIF-1α expression in hepatocellular carcinoma: a meta-analysis," *PLoS One*, vol. 8, no. 6, article e65753, 2013.

[14] O. Kepp, L. Senovilla, I. Vitale et al., "Consensus guidelines for the detection of immunogenic cell death," *Oncoimmunology.*, vol. 3, no. 9, article e955691, 2014.

[15] Q. T. Ostrom, L. Bauchet, F. G. Davis et al., "The epidemiology of glioma in adults: a "state of the science" review," *Neuro-Oncology*, vol. 16, no. 7, pp. 896–913, 2014.

[16] S. H. Shahcheraghi, M. Zangui, M. Lotfi et al., "Therapeutic potential of curcumin in the treatment of glioblastoma multiforme," *Current Pharmaceutical Design*, vol. 25, no. 3, pp. 333–342, 2019.

[17] R. Yahyapour, D. Shabeeb, M. Cheki et al., "Radiation protection and mitigation by natural antioxidants and flavonoids: implications to radiotherapy and radiation disasters," *Current Molecular Pharmacology*, vol. 11, no. 4, pp. 285–304, 2018.

[18] S. J. Hosseinimehr, "Flavonoids and genomic instability induced by ionizing radiation," *Drug Discovery Today*, vol. 15, no. 21-22, pp. 907–918, 2010.

[19] A. Goel and B. B. Aggarwal, "Curcumin, the golden spice from Indian saffron, is a chemosensitizer and radiosensitizer for tumors and chemoprotector and radioprotector for normal organs," *Nutrition and Cancer*, vol. 62, no. 7, pp. 919–930, 2010.

[20] G. Kroemer, L. Galluzzi, O. Kepp, and L. Zitvogel, "Immunogenic cell death in cancer therapy," *Annual Review of Immunology*, vol. 31, no. 1, pp. 51–72, 2013.

[21] L. Galluzzi, I. Vitale, S. A. Aaronson et al., "Molecular mechanisms of cell death: recommendations of the Nomenclature Committee on Cell Death 2018," *Cell Death and Differentiation*, vol. 25, no. 3, pp. 486–541, 2018.

[22] A. D. Garg, L. Galluzzi, L. Apetoh et al., "Molecular and translational classifications of DAMPs in immunogenic cell death," *Frontiers in Immunology*, vol. 6, article 588, 2015Published 2015 Nov 20.

[23] Y. J. Wang, R. Fletcher, J. Yu, and L. Zhang, "Immunogenic effects of chemotherapy-induced tumor cell death," *Genes Dis.*, vol. 5, no. 3, pp. 194–203, 2018.

[24] A. D. Garg, D. V. Krysko, T. Verfaillie et al., "A novel pathway combining calreticulin exposure and ATP secretion in immunogenic cancer cell death," *The EMBO Journal*, vol. 31, no. 5, pp. 1062–1079, 2012.

[25] J. Fucikova, L. Kasikova, I. Truxova et al., "Relevance of the chaperone-like protein calreticulin for the biological behavior and clinical outcome of cancer," *Immunology Letters*, vol. 193, pp. 25–34, 2018.

[26] I. Martins, Y. Wang, M. Michaud et al., "Molecular mechanisms of ATP secretion during immunogenic cell death," *Cell Death and Differentiation*, vol. 21, no. 1, pp. 79–91, 2014.

[27] P. Scaffidi, T. Misteli, and M. E. Bianchi, "Release of chromatin protein HMGB1 by necrotic cells triggers inflammation," *Nature*, vol. 418, no. 6894, pp. 191–195, 2002.

[28] H. Inoue and K. Tani, "Multimodal immunogenic cancer cell death as a consequence of anticancer cytotoxic treatments," *Cell Death and Differentiation*, vol. 21, no. 1, pp. 39–49, 2014.

[29] J. A. Diehl, S. Y. Fuchs, and C. Koumenis, "The cell biology of the unfolded protein response," *Gastroenterology*, vol. 141, no. 1, pp. 38–41.e2, 2011.

[30] D. Ron and P. Walter, "Signal integration in the endoplasmic reticulum unfolded protein response," *Nature Reviews. Molecular Cell Biology*, vol. 8, no. 7, pp. 519–529, 2007.

[31] Y. Kimata and K. Kohno, "Endoplasmic reticulum stress-sensing mechanisms in yeast and mammalian cells," *Current Opinion in Cell Biology*, vol. 23, no. 2, pp. 135–142, 2011.

[32] R. Sano and J. C. Reed, "ER stress-induced cell death mechanisms," *Biochimica et Biophysica Acta*, vol. 1833, no. 12, pp. 3460–3470, 2013.

[33] R. Iurlaro and C. Muñoz-Pinedo, "Cell death induced by endoplasmic reticulum stress," *The FEBS Journal*, vol. 283, no. 14, pp. 2640–2652, 2016.

[34] J. M. Axten, J. R. Medina, Y. Feng et al., "Discovery of 7-methyl-5-(1-{[3- (trifluoromethyl)phenyl]acetyl}-2,3-dihydro-1H-indol-5-yl)-7H-pyrrolo[2,3-d]pyrimidin-4-amine (GSK2606414), a potent and selective first-in-class inhibitor of protein kinase R (PKR)-like endoplasmic reticulum kinase (PERK)," *Journal of Medicinal Chemistry*, vol. 55, no. 16, pp. 7193–7207, 2012.

[35] B. C. Cross, P. J. Bond, P. G. Sadowski et al., "The molecular basis for selective inhibition of unconventional mRNA splicing by an IRE1-binding small molecule," *Proceedings of the National Academy of Sciences of the United States of America*, vol. 109, no. 15, pp. E869–E878, 2012.

[36] L. Menger, E. Vacchelli, S. Adjemian et al., "Cardiac glycosides exert anticancer effects by inducing immunogenic cell death," *Science Translational Medicine*, vol. 4, no. 143, p. 143ra99, 2012.

[37] A. Q. Sukkurwala, S. Adjemian, L. Senovilla et al., "Screening of novel immunogenic cell death inducers within the NCI mechanistic diversity set," *Oncoimmunology.*, vol. 3, no. 4, article e28473, 2014.

[38] V. T. Ho and H. F. Bunn, "Effects of transition metals on the expression of the erythropoietin gene: further evidence that the oxygen sensor is a heme protein," *Biochemical and Biophysical Research Communications*, vol. 223, no. 1, pp. 175–180, 1996.

[39] M. J. Gray, J. Zhang, L. M. Ellis et al., "HIF-1alpha, STAT3, CBP/p300 and Ref-1/APE are components of a transcriptional complex that regulates Src-dependent hypoxia-induced expression of VEGF in pancreatic and prostate carcinomas," *Oncogene*, vol. 24, no. 19, pp. 3110–3120, 2005.

Hindawi
Oxidative Medicine and Cellular Longevity
Volume 2022, Article ID 7608712, 22 pages
https://doi.org/10.1155/2022/7608712

Research Article

Dysregulation of EZH2/miR-138-5p Axis Contributes to Radiosensitivity in Hepatocellular Carcinoma Cell by Downregulating Hypoxia-Inducible Factor 1 Alpha (HIF-1α)

Bing Bai,[1] **Ying Liu**,[2] **Xue-Mei Fu**,[3] **Hai-Yan Qin**,[4] **Gao-Kai Li**,[2] **Hai-Chen Wang**,[1] **and Shi-Long Sun**[1]

[1]*NHC Key Laboratory of Radiobiology, School of Public Health, Jilin University, Changchun, Jilin 130021, China*
[2]*Department of Toxicology, School of Public Health, Jilin University, Changchun, Jilin 130021, China*
[3]*Jilin Women and Children Health Hospital, Changchun, Jilin 130061, China*
[4]*Department of Plastic Surgery, China-Japan Union Hospital of Jilin University, Changchun, Jilin 130031, China*

Correspondence should be addressed to Shi-Long Sun; slsun@jlu.edu.cn

Received 14 June 2022; Revised 24 July 2022; Accepted 3 August 2022; Published 29 August 2022

Academic Editor: Lu Cai

Enhancer of zeste homolog 2 (EZH2) is a histone methyltransferase involved in cell proliferation, invasion, angiogenesis, and metastasis in various cancers, including hepatocellular carcinoma (HCC). However, the role and molecular mechanisms of EZH2 in HCC radiosensitivity remain unclear. Here, we show that EZH2 is upregulated in HCC cells and the aberrantly overexpressed EZH2 is associated with the poor prognosis of HCC patients. Using miRNA databases, we identified miR-138-5p as a regulator of EZH2. We also found that miR-138-5p was suppressed by EZH2-induced H3K27me3 in HCC cell lines. MiR-138-5p overexpression and EZH2 knockdown enhanced cellular radiosensitivity while inhibiting cell migration, invasion, and epithelial-mesenchymal transition (EMT). Analysis of RNA-seq datasets revealed that the hypoxia-inducible factor-1 (HIF-1) signaling pathway was the main enrichment pathway for differential genes after miR-138-5p overexpression or EZH2 knockdown. Expression level of HIF-1α was significantly suppressed after miR-138-5p overexpression or silencing of EZH2. HIF-1α silencing mitigated resistance of HCC cells and inhibited EMT. This study establishes the EZH2/miR-138-5p/HIF-1α as a potential therapeutic target for sensitizing HCC to radiotherapy.

1. Introduction

Hepatocellular carcinoma (HCC) is one of the malignant tumors with high mortality in the world [1]. Surgical resection is the first-line treatment for patients with early-stage HCC [2], but those with advanced-stage disease are unsuitable for surgery [3]. In recent years, advanced radiation therapy, such as stereotactic body radiation therapy (SBRT), has shown high efficiency in suppressing locoregional HCC. Such treatment necessitates the development of radiation sensitizers to enhance the therapeutic ratio and clinical outcomes.

Enhancer of zeste homolog 2 (EZH2), the catalytic subunit of polycomb repressor complex 2 (PRC2), specifically trimethylates histone 3 at lysine 27 (H3K27me3) and functions as a transcriptional repressor via chromatin modification [4]. Several studies have reported the utility of EZH2 as a potential therapeutic target for HCC owing to its marked upregulation in HCC and correlation with poor prognosis of HCC [5–7]. The HCC-promoting role of EZH2 stems from its regulation on epigenetic silencing of signal transducer and activator of transcription 3 (STAT3), TGF-beta, and Wnt pathway via inhibitors, such as axis inhibition protein 2 (AXIN2) and prickle planar cell polarity protein 1 (PRICKLE1) [8–10]. Although the lysine methyltransferase activity of EZH2 is considered majorly related to its cancer regulatory role, EZH2 may also regulate HCC through other mechanisms [11, 12]. Silencing EZH2 has been found to effectively inhibit malignant behaviors of tumor cells, which has hence spurred tremendous efforts to

find novel and efficient EZH2 inhibitors [13, 14]. One of such inhibitors is miR-138-5p, which is a noncoding RNA that can suppress the progressive behavior of HCC cells [15, 16].

Hypoxia is a common tumor biomarker, and hypoxic tumor cells activate stress response pathways to adapt to the low oxygen level. Tumor cells under hypoxia adapt via altering their gene expression to facilitate their survival and even proliferation. These processes contribute to the cancer cells' aggressive phenotype and resistance to therapy [17]. Reduced sensitivity of hypoxic tumor cells to radiotherapy is one of the factors contributing to poor clinical outcomes [18]. Chen et al. found that hypoxia increases the expression of HIF-2α via the PI3K-AKT-mTOR pathway, which contributes to HCC progression [19].

The hypoxia-inducible factor (HIF) is a heterodimer composed of three different oxygen-sensitive HIFα subunits (HIF-1α, HIF-2α, and HIF-3α) and a constitutively expressed β-subunit. HIF-1α and HIF-2α heterodimers function as transcriptional activators of oxygen-regulated target genes [20]. Transcriptional regulation of different genes by HIF-1α in hypoxic cells may contribute differentially to the malignant phenotype in cancer cells. Studies have shown that inhibition of HIF-1 leads to metabolic changes that enhance radiation therapy efficacy [21]. Yang et al. reported that HIF-1 downregulation by siRNA enhanced the radiosensitivity of hypoxic HCC cells [22], suggesting that the combined treatment using HIF-1 inhibitors and radiotherapy enhances the anticancer effect on HCC.

Therefore, the present study strived to investigate the role of the EZH2/miR-138-5p axis on the radiosensitivity of HCC. Our study provided evidence that EZH2 expression is regulated by miR-138-5p, which in turn is epigenetically downregulated by EZH2 through a double-negative feedback loop in HCC cells. Moreover, EZH2/miR-138-5p negative correlation is significantly associated with radiosensitivity in HCC patients through inhibiting HIF-1α.

2. Materials and Methods

2.1. Cell Culture and Transfection. Human liver cancer cell lines HepG2 and Hep3B, as well as HEK-293 T cells, were purchased from Cell Bank of the Chinese Academy of Sciences (Shanghai, China), cultured in DMEM/MEM medium supplemented with 10% fetal bovine serum (FBS) and 1% penicillin/streptomycin, and placed at 37 °C in a humidified incubator containing 5% CO_2.

Mimic of miR-138-5p, S: AGCUGGUGUUGUGAAU CAGGCCG, AS: GCCUGAUUCAC AACACCAGCUUU, the mimic negative control (NC), S: UUCUCCGAACGU GUCACGUTT, AS: ACGUGACACGUUCGGAGAATT, and siRNA of HIF-1α (ACCCUAACUAG CCGAGGAAG AATT) were acquired from GenePharma Co., Ltd. (GenePharma, Shanghai, China). Their sequences are shown in Table 1. Lentivirus vector and EZH2-shRNA/vector plasmid were used to build HepG2-shEZH2/HepG2-vector model.

Cells were sowed into 6-well plates (about 2×10^6 cells/well) and transfected with aforementioned nucleotides or plasmids when confluence reached 60-70% using Sage LipoplusTM (Sagecreation, Beijing, China) referring to manufacturer's recommendations.

Table 1: Sequences of the primers used for RT-qPCR and ChIP-qPCR.

Gene	Sequences (5′-3′)
miR-138-5p-F	TGACCGAGCTGGTGTTGTG
miR-138-5p-R	CAGAGCAGGGTCCGAGGTA
U6 snRNA-F	CGCTTCGGCAGCACATATAC
U6 snRNA-R	TTCACGAATTTGCGTGTCATC
EZH2-F	TGGTCTCCCCTACAGCAGAA
EZH2-R	TCATCTCCCATATAAGGAATGTTATG
GAPDH-F	GTGAAGGTCGGAGTCAACG
GAPDH-R	TGAGGTCAATGAAGGGGTC
HIF-1α-F	TAAGTTCTGAACGTCGAAAAGA
HIF-1α-R	CAGCATCCAGAAGTTTCCTC
ChIP-qPCR primer	
miR-138-5p-1-F	CCATTGTTTCTCTGCACCCC
miR-138-5p-1-R	GTGGCTCCTCCGGTTTTGAG
miR-138-5p-2-F	CACCTGGCTGGGAGTTCTT
miR-138-5p-2-R	CTATTGCAGTCCTGGTCCTC

2.2. Real-Time Quantitative PCR. Total RNA was extracted using the Trizol (Thermo Fisher Scientific, Waltham, MA, USA). For mRNA quantification, cDNA was synthesized using the PrimeScript RT Reagent Kit (TaKaRa, Shiga, Japan) and detected using the SYBR Green PCR Mastermix (Solarbio, Beijing, China) following the manufacturer's protocols. For miRNA quantification, cDNA was synthesized and measured using the Hairpin-it microRNA and U6 snRNA Normalization RT-qPCR Quantitation Kit (GenePharma, Shanghai, China). The primers used for hsa-miR-138-5p and U6 were obtained from GenePharma. Primer sequences are listed in Table 1.

2.3. Bioinformatics Analysis. We performed expression analyses of genes using TCGA data through the ULCAN portal (http://ualcan.path.uab.edu/index.html) [23]. And the survival graphs were downloaded and processed from the Kaplan-Meier plotter portal (http://kmplot.com/analysis) [24]. We searched for targets of has-miR-138-5p using several target prediction algorithms databases, including PicTar, miRanda, miRTarBase, and TargetScan.

2.4. Dual-Luciferase Reporter Gene Assay. HEK-293 T cells (1×10^4 cells per well) were seeded in 96-well culture plates and co-transfected with 200 ng EZH2-3′UTR or EZH2-3′ UTR-Mut vectors and miRNA mimic or NC (10 pM) using LipoPlus™ Reagent (Sagecreation, Beijing, China). Forty-eight hours later, HEK-293 T cells were collected, and the luciferase activity changes of miR-138-5p on EZH2-3′UTR were measured using a dual-luciferase assay kit (Promega, Madison, WI, USA) by a luminometer fluorescence detector (BioTek, Biotek Winooski, Vermont, USA).

2.5. Western Blot. Total protein of cells was extracted by using RIPA buffer containing protease inhibitors (Solarbio, Beijing, China). Protein concentration was quantified using Enhanced BCA Protein Assay Kit (Beyotime Biotechnology, Shanghai, China). The total proteins (30 μg for each) were separated using 10% SDS-PAGE and transferred to polyvinylidene fluoride membranes. Following blocking with 5% skimmed milk at room temperature for 1 h, the membrane was incubated primary antibodies at 4°C overnight. After incubation with primary antibodies, membranes were washed with TBST followed by HRP-conjugated secondary antibodies for 1 hour at room temperature. These bands were detected using ECL solution (Solarbio, Beijing, China).

2.6. Clonogenic Assay. Seed a predetermined number of cells in a 6-well culture plate. After 24 hours, cells were treated with a series of radiation doses (0, 2, 4, 6, and 8 Gy) (Model X-RAD320iX; Precision X-Ray, Inc., North Branford, CT, USA). After incubating these cells at 37°C for 7-10 days, they were washed twice with PBS, fixed with formaldehyde and finally stained with crystal violet solution. Count the number of colonies containing ≥50 cells, colony formation efficiency = (number of colonies/number of inoculated cells) × 100%. Survival fraction (SF) was calculated by normalizing the clonogenic efficiency of the control group. We fit cell survival curves according to standard linear quadratic (LQ) models using GraphPad Prism 5 (GraphPad Software, LaJolla, CA, USA).

2.7. Wound Healing Assay. Wound healing assay is used to detect cell migration ability. The cells are spread on 6-well plates and transfected when the cells reach at 80% confluence. After 48 h of transfection, scrape the cells with a 200 μl pipette tip. Use DMEM or MEM supplemented for cell culture to reduce the potential impact of cell proliferation on the final result. Fixed point image acquisition was performed at 0 h, 24 h, and 48 h, respectively.

2.8. Transwell Invasion Assay. Transwell invasion assay detects cell invasion ability. After 48 h of transfection, cells were resuspended in serum-free DMEM or MEM and transferred to the transwell chamber. The total volume of liquid in the chamber was 200 μl, and 550 μl of complete medium was injected out of the chamber. After 24 h incubation, the culture medium was discarded, washed twice with PBS, fixed with 4% paraformaldehyde for 20 min, and washed twice with PBS. Finally, stain with 0.1% crystal violet for 30 min, wash twice with PBS, and observe the cells under a microscope.

2.9. Flow Cytometry. After 48 hours of transfection, the logarithmic growth phase cells were centrifuged at 1500 rpm for 5 minutes, and the supernatant was discarded. After adding PBS, centrifuge at 1500 rpm for 5 minutes. Repeat the operation. After that, cells should be fixed in ice-cold 70% ethanol for at least 1 h. Using PI Solution (Meilunbio Biotech, Dalian, China), prepare a cell suspension with a cell concentration of 1×10^6 cells/ml using the prepared 1 × PI Solution. After 30 minutes of incubation in the dark, it was detected within 1 hour. For the test of apoptosis, annexin V-FITC (Meilunbio, Biotech, Dalian, China) binding solution was added before PI solution, and it was detected within 1 hour. 2′,7′-dichlorofluorescein diacetate (DCFH-DA, Solarbio, Beijing, China) was used for detection of intracellular ROS.

2.10. Chromatin Immunoprecipitation (ChIP) Assay. ChIP was performed using a ChIP-IT® Express Enzymatic Shearing Kit (Active Motif, Carlsbad, CA, USA) on cells. Briefly, protein-DNA complexes were cross-linked by incubating cells in 1% formaldehyde-containing medium for 10 min. Cell pellets were resuspended in lysis buffer with protease inhibitors. Cells were digested by restriction endonuclease, in order to shear DNA to fragments about 200 bps. Samples were taken at this point as positive controls in the RT-qPCR reaction (input chromatin). Next, cells were incubated with monoclonal antibody against H3K27me3 (Abcam, Cambridge, MA, USA) overnight at 4°C. Human purified IgG was used as control antibody (Immunoway, Newark, Delaware, USA). DNA-protein complexes were collected using Protein A/G Magnetic beads (MedChem Express, Monmouth Junction, NJ, USA), followed by washing, elution, and reverse cross-linking. DNAs were purified with Chromatin IP DNA Purification Kit (Active Motif, Carlsbad, CA, USA). Recovered DNAs were resuspended in TE buffer and were later analyzed by RT-qPCR (Primers are shown in Table 1).

2.11. RNA-Seq Analysis. For RNA-seq, we divided HepG2 cells into four groups, transfected with shEZH2/vector plasmid or miR-138-5p mimic/NC. RNA isolation, library construction, and sequencing were performed on a BGISEQ-500 (Beijing Genomic Institution, BGI). The sequencing data analysis, including heat map clustering, Venn diagram creation, gene ontology (GO) analysis, and Kyoto Encyclopedia of Genes and Genomes (KEGG) analysis, was performed using BGI Dr. Tom 2.0.

2.12. Statistical Analysis. SPSS 24.0 and GraphPad Prism 5 was applied. All measurement data are expressed as mean ± standard deviation (SD) or standard error of the mean (SEM), with at least three independent replications. The comparison between two groups was conducted by independent-samples t test. Kaplan-Meier (K-M) curve was used to analyze the relationship between the expression of miR-138-5p, EZH2, and the 5-year survival rate of HCC patients, and the log rank test was used for variance analysis. p value less than 0.05 was considered to indicate statistical significance: $*p < 0.05$ and $**p < 0.01$.

3. Results

3.1. Expression Levels of EZH2 and miR-138-5p Are Associated with HCC Prognosis. In order to explore the role of miR-138-5p and EZH2 in HCC, we compared their expression in HCC specimens and adjacent nontumor liver tissue in The Cancer Genome Atlas (TCGA) dataset. Our results showed that the expression of EZH2 mRNA in HCC primary tumor tissue ($n = 371$) was significantly higher than that in liver tissue adjacent to the tumor ($n = 50$) (Figure 1(a)). Expression of EZH2 was found to be significantly higher in tumors of higher grades compared to

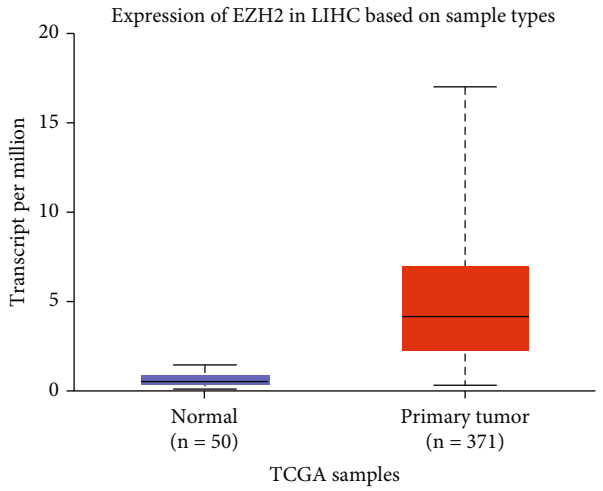

(a)

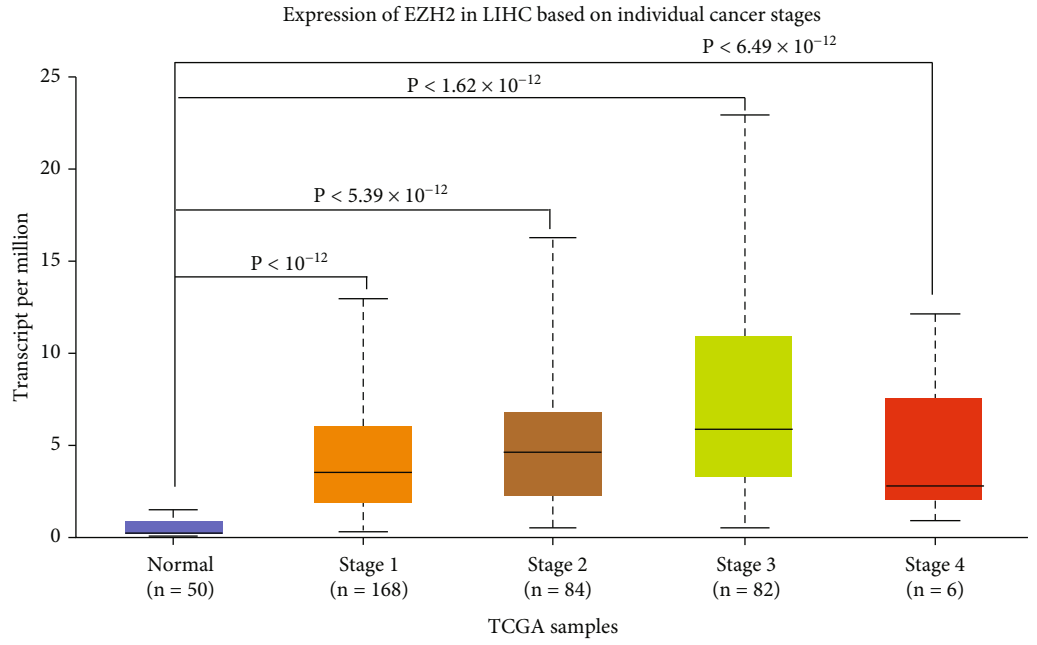

(b)

Figure 1: Continued.

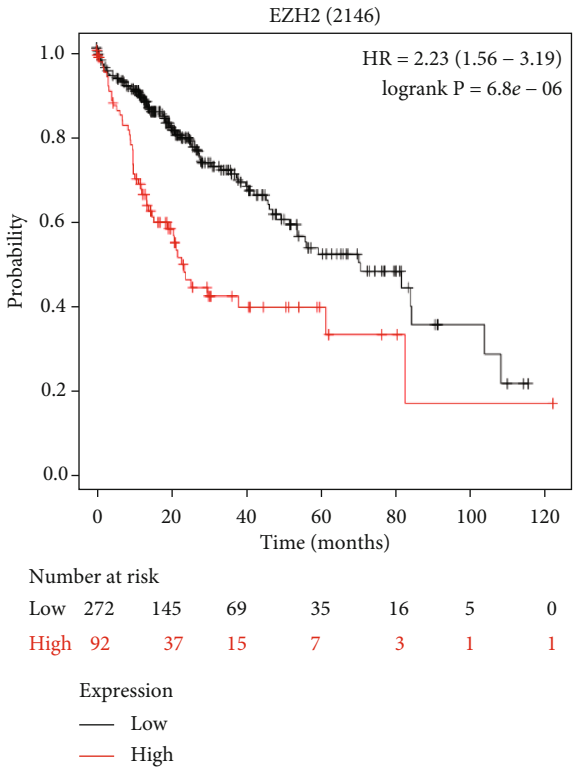

(c)

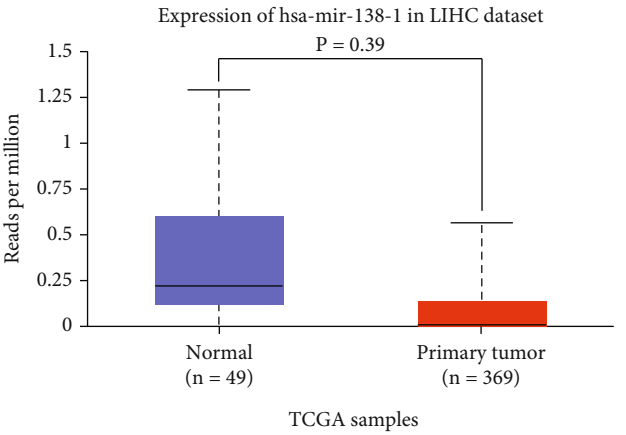

(d)

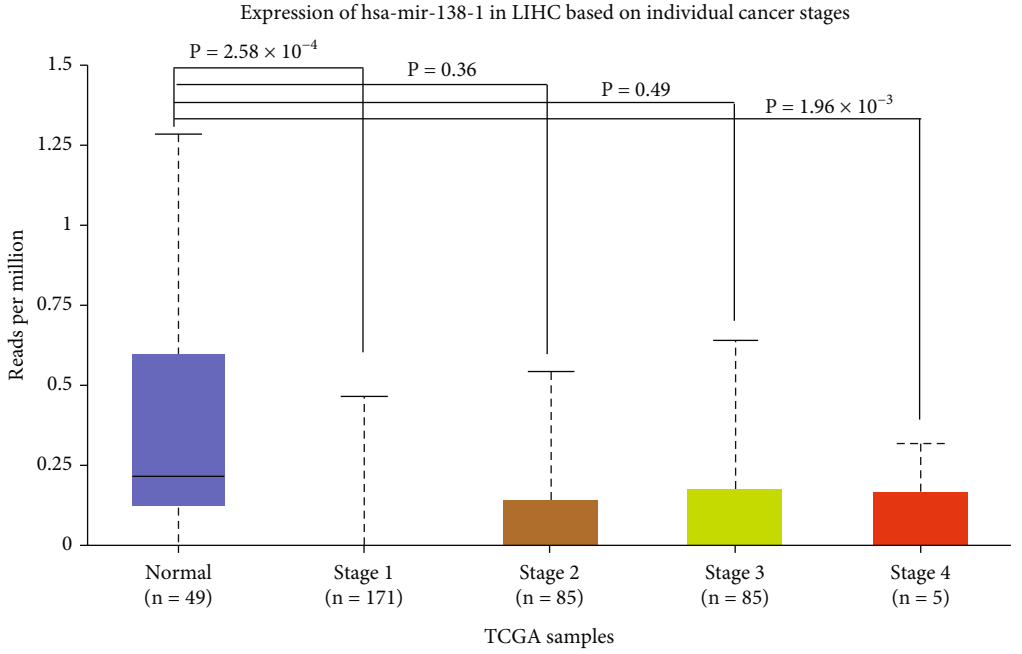

(e)

Figure 1: Continued.

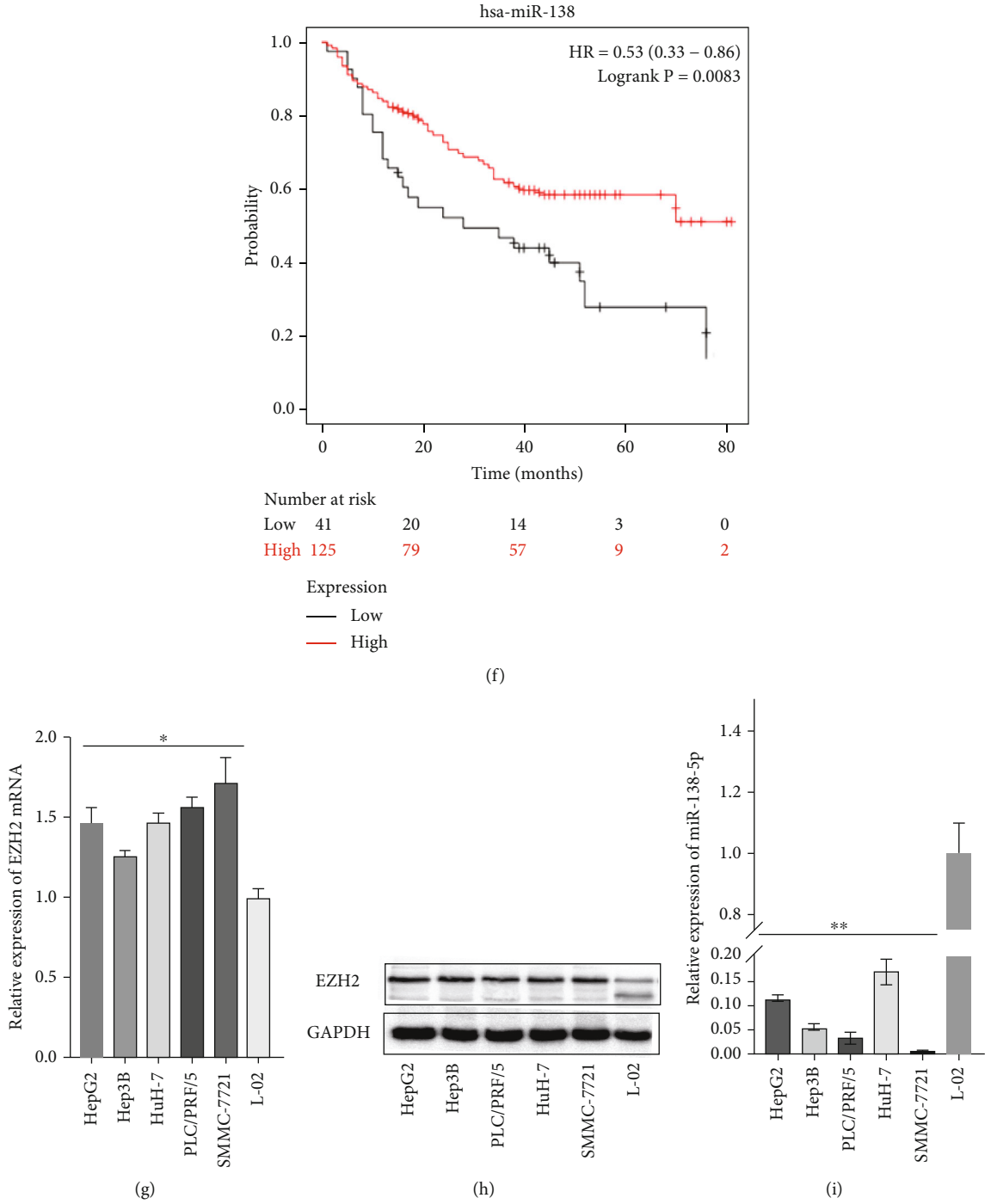

Figure 1: Expression of EZH2, miR-138-5p in subgroups of liver cancer patients with different prognoses and validation in vitro. (a) The plot shows EZH2 mRNA expression level between HCC specimens and liver tissue. (b) The plot shows EZH2 mRNA expression level in grades 1-4 HCC patients. (c) EZH2 expression was correlated with poorer OS in the HCC cohort of the Kaplan Meier plotter database. (d) The plot shows miR-138-5p expression level between HCC specimens and liver tissue. (e) The plot shows miR-138-5p expression levels in grades 1-4 HCC patients. (f) The level of miR-138-5p expression was correlated with poorer OS in the HCC cohort of the Kaplan Meier plotter database. (g) EZH2 mRNA expression was measured in five HCC cells (HepG2, Hep3B, Huh-7, PLC/PRF/5, and SMMC-7721) and immortalized human liver cell line L-02. (h) EZH2 protein expression was measured in five HCC cells (HepG2, Hep3B, Huh-7, PLC/PRF/5, and SMMC-7721) and immortalized human liver L-02 cell line. (i) Level of miR-138-5p expression was tested in five HCC cells (HepG2, Hep3B, Huh-7, PLC/PRF/5, and SMMC-7721) and immortalized human liver cell line L-02. $^{*}p < 0.05$, $^{**}p < 0.01$ (compared to L-02).

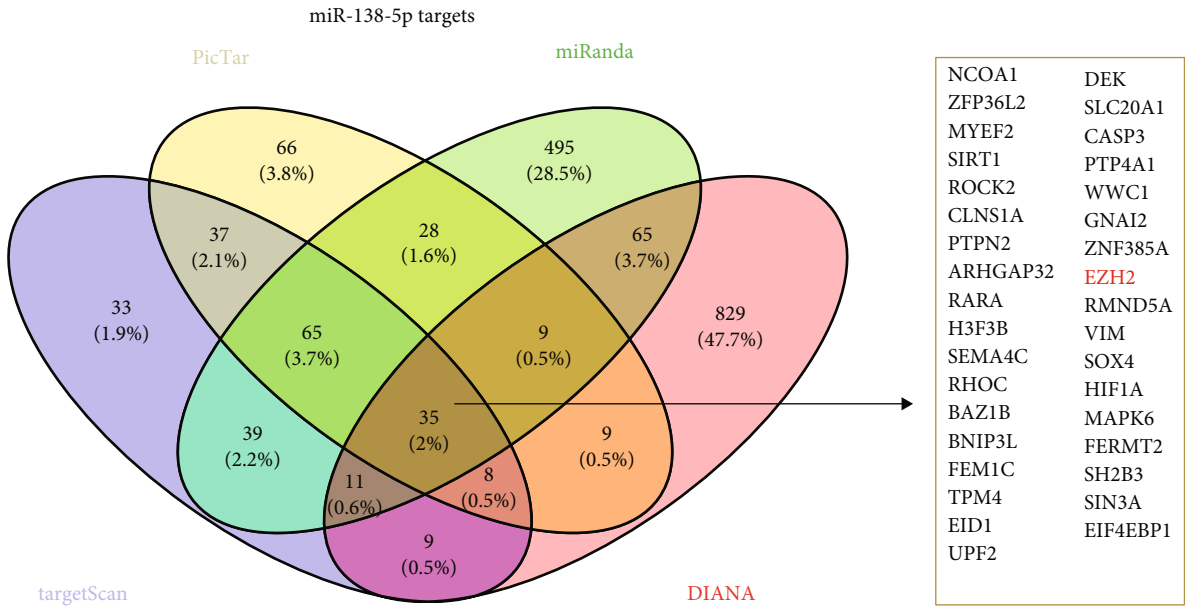

(a)

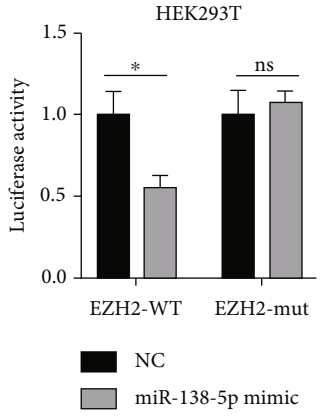

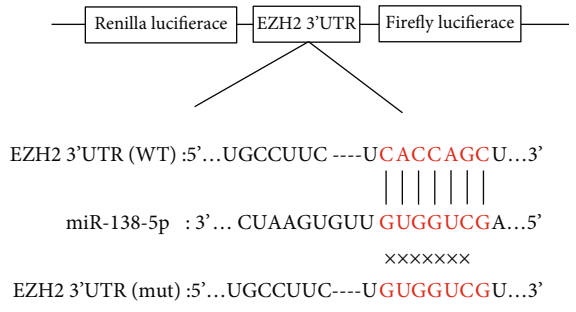

(b)

Figure 2: Continued.

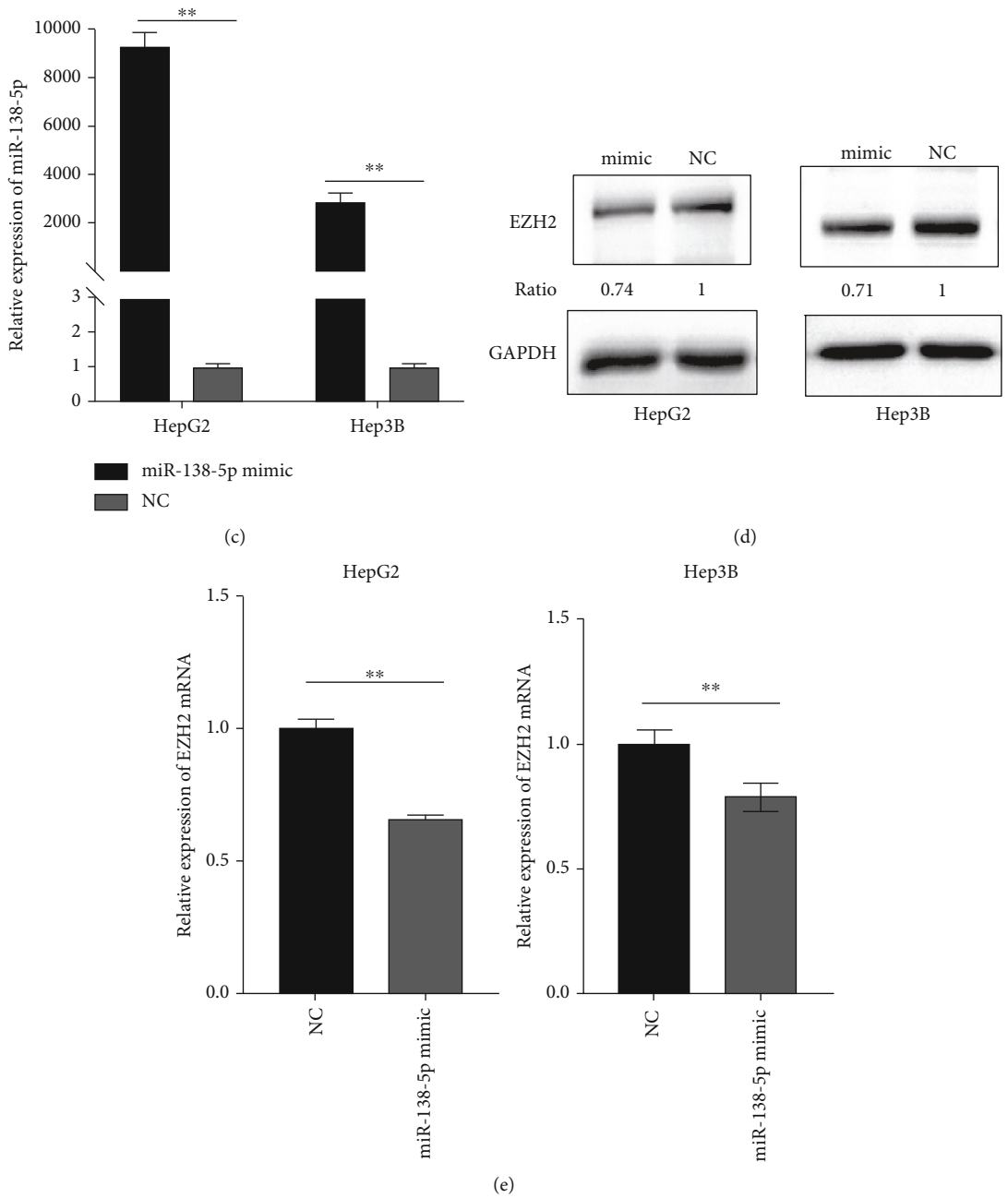

Figure 2: EZH2 is a direct target of miR-138-5p. (a) Venn diagram indicating the intersection of the number of target genes among the above four databases. (b) HEK293T cells were co-transfected with EZH2 3′UTR-wt or EZH2 3′UTR-mut with miR-138-5p mimics or NC. Following 48 h of transfection, luciferase activity was measured. (c) HepG2 and Hep3B were transfected with miR-138-5p mimic or NC for 24 h. The expression of miR-138-5p was determined by RT-qPCR analysis. The expression of U6 was used as an internal control. (d–e) HepG2 and Hep3B were transfected with miR-138-5p mimic or NC for 48 h. The expression of EZH2 was determined by Western blotting and RT-qPCR analysis. GAPDH was used as a loading control. $^{*}p < 0.05$; $^{**}p < 0.01$ (compared to NC group or vector group); ns, no significance.

normal tissues, suggesting that EZH2 may be related to the progression of HCC (Figure 1(b)). Then, the Kaplan Meier (KM) plotter online tool was used to establish the relationship between EZH2 expression and the survival outcomes of HCC [25], which revealed that HCC patients with a higher level of EZH2 had a poorer prognosis (OS: HR = 2.23, 95%CI = 1.56 to 3.19, $p < 0.001$) (Figure 1(c)).

To explore whether miR-138-5p is associated with EZH2 overexpression in HCC patients, we analyzed the level of has-miR-138-1, one member of the pre-miR-138-5p family, in the TCGA database. Interestingly, has-miR-138-1 was significantly downregulated in HCC specimens compared to normal tissues (Figure 1(d)). Has-miR-138-1 was pronouncedly lower expressed in patients with the grade 1 and

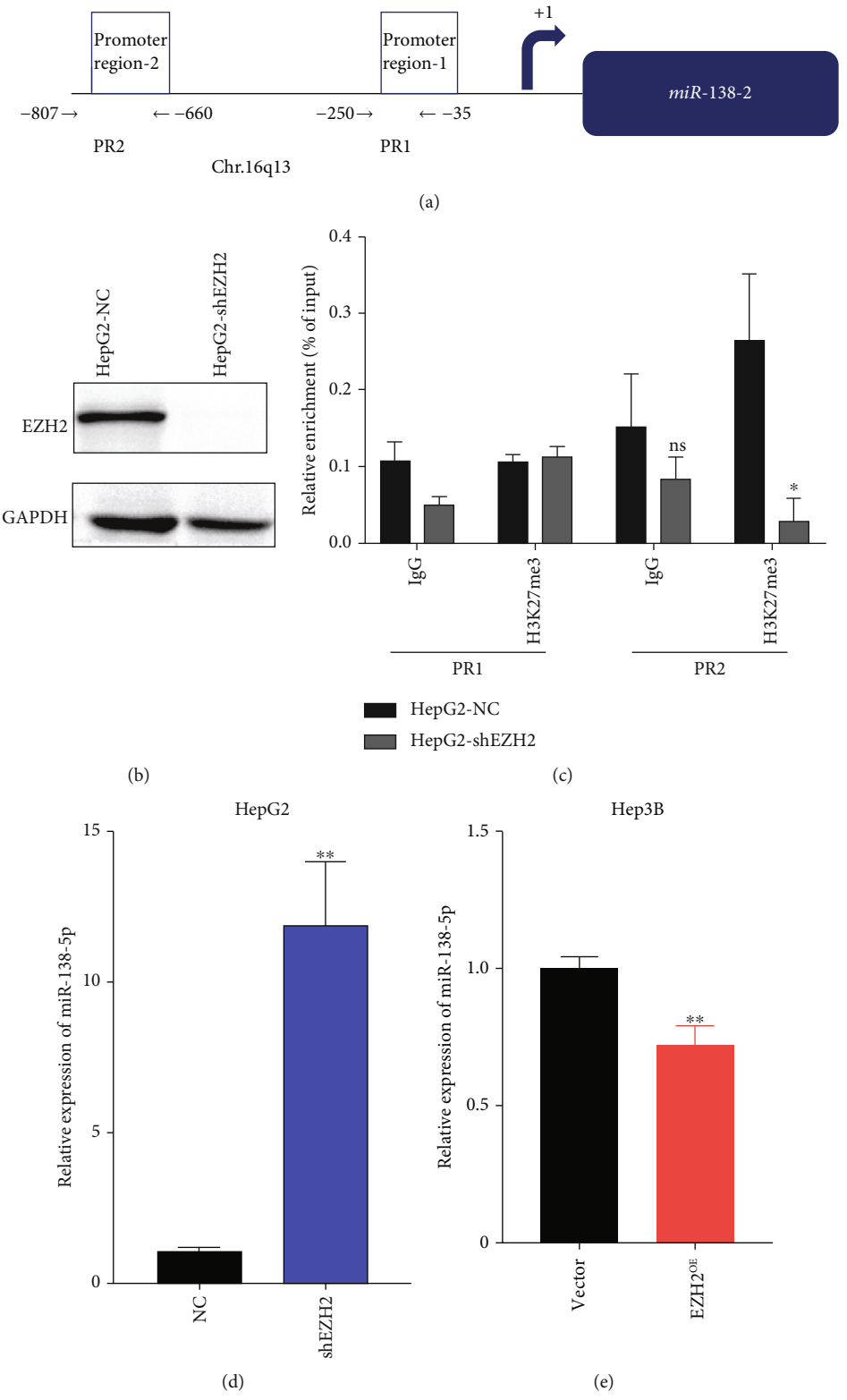

Figure 3: miR-138-5p is epigenetically regulated by EZH2. (a) Binding sites of primers used for the analysis of chromatin immunoprecipitation (ChIP) are indicated relative to the transcription start site. (b) Expression of EZH2 in HepG2-shEZH2 and HepG2-NC groups. (c) The HepG2-NC and HepG2-shEZH2 were cultured and subjected to ChIP using H3K27me3 antibodies, or as control, normal human IgG. The precipitated chromatin was analyzed by RT-qPCR for the abundance of region PP1&PP2 upstream of the miR-138-5p gene. Values were normalized to chromatin levels in 1% input samples. (d) Total RNA of HepG2-shEZH2 was isolated from cells and the miR-138 level was quantified by RT-qPCR (E) Hep3B was treated with EZH2 overexpression plasmid and total RNA was isolated from cells. The miR-138-5p level was quantified by RT-qPCR. $^{*}p < 0.05$; $^{**}p < 0.01$ (compared to NC group or vector group).

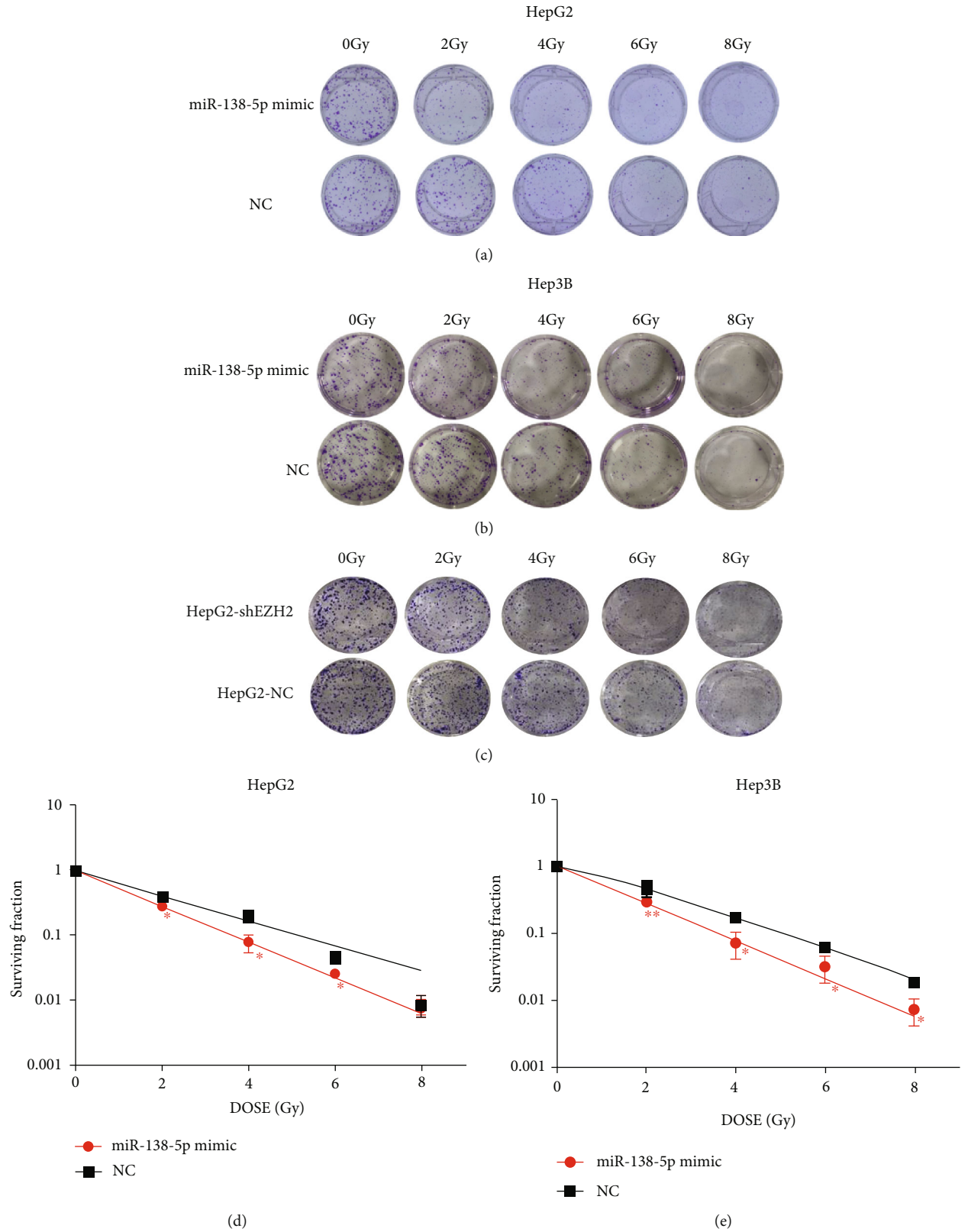

Figure 4: Continued.

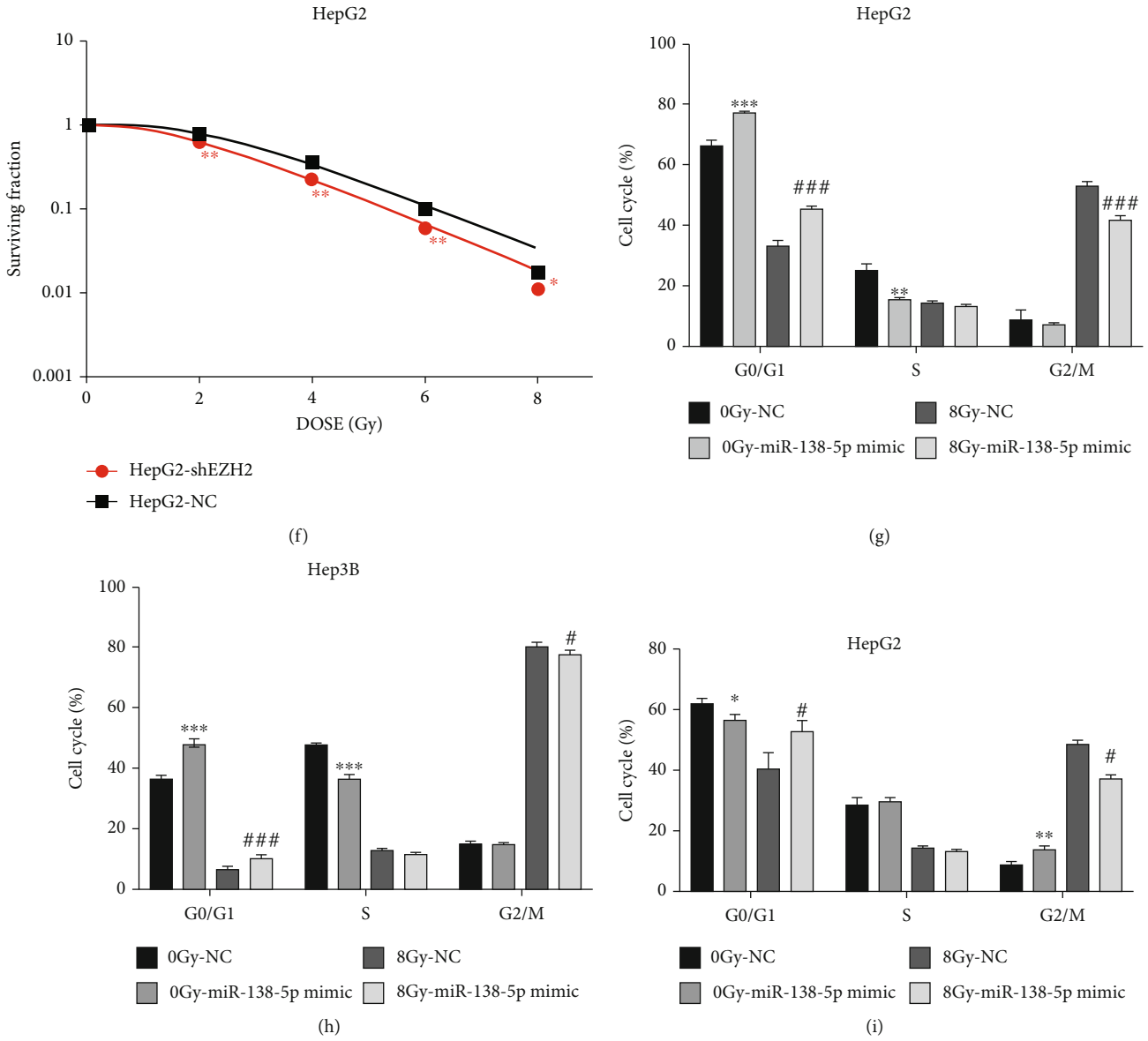

Figure 4: Continued.

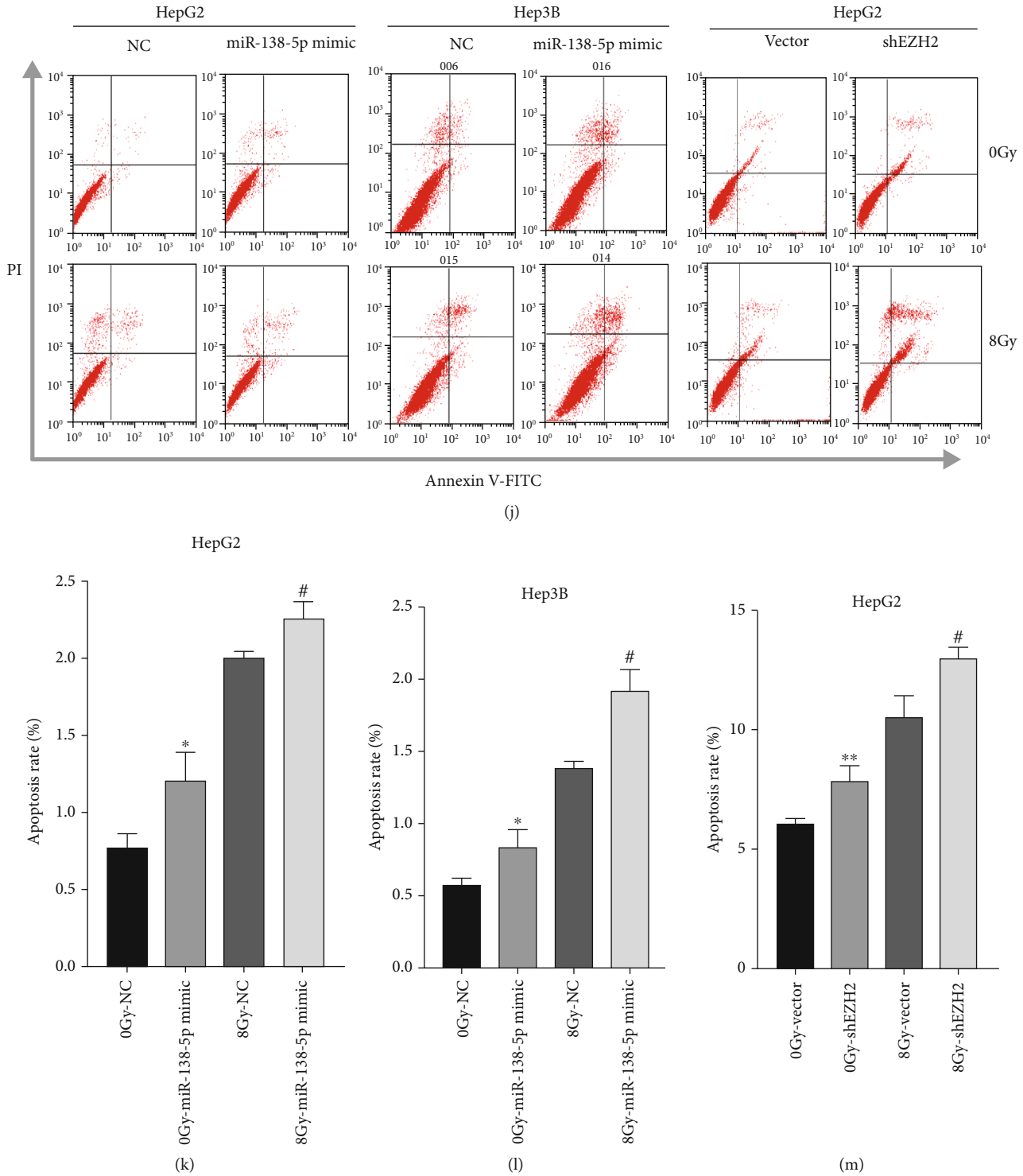

Figure 4: Overexpression of miR-138-5p by mimic or knockdown of EZH2 enhances radiosensitivity of HCC cells. (a–c) Experiments results of three groups of cells' clone formation experiments. (d–f) The SF of three groups of cells. (g–i) HepG2 and Hep3B cells were transfected with miR-138-5p mimic/NC or shEZH2/vector plasmid before exposure to 8 Gy radiation. After 24 h, cells were harvested for cell-cycle analysis. (j–m) HepG2 and Hep3B cells were transfected with miR-138-5p mimic/NC or shEZH2/vector plasmid before exposure to 8 Gy radiation. After 24 h, cells were harvested for apoptosis analysis. $^{*}p < 0.05$; $^{**}p < 0.01$ (compared to NC or vector group in HepG2); $^{\#}p < 0.05$; $^{\#\#}p < 0.01$ (compared to NC group after exposed to 8Gy).

grade 4 HCC, but not grade 2 and grade 3 HCC (Figure 1(e)). Similarly, survival analysis showed that lower level of miR-138-5p is associated with a poorer prognosis (OS: HR = 0.53, 95%CI = 0.33 to 0.86, $p < 0.01$) (Figure 1(f)). To explore further the biological function of miR-138-5p and EZH2 in HCC cells, we examined their expression

Table 2: Cell survival curve fitting results.

Cell	Group	D_0 (Gy)	n	Dq (Gy)	SF_2	R^2
HepG2	miR-138-5p mimic	1.570	1.053	0.081	0.292	0.9998
	NC	2.259	1.001	0.002	0.403	0.9969
Hep3B	miR-138-5p mimic	1.416	1.233	0.297	0.291	0.9993
	NC	1.773	1.614	0.849	0.466	0.9985
HepG2	miR-138-5p mimic	1.591	2.957	1.725	0.626	0.9997
	NC	1.644	4.471	2.463	0.785	0.9991

pattern in HCC cell lines, using the human liver cell line as a control. Consistent with the bioinformatics analysis, the expression levels of EZH2 protein and mRNA in five HCC cell lines, including HepG2 and Hep3B, were significantly higher than that in the immortalized human liver L-02 cell line (Figures 1(g) and 1(h)). Conversely, the level of miR-138-5p is lower in HCC cells than that in L-02 cells (Figure 1(i)).

3.2. In HCC Cells, EZH2 Is a Direct Target of miR-138-5p, which Is Epigenetically Regulated by EZH2 in H3K27me3-Dependent Way through a Negative Feedback Loop. To explore whether miR-138-5p are associated with EZH2 aberrant overexpression in HCC cells, we searched for the targets of miR-138-5p using a variety of target prediction algorithm databases, including PicTar, miRanda, TargetScan, and DIANA. After taking the overlapping target molecules, 35 genes, including EZH2, are found to be the common target genes of miR-138-5p (Figure 2(a)). Comprehensive bioinformatics analysis was carried out, which showed that miR-138-5p had a negative correlation with EZH2 expression level. The luciferase reporter assay also confirmed that EZH2 is a direct target of miR-138-5p (Figure 2(b)). HEK-293 T cells were also transfected with the mutant or wild-type EZH2-3′UTR luciferase reporter vectors together with miR-138-5p mimic or negative control, which showed that miR-138-5p overexpression significantly reduced wild-type EZH2-3′UTR reporter luciferase activity, but not that of the mutant-3′UTR reporter. This data indicated that miR-138 could directly target the EZH2 3′UTR. To further evaluate the inhibitory effect of miR-138-5p on EZH2, HepG2 and Hep3B cells were transfected with miR-138-5p mimic and mimic NC, and the overexpression of miR-138-5p was verified by RT-qPCR (Figure 2(c)). In HepG2 and Hep3B cells, the mRNA and protein expression of EZH2 were significantly inhibited by miR-138-5p overexpression (Figures 2(d) and 2(e)).

Next, we explored the molecular mechanism underlying miR-138-5p downregulation in HCC cells. We designed two primer pairs to amplify the two promoter regions of the miR-138 gene, i.e., promoter region 1(PR1, from −35 to −250 bp) and promoter region 2 (PR2, from −660 to −807 bp) upstream. Chromatin immunoprecipitation (ChIP) was performed to assess the repressive histone marker H3K27me3 (Figure 3(a)). To further study the regulatory role of EZH2 on miR-138-5p, the EZH2 gene was silenced with shRNA in HepG2 (Figure 3(b)). Furthermore, ChIP assays with H3K27me3 antibody showed that it was less occupied in the upstream regions of PR2 in HepG2-shEZH2 (Figure 3(c)). Thus, H3K27me3 upregulation induced by EZH2 may contribute to miR-138-5p suppression. These data confirmed that miR-138-5p was upregulated in HepG2-shEZH2 (Figure 3(d)). Conversely, cells overexpressing EZH2 showed a reduced level of miR-138-5p (Figure 3(e)). Taken together, these results indicate that miR-138-5p and EZH2 can form a negative feedback loop that regulates the phenotypes of HCC.

3.3. Overexpression of miR-138-5p or Knockdown of EZH2 Enhances Radiosensitivity of HCC Cells. To explore miR-138-5p's impact on HCC cells' radiosensitivity, clonogenic assays were performed after exposure to X-ray of different doses (0, 2, 4, 6 or 8 Gy). HepG2 and Hep3B cells in the logarithmic growth phase were divided into the miR-138-5p mimic group and NC group, each group with three repeated culture holes. Radiotherapy reduced the survival of the cells, as measured by survival fractions (SF), in both cell lines in a dose-dependent manner. However, cancer cells transfected with miR-138-5p mimic demonstrated a more significant decrease in SF compared to the NC group in all ranges of absorbed dose, and the cell survival curves decreased markedly (Figures 4(a)–4(d)). In the miR-138-5p mimic group, the radiation dose required to reduce the fraction of surviving cells to 37% of its previous value (D0 in radiation biology). The D0 dose for HepG2 cells decreased from 2.26 to 1.57 Gy and decreased from 1.77 to 1.42 Gy in Hep3B cells. Knocking down the EZH2 gene also achieved similar effects, i.e., the D0 dose for HepG2-shEZH2 decreased from 1.64 to 1.59 Gy (Table 2). These data suggest that the overexpression of miR-138-5p may significantly enhance the radiosensitivity of HCC cells. Various anticancer drugs are known to inhibit tumor cell division and induce cell death through cell cycle arrest, which prompted us to investigate whether the role of EZH2/miR-138-5p axis in enhancing radiosensitivity is facilitated by induced cell cycle arrest. After treating HCC cells with miR-138-5p mimic for 48 h, both HepG2 and Hep3B cells showed cell cycle arrest at the G0/G1 stage (Figures 4(g) and 4(h)). Compared to the NC group, the population of cells at the G0/G1 stage increased by 10.79% ± 1.07% in HepG2 cells and 4.17% ± 1.15% in Hep3B cells, respectively. In particular, the G0/G1 cycle arrest further increased in HepG2 after radiation treatment. Similarly, the HepG2-shEZH2 group also showed significantly increased G0/G1 arrest after radiation treatment (Figure 4(i)).

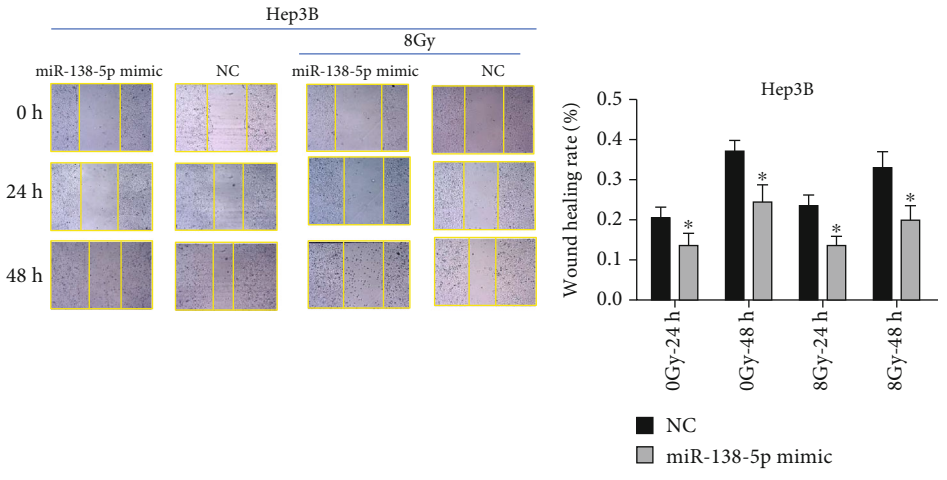

(a)

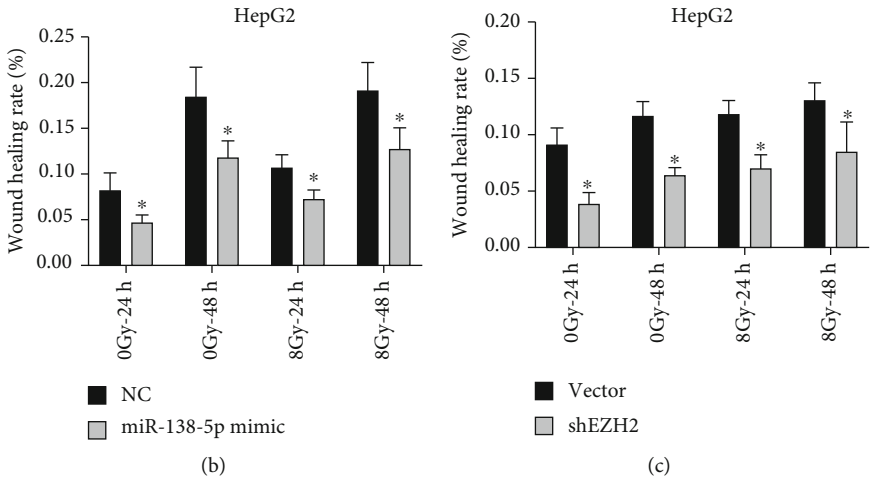

(b) (c)

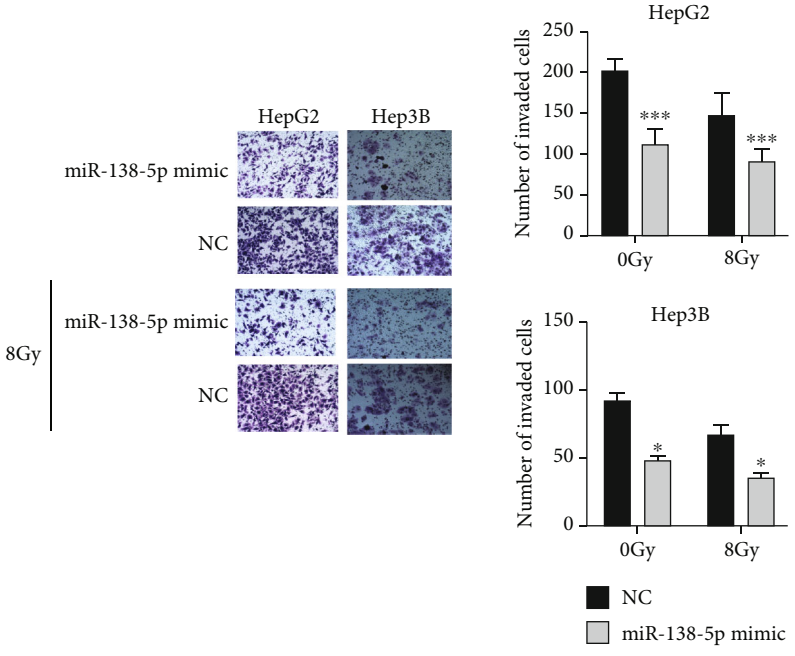

(d)

Figure 5: Continued.

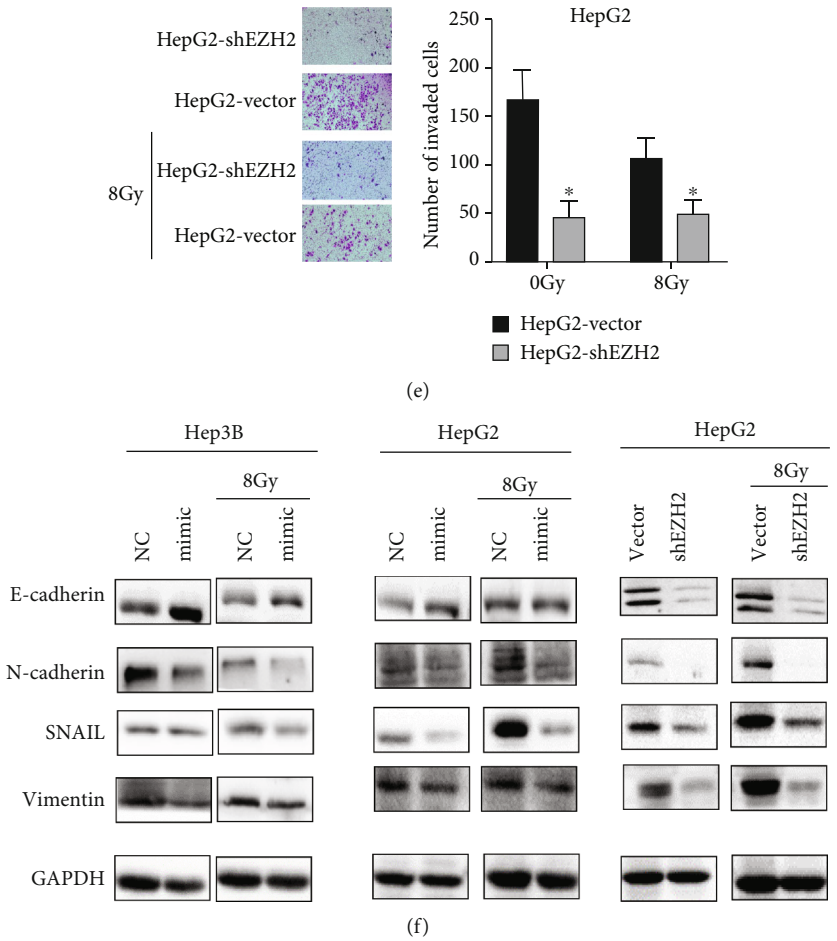

Figure 5: Overexpression of miR-138-5p or knockdown of EZH2 inhibits radiation-induced migration and invasion via EMT. (a–c) Wound healing assays of Hep3B and HepG2 cells infected with miR-138-5p mimic/NC or shEZH2/vector plasmid after radiation. (d–e) Transwell assays of Hep3B and HepG2 cells infected with miR-138-5p mimic/NC or shEZH2/vector plasmid after radiation. (f) The effect of miR-138-5p mimic or knockdown of EZH2 on the expression of EMT-related molecules by Western blotting. $^*p < 0.05$ (compared to NC group or the vector group).

Radiation-induced apoptosis is one of the major mechanisms of cell death. Hence, we also analyzed how dysregulation of EZH2/miR-138-5p axis contributed to the apoptosis of HCC cells (Figure 4(j)). Compared to the NC group, treatment with miR-138-5p mimic significantly increased the number of AnnexinV-FITC positive cells in HepG2 and Hep3B cells after radiation (Figures 4(k) and 4(l)). Consistently, the apoptosis rate of the HepG2-shEZH2 group was higher than that of the HepG2-vector group after radiation (Figure 4(m)).

3.4. Overexpression of miR-138-5p or Knockdown of EZH2 Inhibits Radiation-Induced Cell Migration and Invasion via Suppressing EMT. Given that radiation paradoxically promotes tumor cell migration and invasion while exerting cytotoxic effects, we explored whether the EZH2/miR-138-5p axis plays an important part in inhibiting cell migration and invasion while augmenting cellular radiosensitivity. In the mimic group, the relative wound healing rate was significantly reduced compared with the NC groups (Figures 5(a) and 5(b)). The high expression of miR-138-5p was also shown to inhibit the migration ability after being exposed to 8Gy radiation. The migratory ability of the HepG2-shEZH2 group was similar to that of the mimic group (Figure 5(c)). Knockdown of EZH2 also inhibited the migratory ability of HepG2 after radiation. As shown in Figures 5(d) and 5(e), overexpression of miR-138-5p or inhibition of EZH2 expression significantly decreased the migration and the invasion rate in HCC cells after radiation.

Since EMT is a putative molecular mechanism that drives tumor migration and invasion, we explored whether the EZH2/miR-138-5p axis is involved in EMT by analyzing levels of EMT markers including E-cadherin, N-cadherin, vimentin, and Snail. Our results indeed showed that the protein level of E-cadherin was significantly increased, which means adherens junction between cells was decreased. The protein levels of N-cadherin and vimentin were pronouncedly reduced in HepG2 and Hep3B cells after mimic or shEZH2 treatment, even after radiation, suggesting attenuated EMT (Figure 5(f)). Snail, a transcription factor that activates EMT, is also decreased after overexpressing miR-138-5p or inhibiting EZH2. Taken together, these results

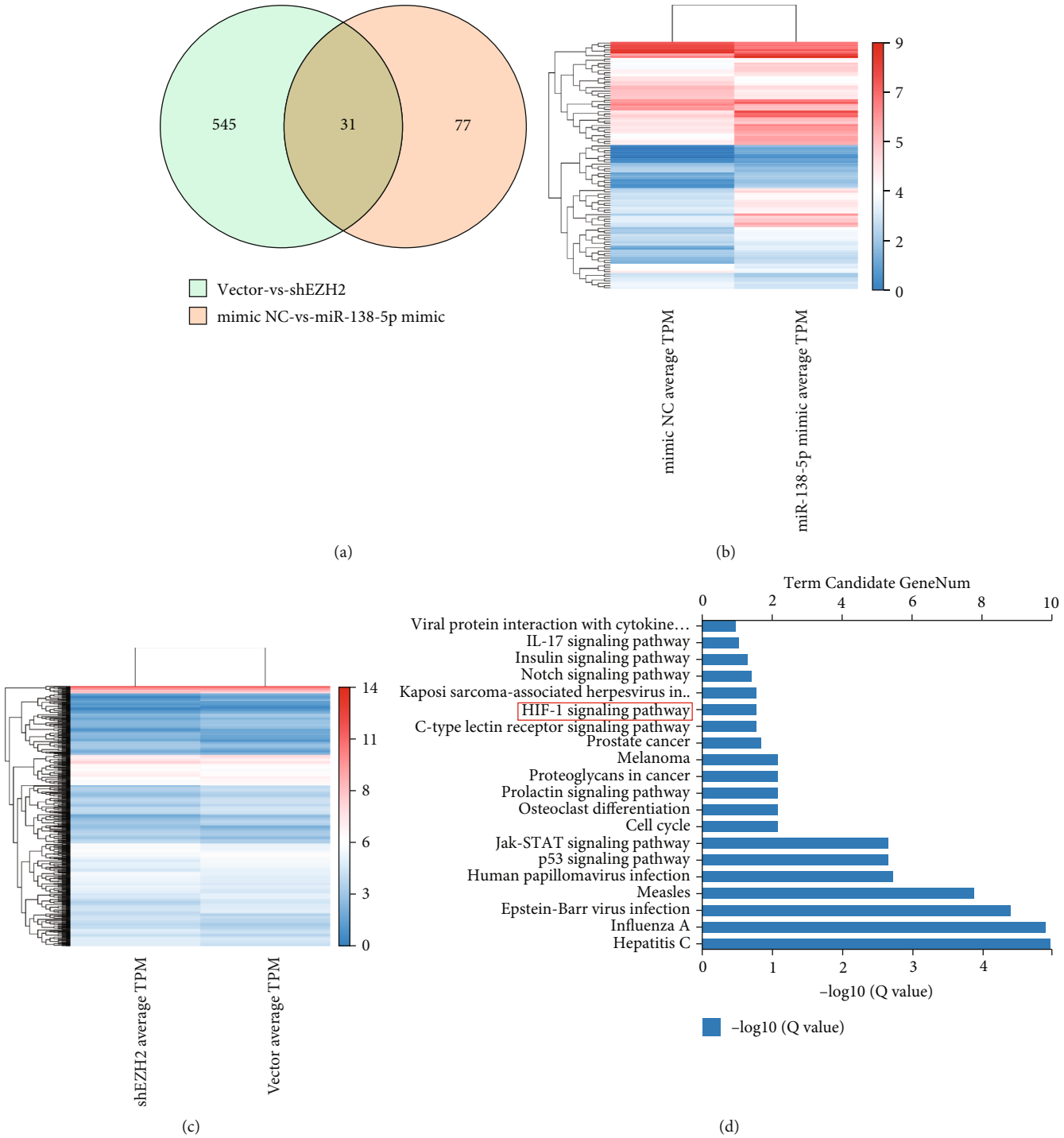

Figure 6: Continued.

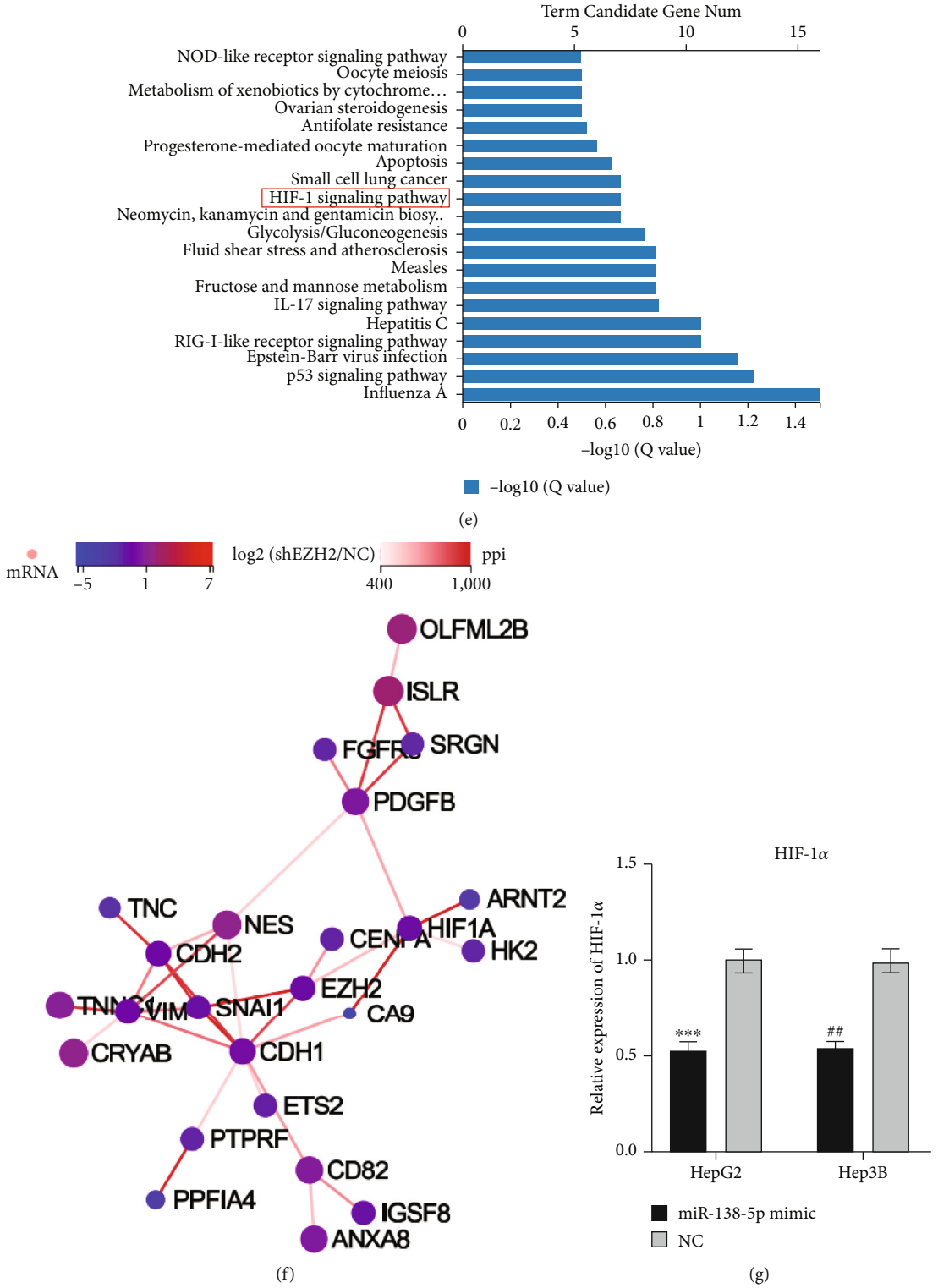

Figure 6: RNA-seq and verification. (a) Venn diagram showing the overlap of differentially expressed genes in two pair-wise comparisons (miR-138-5p mimic VS NC and HepG2-shEZH2 VS vector). (b–c) Heat maps of representative up and downregulated genes from HepG2 RNA-seq results. (d–e) The significant pathways enriched from the critical differential genes in KEGG analysis. (f) Network interaction diagram of representative and downregulated genes, EZH2, EMT, and HIF-1α-related genes from RNA-seq results. (g) In HepG2 and Hep3B cells, the expression detection of HIF-1α mRNA after transfection of miR-138-5p mimic by RT-qPCR.

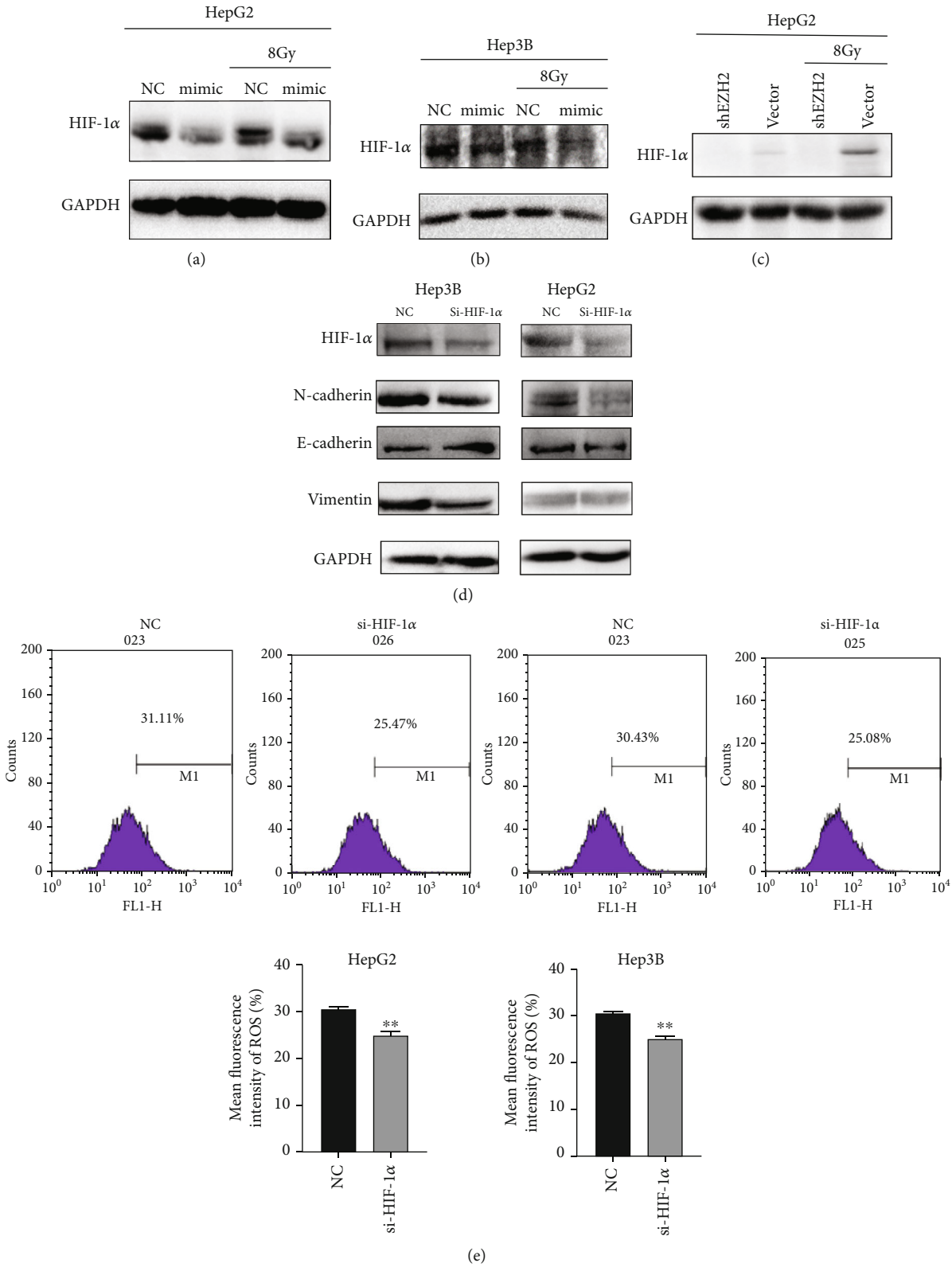

Figure 7: Continued.

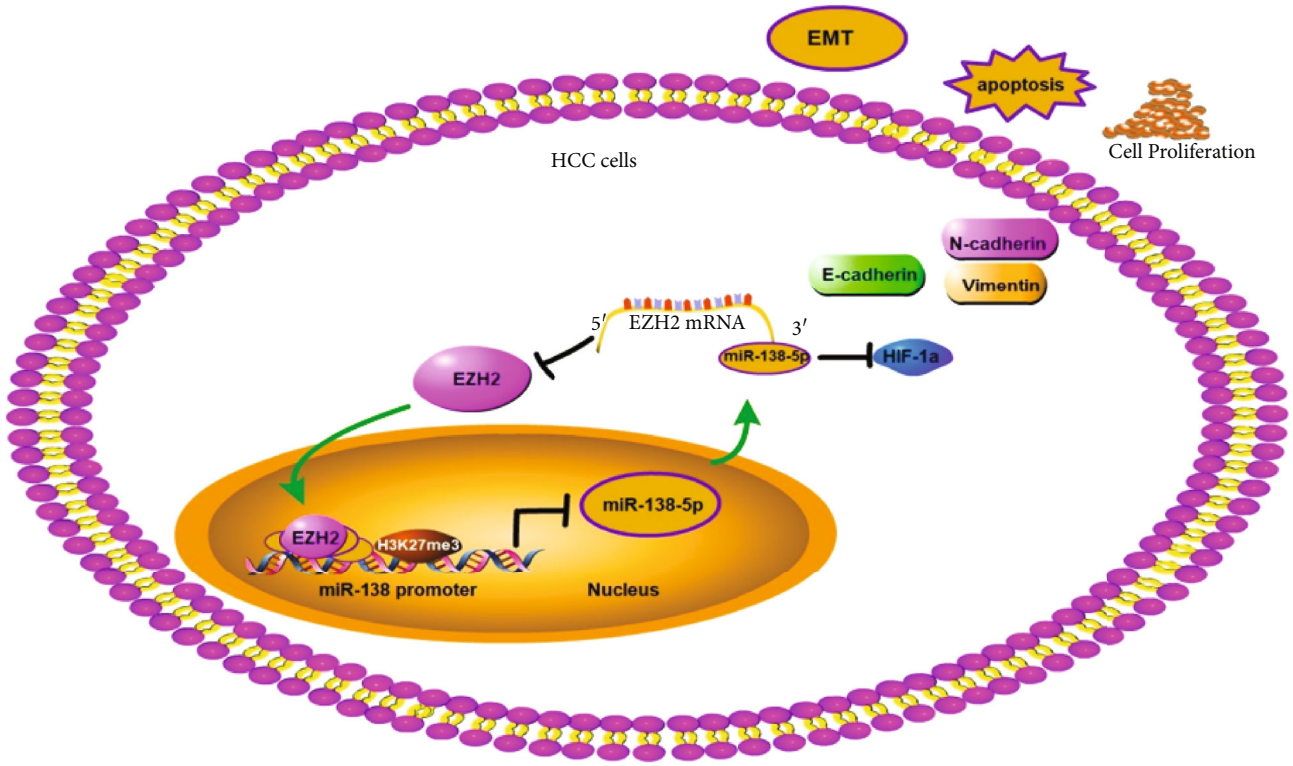

(f)

Figure 7: Dysregulation of EZH2/miR-138-5p axis affects EMT via HIF-1α. (a–c) In HepG2 and Hep3B cells, HIF-1α levels after transfection of miR-138-5p mimic were analyzed by Western Blot after radiation. (d) The effect of HIF-1α knockdown on the expression of EMT-related molecules by Western blotting (compared to NC group or vector group). (e) The level of ROS in HepG2 and Hep3B cells after transfection of siRNA of HIF-1α. (f) Proposed model for EZH2/miR-138 regulatory axis involved in EMT of HCC cells. $^{*}p < 0.05$; $^{**}p < 0.01$ compared to NC group.

implicated that dysregulation of EZH2/miR-138-5p axis can suppress EMT in HepG2 and Hep3B cells.

3.5. Dysregulation of EZH2/miR-138-5p Axis Affects the Expression of HIF-1α. HepG2 cells were treated with miR-138-5p mimic/NC or shEZH2/vector plasmid and then analyzed by RNA-Seq. The Venn diagram and heat map revealed 576 differential genes between HepG2-shEZH2/HepG2-vector groups (281 downregulated genes and 295 upregulated genes) and 108 differential genes between miR-138-5p mimic/NC groups (33 downregulated genes and 75 upregulated genes) (Figures 6(a)–6(c)). As determined by KEGG analysis, differential genes in both groups were enriched in the HIF-1 signaling pathway (Figures 6(d)–6(e)). Then, we plotted a network interaction diagram with EZH2 and HIF-1α as the main candidate genes, showing a potential regulatory relationship between EZH2 and HIF-1α (Figure 6(f)). We confirmed the expression of HIF-1α via RT-qPCR analyses. The HIF-1α expression in HepG2 and Hep3B cells was downregulated upon miR-138-5p mimic treatment (Figure 6(g)).

3.6. Dysregulation of EZH2/miR-138-5p Axis Affects EMT via HIF-1α. Hypoxia is an environmental feature at the aggressive front of tumors, where EMT program takes place. Hypoxia-activated HIF-1α induces cancer EMT through multiple molecules and pathways, including epigenetic regulators and transcription factors/repressors [26]. To identify whether HIF-1 is involved in the regulation of EMT by this axis, we further analyzed the expression of HIF-1α in each group. Our results showed that protein level of HIF-1α was decreased after overexpressing miR-138-5p or inhibiting EZH2 after cells were exposed to 8 Gy radiation (Figures 7(a)–7(c)). The expression of HIF-1α was then reduced using siRNA in HepG2 and Hep3B cells. We found that the epithelial marker E-cadherin was upregulated, whereas the mesenchymal markers N-cadherin and Vimentin were downregulated (Figure 7(d)). Flow cytometry analysis also detected the change of intracellular ROS content after inhibiting HIF-1α expression. These data suggest that inhibition of HIF-1α expression can suppress the level of ROS (Figure 7(e)).

4. Discussion

This study investigated the role of the EZH2/miR-138-5p regulatory feedback loop in the post-radiation response of HCC. Multiple studies have shown a correlation between high EZH2 expression and poor prognosis in different cancers, including HCC [5, 27]. It has also been reported that EZH2 can protect glioma stem cells from radiation-induced cell death [28]. The high expression of EZH2 may be one of the mechanisms of bladder cancer cells in

acquiring radiation resistance [29]. However, the role of EZH2 in the response of HCC cells to radiation is unclear. Here, we show that inhibition of EZH2 expression can restore the radiosensitivity of HCC cells. It is worth noting that several studies have reported upregulation of EZH2 expression in HCC, of which the underlying mechanism remains unknown. Also, since changes in miRNA expression appear to be a common feature of cancers, including HCC, inhibition of miRNAs targeting EZH2 may be associated with aberrant overexpression of EZH2. We here provided clear evidence that miR-138-5p negatively regulates EZH2 expression in HCC. Compared with tumor adjacent tissue, miR-138 was downregulated in HCC patient samples and negatively correlated with HCC survival. The negative correlation between miR-138 and EZH2 expression levels in HCC patients could be explained by the fact that EZH2 is a direct target of miR-138, as revealed by the luciferase assay. Similar to our findings, miRNA-associated EZH2 overexpression has also been reported in other tumors [30, 31].

Growing evidence suggests that EZH2 can also negatively regulate miRNAs through a feedback loop in tumors [32, 33]. In HCC, it has been reported that histone methylation can silence some tumor suppressor miRNAs and, in turn, lead to the upregulation of some oncogenes [34, 35]. Our data supported such a notion as miR-138 was shown to be epigenetically regulated by transcriptional suppression of its promoter region in HCC cells. Inhibition of EZH2 reduced H3K27me3 marker enrichment in the promoter region of miR-138-5p. These findings suggest a regulatory loop between the epigenetic silencing mechanism of miR-138-5p and EZH2 in HCC cells.

To verify the clinical relevance of EZH2 and the prognosis of HCC patients, we analyzed the TCGA database and found that patients with high EZH2 expression had significantly poorer survival. With increasing HCC grade, the expression of EZH2 was significantly increased. These data suggest that EZH2 upregulation is a predictor of poor prognosis. Therefore, anti-EZH2 therapy may serve as a promising strategy for the treatment of HCC. In view of the expression levels of EZH2 and miR-138-5p in liver cancer patients, we verified the changes in the radiosensitivity of HCC cells after changing the expression levels.

In addition, one of the most important findings of this paper is that overexpression of miR-138-5p in HCC cells can effectively enhance the radiosensitivity and reduce the ability of proliferation and apoptosis of HCC cells after radiation, and silencing of the EZH2 gene can achieve similar effects. These data suggest that low expression of miR-138-5p has an impact on HCC cell radiosensitivity by forming a negative feedback loop with EZH2, which is a direct and functionally relevant target of miR-138-5p. Similar to miR-138-5p overexpression, EZH2 inhibition by EZH2 shRNA induced apoptosis and cell cycle arrest at the G0/G1 stage.

This observation may suggest that a high level of EZH2 in HCC cells leads to an imbalance of cellular feedback loops leading to dysregulation of miR-138-5p, which affects cellular radiosensitivity. This feedback loop in the cell has been in a certain steady state, and its dynamic behavior may be influenced by external stimuli. After receiving an external stimulus, the feedback system can switch from one stable state to another in order to adapt to the external stimulus. Our results also suggest that overexpression of miR-138-5p or inhibition of EZH2 inhibits the migratory and invasive ability of HCC cells after radiation, at least in part through inhibition of the EMT pathway.

Our RNA-seq study found that the expression of HIF-1α was downregulated in miR-138-5p mimic group compared to the NC group, which is also downregulated in HepG2-shEZH2 in comparison to HepG2-vector. We also confirmed that HIF-1α was significantly downregulated in HepG2, in which miR-138-5p is overexpressed or EZH2 is silenced. Notably, in some cells, miR-138-5p can directly target HIF-1α and inhibit its expression [36, 37]. Studies have also reported that EZH2 can affect the expression of HIF-1α by downregulated miR-146a-5p [38]. These results suggest that dysregulation of EZH2/miR-138-5p axis could downregulate HIF-1α in direct or indirect pathway. Although the molecular mechanism mentioned above needs to be further elucidated, the above studies including our results further confirmed that HIF-1α is an important downstream target gene of EZH2/miR-138-5p axis. In a normal oxygen environment, HIF-1α is at a completely inactive level. Conversely, when cells are hypoxic, elevated HIF enters the nucleus and then upregulates many genes involved in cancer progression. High level of HIF-1α promotes cancer progression through multiple mechanisms, including angiogenesis, cell proliferation and survival, invasion and metastasis, and therapy resistance. It was also reported that HIF-1α could promote metastasis and EMT through increasing ROS expression level in cancer cells [39]. It has also been reported that, in HCC cells, hypoxia leads to increase on ROS and HIF-1α levels, which promotes the progression of EMT through the Hedgehog pathway [40]. We further confirmed the above studies, and we found that ROS level were reduced and EMT progression was inhibited after using siRNA to knockdown HIF-1α.

5. Conclusions

In conclusion, we determined EZH2 and miR-138-5p reciprocally regulate each other in HCC cells via a negative feedback loop, which contributes to the change of HIF-1α expression (Figure 7(f)). Our findings provide new insights into the mechanism of miR-138-5p/EZH2/HIF-1α pathway in the radiosensitivity of HCC. This study establishes EZH2/miR-138-5p axis as a potential predictor of poor prognosis and therapeutic target for HCC patients.

Data Availability

The data are presented within the paper. Additional raw data are available on request from the corresponding author.

Conflicts of Interest

The authors declare no conflict of interest.

Acknowledgments

This research was funded by the Key R & D project of Science and Technology Department of Jilin Province (No. 20210204109YY; No. 20200404179YY) and the National Natural Science Foundation of China (No. 82072184).

References

[1] H. Sung, J. Ferlay, R. L. Siegel et al., "Global cancer statistics 2020: GLOBOCAN estimates of incidence and mortality worldwide for 36 cancers in 185 countries," *CA: a Cancer Journal for Clinicians*, vol. 71, no. 3, pp. 209–249, 2021.

[2] M. Kudo, F. Trevisani, G. K. Abou-Alfa, and L. Rimassa, "Hepatocellular carcinoma: therapeutic guidelines and medical treatment," *Liver Cancer*, vol. 6, no. 1, pp. 16–26, 2016.

[3] J. M. Llovet and M. Beaugrand, "Hepatocellular carcinoma: present status and future prospects," *Journal of Hepatology*, vol. 38, Suppl 1, pp. 136–149, 2003.

[4] S. B. Gao, S. L. Sun, Q. L. Zheng et al., "Genetic alteration and misexpression of Polycomb group genes in hepatocellular carcinoma," *American Journal of Cancer Research*, vol. 5, no. 10, pp. 2969–2979, 2015.

[5] M. Y. Cai, Z. T. Tong, F. Zheng et al., "EZH2 protein: a promising immunomarker for the detection of hepatocellular carcinomas in liver needle biopsies," *Gut*, vol. 60, no. 7, pp. 967–976, 2011.

[6] T. Sudo, T. Utsunomiya, K. Mimori et al., "Clinicopathological significance of EZH2 mRNA expression in patients with hepatocellular carcinoma," *British Journal of Cancer*, vol. 92, no. 9, pp. 1754–1758, 2005.

[7] M. Sasaki, H. Ikeda, K. Itatsu et al., "The overexpression of polycomb group proteins Bmi1 and EZH2 is associated with the progression and aggressive biological behavior of hepatocellular carcinoma," *Laboratory Investigation*, vol. 88, no. 8, pp. 873–882, 2008.

[8] A. S. Cheng, S. S. Lau, Y. Chen et al., "EZH2-mediated concordant repression of Wnt antagonists promotes β-catenin-dependent hepatocarcinogenesis," *Cancer Research*, vol. 71, no. 11, pp. 4028–4039, 2011.

[9] B. Huang, M. Huang, and Q. Li, "MiR-137 suppresses migration and invasion by targeting EZH2-STAT3 signaling in human hepatocellular carcinoma," *Pathology, Research and Practice*, vol. 214, no. 12, pp. 1980–1986, 2018.

[10] Y. Shi, X. Yang, X. Xue et al., "HANR promotes hepatocellular carcinoma progression via miR-214/EZH2/TGF-β axis," *Biochemical and Biophysical Research Communications*, vol. 506, no. 1, pp. 189–193, 2018.

[11] S. T. Lee, Z. Li, Z. Wu et al., "Context-specific regulation of NF-κB target gene expression by EZH2 in breast cancers," *Molecular Cell*, vol. 43, no. 5, pp. 798–810, 2011.

[12] K. Xu, Z. J. Wu, A. C. Groner et al., "EZH2 oncogenic activity in castration-resistant prostate cancer cells is poly-comb-independent," *Science*, vol. 338, no. 6113, pp. 1465–1469, 2012.

[13] Z. Li, P. Hou, D. Fan et al., "The degradation of EZH2 mediated by lncRNA ANCR attenuated the invasion and metastasis of breast cancer," *Cell Death and Differentiation*, vol. 24, no. 1, pp. 59–71, 2017.

[14] Z. Cao, W. Wu, H. Wei, W. Zhang, Y. Huang, and Z. Dong, "Downregulation of histone-lysine N-methyltransferase EZH2 inhibits cell viability and enhances chemosensitivity in lung cancer cells," *Oncology Letters*, vol. 21, no. 1, p. 26, 2021.

[15] T. Zeng, L. Luo, Y. Huang, X. Ye, and J. Lin, "Upregulation of miR-138 increases sensitivity to cisplatin in hepatocellular carcinoma by regulating EZH2," *BioMed Research International*, vol. 2021, Article ID 6665918, 12 pages, 2021.

[16] D. Y. Zhang, Q. C. Sun, X. J. Zou et al., "Long noncoding RNA UPK1A-AS1 indicates poor prognosis of hepatocellular carcinoma and promotes cell proliferation through inter-action with EZH2," *Journal of Experimental & Clinical Cancer Research*, vol. 39, no. 1, p. 229, 2020.

[17] A. L. Harris, "Hypoxia–a key regulatory factor in tumour growth," *Nature Reviews. Cancer*, vol. 2, no. 1, pp. 38–47, 2002.

[18] E. K. Rofstad, K. Sundfør, H. Lyng, and C. G. Tropé, "Hypoxia-induced treatment failure in advanced squamous cell carcinoma of the uterine cervix is primarily due to hypoxia-induced radiation resistance rather than hypoxia-induced metastasis," *British Journal of Cancer*, vol. 83, no. 3, pp. 354–359, 2000.

[19] J. Chen, J. Chen, J. Huang et al., "HIF-2α upregulation mediated by hypoxia promotes NAFLD-HCC progression by activating lipid synthesis via the PI3K-AKT-mTOR pathway," *Aging (Albany NY)*, vol. 11, no. 23, pp. 10839–10860, 2019.

[20] E. Moreno Roig, A. J. Groot, A. Yaromina et al., "HIF-1α and HIF-2α differently regulate the radiation sensitivity of NSCLC cells," *Cells*, vol. 8, no. 1, 2019.

[21] T. W. Meijer, J. H. Kaanders, P. N. Span, and J. Bussink, "Targeting hypoxia, HIF-1, and tumor glucose metabolism to improve radiotherapy efficacy," *Clinical Cancer Research*, vol. 18, no. 20, pp. 5585–5594, 2012.

[22] W. Yang, T. Sun, J. Cao, and S. Fan, "Hypoxia-inducible factor-1α downregulation by small interfering RNA inhibits proliferation, induces apoptosis, and enhances radiosensitivity in chemical hypoxic human hepatoma SMMC-7721 cells," *Cancer Biotherapy & Radiopharmaceuticals*, vol. 26, no. 5, pp. 565–571, 2011.

[23] D. S. Chandrashekar, B. Bashel, S. A. H. Balasubramanya et al., "UALCAN: a portal for facilitating tumor subgroup gene expression and survival analyses," *Neoplasia*, vol. 19, no. 8, pp. 649–658, 2017.

[24] B. Győrffy, "Survival analysis across the entire transcriptome identifies biomarkers with the highest prognostic power in breast cancer," *Computational and Structural Biotechnology Journal*, vol. 19, pp. 4101–4109, 2021.

[25] A. Lánczky and B. Győrffy, "Web-based survival analysis tool tailored for medical research (KMplot): development and implementation," *Journal of Medical Internet Research*, vol. 23, no. 7, article e27633, 2021.

[26] B. Bao, A. S. Azmi, S. Ali et al., "The biological kinship of hypoxia with CSC and EMT and their relationship with deregulated expression of miRNAs and tumor aggressiveness," *Biochimica et Biophysica Acta*, vol. 1826, no. 2, pp. 272–296, 2012.

[27] M. L. Eich, M. Athar, J. E. Ferguson, and S. Varambally, "EZH2-targeted therapies in cancer: hype or a reality," *Cancer Research*, vol. 80, no. 24, pp. 5449–5458, 2020.

[28] S. H. Kim, K. Joshi, R. Ezhilarasan et al., "EZH2 protects glioma stem cells from radiation-induced cell death in a MELK/FOXM1-dependent manner," *Stem Cell Reports*, vol. 4, no. 2, pp. 226–238, 2015.

[29] X. Zhang, X. Ma, Q. Wang, and Z. Kong, "EZH2 targeting to improve the sensitivity of acquired radio-resistance bladder

cancer cells," *Translational Oncology*, vol. 16, article 101316, 2022.

[30] Y. Li, H. C. Zhou, Y. Zhang, and H. Huang, "MicroRNA-625-3p inhibits gastric cancer metastasis through modulating EZH2," *European Review for Medical and Pharmacological Sciences*, vol. 24, no. 3, pp. 1177–1185, 2020.

[31] X. B. Sun, Y. W. Chen, Q. S. Yao et al., "Mi-croRNA-144 suppresses prostate cancer growth and metastasis by targeting EZH2," *Technology in Cancer Research & Treatment*, vol. 20, p. 153303382198981, 2021.

[32] L. Wang, X. Zhang, L. T. Jia et al., "C-Myc-mediated epigenetic silencing of MicroRNA-101 contributes to dysregulation of multiple pathways in hepatocellular carcinoma," *Hepatology*, vol. 59, no. 5, pp. 1850–1863, 2014.

[33] C. Zhuang, P. Wang, D. Huang et al., "A double-negative feedback loop between EZH2 and miR-26a regulates tumor cell growth in hepatocellular carcinoma," *International Journal of Oncology*, vol. 48, no. 3, pp. 1195–1204, 2016.

[34] J. Hou, L. Lin, W. Zhou et al., "Identification of miRNomes in human liver and hepatocellular carcinoma reveals miR-199a/b-3p as therapeutic target for hepatocellular carcinoma," *Cancer Cell*, vol. 19, no. 2, pp. 232–243, 2011.

[35] X. Zhang, X. Zhang, T. Wang et al., "MicroRNA-26a is a key regulon that inhibits progression and metastasis of c-Myc/EZH2 double high advanced hepatocellular carcinoma," *Cancer Letters*, vol. 426, pp. 98–108, 2018.

[36] Y. S. Gai, Y. H. Ren, Y. Gao, and H. N. Liu, "Astaxanthin protecting myocardial cells from hypoxia/reoxygenation injury by regulating miR-138/HIF-1α axis," *European Review for Medical and Pharmacological Sciences*, vol. 24, no. 14, pp. 7722–7731, 2020.

[37] H. Mei, H. Xian, and J. Ke, "LncRNA-MCM3AP-AS1 promotes the progression of infantile hemangiomas by increasing miR-138-5p/HIF-1α axis-regulated glycolysis," *Frontiers in Molecular Biosciences*, vol. 8, article 753218, 2021.

[38] S. Ni, B. Yang, L. Xia, and H. Zhang, "EZH2 mediates miR-146a-5p/HIF-1α to alleviate inflammation and glycolysis after acute spinal cord injury," *Mediators of Inflammation*, vol. 2021, Article ID 5591582, 14 pages, 2021.

[39] W. N. Xu, R. Z. Yang, H. L. Zheng, L. S. Jiang, and S. D. Jiang, "NDUFA4L2 regulated by HIF-1α promotes metastasis and epithelial-mesenchymal transition of osteosarcoma cells through inhibiting ROS production," *Frontiers in Cell and Development Biology*, vol. 8, article 515051, 2020.

[40] Z. Liu, K. Tu, Y. Wang et al., "Hypoxia accelerates aggressiveness of hepatocellular carcinoma cells involving oxidative stress, epithelial-mesenchymal transition and non-canonical hedgehog signaling," *Cellular Physiology and Biochemistry*, vol. 44, no. 5, pp. 1856–1868, 2017.

Hindawi
Oxidative Medicine and Cellular Longevity
Volume 2022, Article ID 9174111, 13 pages
https://doi.org/10.1155/2022/9174111

Research Article

GATA3 Exerts Distinct Transcriptional Functions to Regulate Radiation Resistance in A549 and H1299 Cells

Rui Wang,[1] **Junxuan Yi**,[1] **Hui Gao**,[1,2] **Xinfeng Wei**,[1] **Lihong Shao**,[3] **Mingwei Wang**,[1] **Weiqiang Xu**,[1] **Xiaoshu Yin**,[1] **Yannan Shen**,[1] **Zhicheng Wang**,[1] **Wei Wei**,[1,4] **and Shunzi Jin**[1]

[1]*NHC Key Laboratory of Radiobiology, School of Public Health, Jilin University, Changchun, Jilin, China*
[2]*Department of Orthopedics, The First Hospital of Jilin University, Changchun, Jilin, China*
[3]*Department of Radiation Oncology, The First Bethune Hospital of Jilin University, China*
[4]*Affiliated Dongguan People's Hospital, Southern Medical University, Dongguan, Guangdong, China*

Correspondence should be addressed to Wei Wei; dr_weiwei528@163.com and Shunzi Jin; jinsz@jlu.edu.cn

Received 21 June 2022; Accepted 23 July 2022; Published 10 August 2022

Academic Editor: Bing Wang

Background. Radiation resistance of lung cancer cells is a vital factor affecting the curative effect of lung cancer. Transcription factor GATA3 is involved in cell proliferation, invasion, and migration and is significantly expressed in a variety of malignancies. However, the molecular mechanism governing GATA3 regulation in lung cancer cells' radiation resistance is unknown. *Methods*. Radiation-resistant cell models (A549-RR and H1299-RR) were made using fractionated high-dose irradiation. Use clone formation, CCK-8, F-actin staining, cell cycle detection, and other experiments to verify whether the model is successfully constructed. Cells were transiently transfected with knockdown or overexpression plasmid. To explore the relationship between GATA3/H3K4me3 and target genes, we used ChIP-qPCR, ChIP-seq, and dual luciferase reporter gene experiments. Xenograft tumor models were used to evaluate the effect of GATA3 depletion on the tumorigenic behavior of lung cancer cells. *Results*. We report that transcription factors GATA3 and H3K4me3 coactivate NRP1 gene transcription when A549 cells develop radiation resistance. However, the mechanism of radiation resistance in H1299 cells is that GATA3 acts as a transcription inhibitor. The decrease of GATA3 will promote the increase of NRP1 transcription, in which H3K4me3 does not play a leading role. *Conclusions*. GATA3, an upstream transcriptional regulator of NRP1 gene, regulates the radioresistance of A549 and H1299 cells by opposite mechanisms, which provides a new target for radiotherapy of lung cancer.

1. Introduction

Radiotherapy is one of the most effective cancer therapy approaches that involves complex biological processes to induce cancer cell death [1–3]. The factors that cause cancer patients to produce radiotherapy resistance during treatment are diverse. Molecular mechanisms of radioresistance remain unclear.

GATA binding protein-3 (GATA3) is a transcription factor consisting of 443 or 444 amino acids with two activation domains and two zinc finger structures [4, 5]. GATA3 affects target gene expression and triggers the proliferation and differentiation of specific immune cells [6, 7]. GATA3 is expressed in various tissues and cell types, especially breast, central nervous system, kidney, hair follicle skin, helper T cells (Th2), lymphocytes, and so on [8]. High GATA3 expression in lung adenocarcinoma has also been considered an evaluation factor of poor prognosis [4, 9–11]. However, its function remains elusive.

Neuropilin-1 (NRP1) is a transmembrane protein overexpressed in advanced human tumors, typically exhibiting growth-promoting functions in cancer cells [12, 13]. As a coreceptor for vascular endothelial growth factors (VEGFs), NRP1 has been shown to interact with the cell surface epidermal growth factor receptor (EGFR) to promote intracellular signaling. The mechanisms modulating *NRP1* expression in cancer cells are controversial. For example, growth factors

and stimulation of the RAS-MAPK signaling pathway may stimulate NRP1 transcription [14, 15]. On the other hand, *NRP1* transcripts are proposed targets for miRNA-338 [16] and other miRNAs. At present, research on NRP1 is involved in many fields such as angiogenesis, the hematopoietic system, immune system, and tumor occurrence and development [17, 18]. Previous studies have supported the notion that elevated *NRP1* expression in tumors correlates with poor outcomes. On the other hand, NRP1 is associated with radiation resistance [19]. However, the molecular mechanism through which NRP1 plays a crucial role in the formation of radiation resistance in lung cancer cells is unknown; in particular, more research into transcription factor regulatory mechanisms is needed.

KMT2B (Lysine Methyltransferase 2B), also known as MLL2 (Mixed Lineage Leukemia 2), belongs to the family of mammalian histone H3 lysine 4 (H3K4) methyltransferases and forms a protein complex with WRAD (WDR5, RbBP5, ASH2L, and DPY30), Host Cell Factors 1/2 (HCF 1/2), and Menin. The MLL2 complex is responsible for H3K4 trimethylation (H3K4me3) on specific gene promoters and nearby cis-regulatory sites, regulating bivalent developmental genes as well as stem cell and germinal cell differentiation gene sets [20].

The research results of this project suggest that the present ChIP-seq and RNA-seq analyses reveal that *NRP1* is a key gene directly regulated by GATA3 and H3K4me3 that is involved in the formation of tumor cell radiation resistance. Moreover, radiation resistance mechanisms of the two lung cancer cell types are different. In A549-RR cells, GATA3 and H3K4me3 coregulate *NRP1* expression positively, while GATA3 represses NRP1 expression in H1299-RR cells.

2. Methods and Materials

2.1. Cell Culture and Transfection. Human lung cancer cell lines A549 and H1299 were purchased from Cell Bank Type Culture Collection of the Chinese Academy of Sciences (Shanghai, China). A549 cells were maintained in DMEM/high glucose (Gibco, USA). H1299 cells were maintained in RPMI-1640 medium (Gibco, USA). 10% Fetal Bovine Serum (HyClone, USA), 100 U/ml penicillin, and 100 μg/ml streptomycin were added to the medium. Cell growth environment was in a humidified CO_2 incubator at 37°C and 5% CO_2. Cell lines were regularly confirmed to be free from mycoplasma contamination using MycoAlert Detection Kit (Lonza). GATA3 small interfering RNA (siRNA, GenePharma, China) with the corresponding control RNA (siNC), recombinant plasmid overexpressing GATA3 with the empty pcDNA3.1(+) vector (PLL, Nanjing, China), the lentiviral shRNA against human GATA3 and NRP1 (PLL, China) with corresponding control RNA (shNC), or recombinant plasmid overexpressing NRP1 with the empty PLNCX2 vector (Sigma, USA) were transfected into cells. The transfection was carried out according to the manufacturer's instructions using the Lipofectamine 2000 transfection reagent (Invitrogen, USA). Table S1 shows the sequences of the shRNA and siRNA oligonucleotides.

2.2. Dose-Gradient Irradiation. A549 and H1299 cells were performed at a rate of 1.02 Gy/min for A549 cells and 0.75 Gy/min for H1299 cells [21] at room temperature using an X-ray generator (Model X-RAD320iX, USA). They were exposed to 6 Gy every time, 5 times, 30 Gy in total. Cells were passaged 4 times or more for subsequent experiments. For the mouse radiosensitivity experiment, a radiation dose of 20 Gy was administered when the xenografts reached an average volume of 200 mm^3 [22]. Finally, mice were euthanized at prespecified times.

2.3. Mouse Irradiation Study. Six-week-old BALB/c nude mice were purchased from Beijing Huafukang Biotechnology Company (China). Using lentiviral plasmids (PLL Company, Nanjing, China). We constructed stable knockdown GATA3 cell models in A549 and H1299 cells. Table S1 shows the sequences of the shNC and shGATA3. A total of 1×10^6 cells were resuspended in 100 μl of PBS and injected subcutaneously into the right hind legs of mice. All animals were kept in laboratory animal centers, in accordance with the regulations of the Medical Ethics Committee. Every two days, body weight and tumor volume measures were taken. All animals were sacrificed 14 days after irradiation and their excised tumors were weighed. Tumor volume $(mm^3) = a^2 \times b/2$ (a: length (mm), b: width (mm)). The BALB/c nude mice used in this experiment had passed the quality test, and the license number of Beijing Huafukang Company is SCXK (Jing) 2019-0008.

2.4. Colony Formation Assay. 1000 cells were seeded into 6-well plates. The next day, cells were irradiated with X-rays of 0, 2, 4, 6, 8 Gy. After 2 weeks, cell colonies were washed 3 times with PBS for 3 min each, fixed with 4% paraformaldehyde for 30 min, and stained with crystal violet (Solarbio, Beijing, China) for 30 min.

2.5. Cell Cycle Analysis. The cells were made into one cell suspension, cleaned twice with cold PBS, added with 300 μl of PBS cell suspension, added with 150 μl of 75% ethanol, fixed at 4°C for 2 hours, washed twice with PBS, added with an appropriate amount of PI, placed in the dark for 15 min, and subjected to flow cytometry analysis. The machine type of the flow analyzer is a FACSCalibur flow cytometer, and the company is BD Biosciences (USA).

2.6. Quantitative Real-Time PCR. RNA was remoted with TRIzol (Invitrogen, USA) and reverse transcribed to produce cDNA (TaKaRa Reverse Transcription Kit, Dalian, China) according to the manufacturer's protocol. With GAPDH as the internal control, qRT PCR was performed by the TB-Green assay (Fluorescence Quantitation Kit, TaKaRa). Relative quantification of gene expression was computed using the method of $2^{-\Delta\Delta CT}$. The sequences of the qRT-PCR primers are listed in Table 1.

2.7. Immunofluorescence. The cells were cleaned with PBS three times. Then, we conducted a more in-depth exploration. After washing, the cells were subjected to 30 min of membrane permeation with 0.5% Triton X-100, washed with PBS, and then sealed with 10% BSA for 1 h. Take out the

Table 1: The sequences of the qRT-PCR primers.

qRT-PCR primers		Sequence 5′ to 3′
NRP1	Forward	CCCCAAACCACTGATAACTCG
	Reverse	AGACACCATACCCAACATTCC
GATA3	Forward	AAGGCAGGGAGTGTGTGAAC
	Reverse	CGGTTCTGTCCGTTCATTTT
KMT2B	Forward	TCCATCTTCACTGACCCACC
	Reverse	GTGACGACTGAGGTAGGAGG
GAPDH	Forward	ACGGATTTGGTCGTATTGGG
	Reverse	TGATTTTGGAGGGATCTCGC

blocking solution, put it directly into the wet box, drip the diluted primary antibody, and incubate overnight at 4°C. The next day, after rewarming the wet box at room temperature for 30 min, drip the diluted fluorescent secondary antibody, incubate at room temperature in the dark for 1 h, wash with PBS, drop the sealing agent containing DAPI, store it in a dry cassette at 4°C, and take photos with a fluorescence microscope.

2.8. Western Blotting. The total protein sample was prepared using the NP-40 (Beyotime, Shanghai, China). For western blot analysis, identical amounts of protein were resolved by SDS-PAGE, moved to PVDF membranes, immunoblotted with primary (NRP1 1 : 1000; Flag 1 : 1000; GATA3 1 : 1000) and secondary antibodies (Rabbit antibody 1 : 10000; Mouse antibody 1 : 50000), and detected using chemiluminescence (Pierce ECL kit, Thermo Fisher Scientific). The information about primary and secondary antibodies used in this article is listed in Table 2.

2.9. Immunohistochemistry (IHC). The experiment was carried out according to the immunohistochemical kit (purchased from Maixin, Fujian, China). After staining the tissue sections, mount them and take pictures after drying.

2.10. Chromatin Immunoprecipitation-Quantitative PCR (ChIP-qPCR). The sequences of NRP1 gene promoter region were queried by bioinformatics and matched with the GATA3 protein. There were 11 sequences with a matching score of more than 90%, and the optimal binding sequence was selected to design primers. The experimental steps of ChIP-qPCR were carried out in strict accordance with the kit instructions (purchased from ACTIVE-MOTIF, USA). The unique primer sequences are listed in Table 3.

2.11. Chromatin Immunoprecipitation Sequencing (ChIP-seq). For ChIP-Seq, the Shenzhen ACE Gene Company was responsible for sample preparation and sequencing analysis. Raw reads were aligned to the human refence genome (assembly hg19) using Bowtie 2 [23] with default parameters. Peaks were called with MACS2 [24] with default parameters. The colocalization of GATA3 and H3K4me3 peaks was performed using the bed tool [25] intersect utility. Gene set enrichment analysis of overlapping regions for GATA3 and H3K4me3 was performed with the web app GREAT [26] with default settings.

2.12. Plasmid Transfection and Luciferase Reporter Assays. For luciferase assays to test the interaction between GATA3 and the NRP1 promoter, A549 cells were transiently cotransfected with 100 ng of pGL3-Basic or NRP1 promoter plasmid and 50 ng of pRL-TK, or its negative control using Lipofectamine 3000 (Invitrogen, USA) in 24-well plates. Then, 48 h after transfection, the luciferase activities were tested using a Dual-Luciferase Reporter Assay according to the E1910 Kit (Promega, USA).

2.13. Statistical Analysis. The experimental data in this experiment were statistically analyzed by SPSS 24.0 software, and the obtained data were expressed by means ± standard deviation. The statistical analyses of the experiment data were performed by using a two-tailed Student's paired *t*-test and one-way ANOVA. Statistical significance was assessed at least three independent experiments. $P < 0.05$ considered the difference to be statistically significant.

3. Results

3.1. Establishment of Radiation-Resistant Cell Model. The radioresistant cell lines A549-RR and H1299-RR were created by irradiating the parental A549 and H1299 cell lines with a dose gradient at a high dose of 30 Gy (Figures 1(a) and 1(b)). As the radiation dose increased, we discovered that the survival fraction in A549-RR and H1299-RR cells was substantially higher than in A549 and H1299 cells (Figures 1(c) and 1(d)). Furthermore, A549-RR and H1299-RR cells were larger and had longer pseudopodia compared to parental cells (Figures 1(e) and 1(g)). Next, compared to the parental cells, A549-RR and H1299-RR cells demonstrated a significantly increased survival rate (Figures 1(f) and 1(h)). According to the point-and-click multitarget model, the higher the Dq value, the stronger the ability to repair the sublethal damage of cells. Therefore, the clone formation experiment results confirmed that A549-RR and H1299-RR have stronger damage repair ability (Table S2). The development of radiation resistance resulted in a diffuse cytoplasmic distribution of F-actin (Figures 1(i) and 1(k)). Radiation can cause a different cell cycle arrest [27]. We found that A549-RR cells had G2/M phase arrest and H1299-RR cells had S phase arrest compared with their parents (Figures 1(j) and 1(l)). These results indicate that both A549-RR and H1299-RR cells are resistant to radiation.

3.2. GATA3 and NRP1 Are Involved in the Formation of Radioresistance in Lung Cancer Cells. To study the mechanism of radiation resistance, we performed RNA-sequencing. According to the results of RNA-sequence, there were 15,126 genes coexpressed by A549 and A549-RR cells (Figure 2(a)). Heatmap analysis showed that *NRP1*, *GATA3*, and *KMT2B* were the upregulated genes (Figure 2(b)). KMT2B is a member of the H3K4 histone methyltransferase (HMT) family, which can catalyze the trimethylation of histones. Kyoto Encyclopedia of Genes and Genomes pathways were studied for each module which was performed to investigate the signaling mechanisms. The cancer pathways,

Table 2: Antibodies used in western blotting.

Antibodies	Catalog number	Company	Dilutions
Anti-GAPDH	TA802519	OriGene	1 : 1000
Antineuropilin 1 antibody	ab81321	Abcam	1 : 1000
Anti-GATA3 antibody	ab199428	Abcam	1 : 1000
Antihistone H3 (tri methyl K4)	ab213224	Abcam	1 : 1000
Antihistone H3	ab1791	Abcam	1 : 1000
Flag-tag (1A8) mAb	AP0007M	Bioworld	1 : 1000
Goat antimouse IgG (H+L) HRP	BS12478	Bioworld	1 : 50000
Goat antirabbit IgG (H+L) HRP	BS13278	Bioworld	1 : 10000
Cy3 goat antibody	AS007	ABclonal	1 : 250
Recombinant rabbit IgG	ab172730	Abcam	1 : 100

Table 3: The sequences of the ChIP-qPCR primers.

ChIP-qPCR primers		Sequence 5′ to 3′
NRP1-promoter-primer 1	Forward	CACACTCAGCAGGGAAAGG
	Reverse	GAGCGCCCGTTTGGATAG
NRP1-promoter-primer 2	Forward	GAGCAGTTACCATCCAGTCTAC
	Reverse	TAGGAGGTGCTGCAGAAATAAG

PI3K-AKT pathway [28], and MAPK pathway were found to be overrepresented in the dysregulated genes (Figure 2(c)). Indeed, differential genes were enriched in the GO biological processes related with the plasma membrane (Figure 2(d)), according to Gene Ontology (GO) analysis. Next, we checked the RNA-seq results and discovered that gene expression in A549 and A549-RR cells matched the sequencing results (Figure 2(e)). In H1299 and H1299-RR cells, however, the mRNA expression of NRP1 and GATA3 rose whereas the mRNA expression of KMT2B decreased (Figure 2(f)). Immunofluorescence results showed that GATA3 nucleation was observed in both radiation-resistant models (Figure 2(h)).

3.3. GATA3 Positively Regulates NRP1 Expression in A549-RR Cells but Represses NRP1 Expression in H1299-RR Cells. To begin to understand the role of GATA3-mediated transcriptional regulation, we first designed siRNAs to specifically knock down the expression of GATA3 (Figure S1). GATA3 and NRP1 were knocked down and overexpressed using transient transfection of siGATA3, pcDNA3.1(+)-Flag-GATA3, pSIREN-RetroQ-shNRP1, and pLNCX2-NRP1 plasmids. The qRT-PCR results showed that in A549 and A549-RR cells, the mRNA expression of NRP1 decreased after GATA3 knockdown and increased after GATA3 overexpression (Figure S2). Knockdown of GATA3 downregulated the expression of the NRP1 protein; overexpression of GATA3 upregulated the NRP1 protein (Figure 3(a)). On the other hand, knockdown or overexpression of NRP1 showed no obvious change in the GATA3 protein (Figure 3(b)), indicating that NRP1 does not directly affect the expression of GATA3. Thus, GATA3 can positively regulate NRP1 in A549 and A549-RR cells.

Conversely, the phenomenon in H1299 and H1299-RR cells was the opposite compared to that in A549 cells. The mRNA expression of NRP1 increased after GATA3 knockdown and decreased after GATA3 overexpression in H1299 cells and H1299-RR cells (Figure 3(c)). However, there was no significant change in the expression of GATA3 after knockdown or overexpression of NRP1 in other cells (Figure 3(d)). Taken together, these results indicated that GATA3 negatively regulates NRP1 in H1299 and H1299-RR cells. At the same time, we also detected the mRNA expression levels of GATA3 or NRP1 after knockdown or overexpression and found no obvious trend (Figure S3). Therefore, the regulation of GATA3 on NRP1 mainly reflects its protein expression.

3.4. GATA3 Is Located Upstream of the NRP1 Gene to Regulate Transcription. In order to explore whether GATA3 regulates the transcription of the *NRP1* gene, we constructed a recombinant plasmid of the promoter region of the *NRP1* gene with the pGL3 basic vector. Dual-luciferase reporter assays confirmed that GATA3 promotes activation of the *NRP1* promoter in A549-RR cells, while the ability of GATA3 to activate the *NRP1* promoter was weakened in H1299-RR cells (Figure 4(a)). We analyzed the whole genome distribution of GATA3 target genes in two radiation resistant cells and found that the target genes were widely distributed, including exons, promoters, and so on (Figure 4(b)). In the ChIP-seq analysis, a binding event between GATA3 proteins was observed upstream of the *NRP1* locus (Figure 4(c)). Next, ChIP-qPCR analysis was performed using A549, A549-RR, H1299, and H1299-RR cells and specific antibodies against GATA3 and IgG for selected *NRP1* genes. The results showed a strong enrichment of GATA3 on the gene promoters, validating the

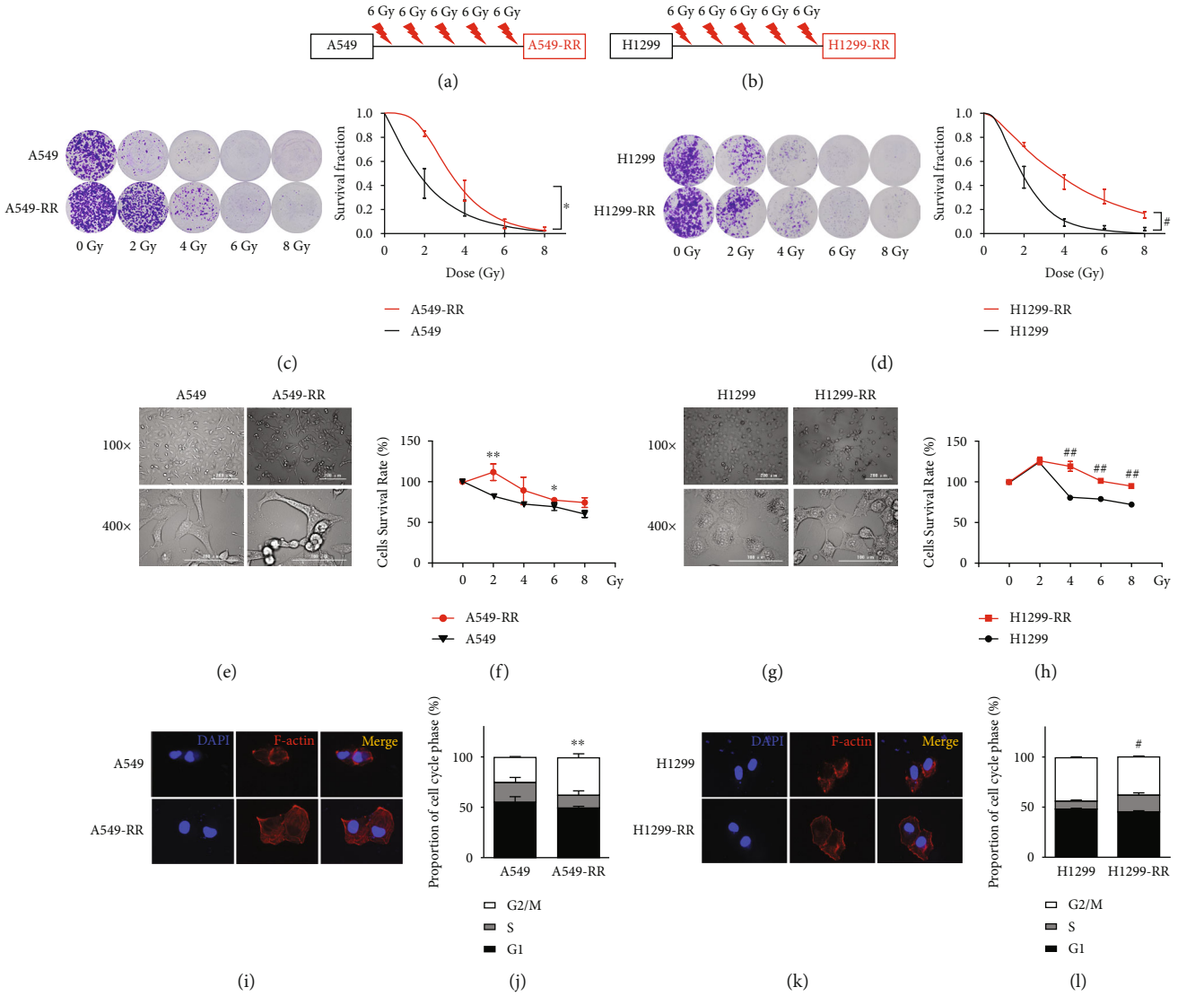

FIGURE 1: A549-RR and H1299-RR cells are resistant to radiation. (a, b) The strategy of A549 and H1299 radiation resistance cells. (c, d) Cell Counting Kit-8 assay was performed to detect the viability and proliferation of the cells. The survival rate was normalized to 0 Gy. (e, g) Cell morphology was observed by light microscope. (f, h) Colony formation assay was performed to detect the viability of the cells. The survival rate was normalized to the 0 Gy group. (i, k) Double staining of cells for F-actin (red) and for cell nuclei with DAPI (blue). (j, l) Cell cycle distribution of each group. Results were presented as mean ± SD of three independent experiments ($n = 3$; $^{*}P < 0.05$, $^{**}P < 0.01$ vs. A549; $^{\#}P < 0.05$, $^{\#\#}P < 0.01$ vs. H1299; two-tailed t-test).

ChIP-seq results (Figure 4(d)). These results indicated that *NRP1* is a high-confidence target gene downstream of GATA3 in lung cancer cells.

3.5. H3K4me3 and GATA3 Jointly Regulate the Transcription of NRP1 Gene. In RNA-seq results, we found that H3K4me3 methyltransferase KTM2D was upregulated in A549-RR cells, so we speculated that H3K4me3 was likely to participate in the formation of radiation resistance. In support of this finding, we examined the expression of H3K4me3 in two radiation resistance models; western blot analysis showed that A549-RR cell lines had a high expression level of H3K4me3. However, H1299-RR cell lines displayed a low H3K4me3 expression level (Figure 5(a)).

Then, how does H3K4me3 affect radiation resistance? In ChIP-sequence analysis, we found that there were 10631 and 8232 target genes jointly regulated by GATA3 and H3K4me3, respectively, in the two radiation resistance models. Surprisingly, NRP1 was the common target gene, E2FA, NR2F2, and so on were included (Figure 5(b)). We next analyzed the chromatin status at the NRP1 target locus in lung cancer cells and found that *NRP1*-enriched regions were frequently associated with an active histone mark (H3K4me3). Furthermore, the enrichment of H3K4me3 in the promoter region of the NRP1 gene in the two radiation resistant models was different. In A549-RR cells, this enrichment increased, whereas in H1299-RR cells, it reduced (Figure 5(c)). Finally, we verified the enrichment of

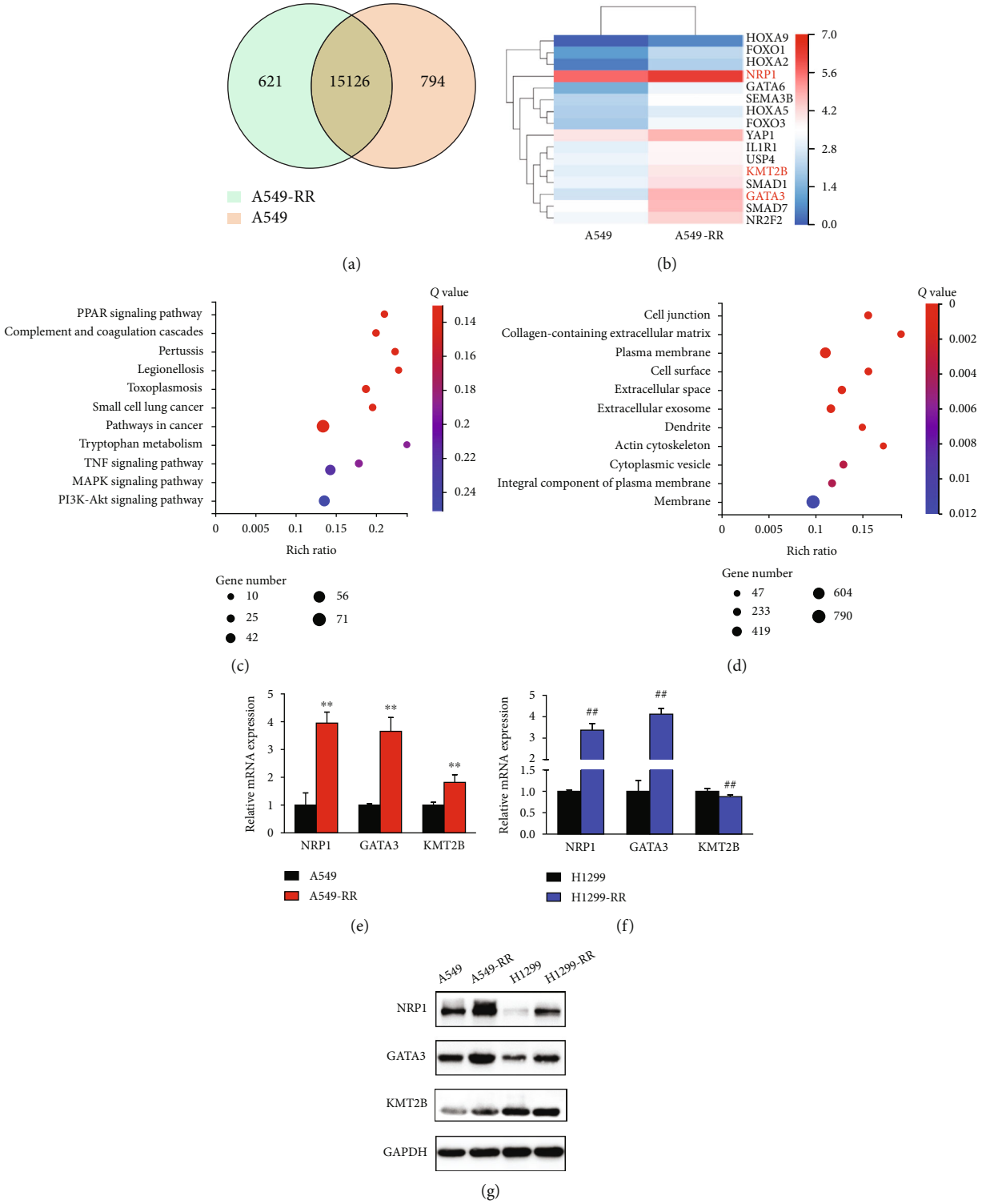

Figure 2: Continued.

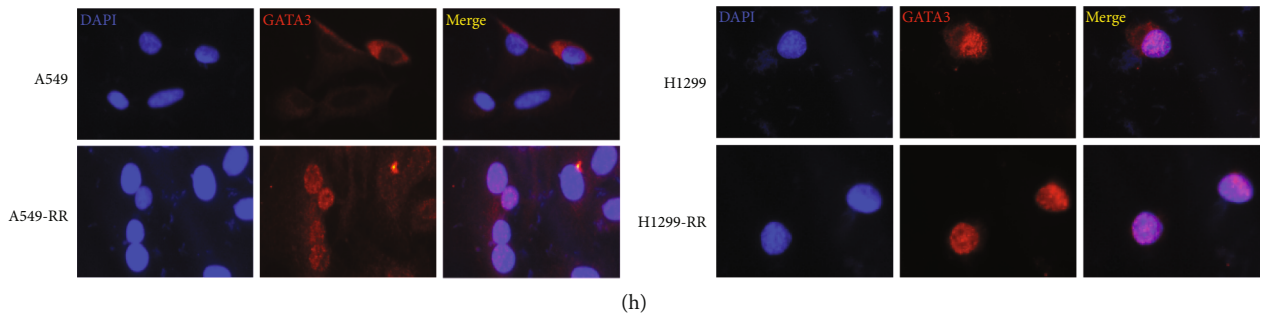

Figure 2: GATA3 and NRP1 are overexpressed in A549-RR and H1299-RR cells. (a) Venn diagram shows the overlap of genes between A549-RR (green) and A549 (yellow). (b) Hierarchical clustering of genes altered by A549 and A549-RR cells. (c) Pathway analysis of differential genes arranged into functional groups. (d) Genes differentially expressed were selected for gene ontology analysis. (e, f) Verification of RNA-seq results through qRT-PCR analysis of the indicated genes in A549, A549-RR, H1299, and H1299-RR cells ($n = 3$; $^{*}P < 0.05$, $^{**}P < 0.01$ vs. A549; $^{\#}P < 0.05$, $^{\#\#}P < 0.01$ vs. H1299; two-tailed t-test). (g) Expressions of NRP1, GATA3, and KMT2B were measured using western blotting ($n = 3$). (h) Immunofluorescence staining of cells for GATA3 (red) or NRP1 (red) and for cell nuclei with DAPI (blue) ($n = 3$).

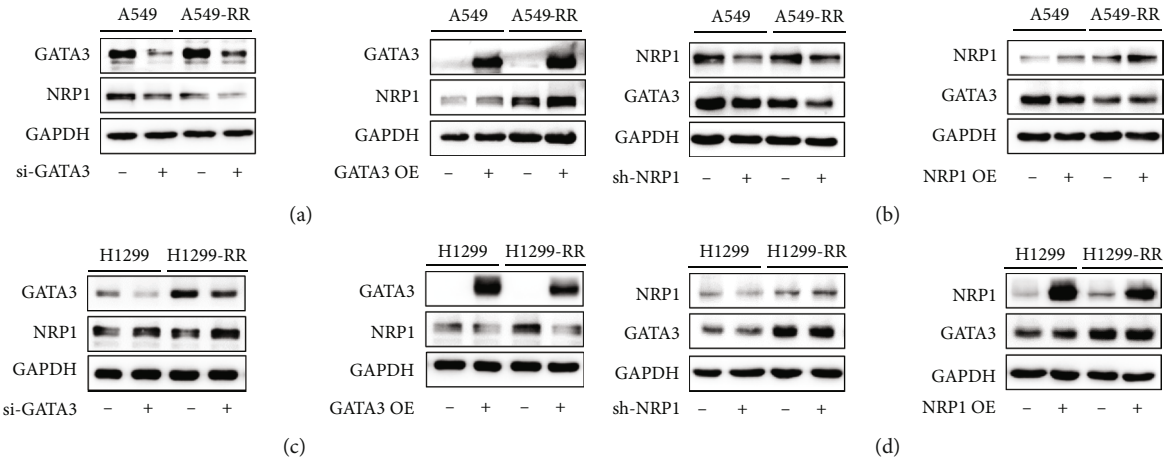

Figure 3: GATA3 positively regulates NRP1 expression in A549-RR cells but represses NRP1 expression in H1299-RR cells. (a) The protein expression of GATA3 and NRP1 involved in A549 and A549-RR cells transfected with negative control siNC, siGATA3, vector, or pcDNA3.1(+)-GATA3. (b) The protein expression of GATA3 and NRP1 involved in A549 and A549-RR cells transfected with negative control shNC or shNRP1 and vector or pLNCX2-NRP1. (c, d) The GATA3 and NRP1 protein level were downregulated or upregulated in H1299 and H1299-RR cells. Cells were transfected for 48 hours and harvested for analysis.

H3K4me3 according to the ChIP-seq site (-2354~-2451). The results showed that H3K4me3 was indeed enriched here, which also confirmed the results of ChIP-seq (Figure 5(d)).

3.6. GATA3 Knockdown Can Enhance A549-RR Cell Radiosensitivity. To directly test whether GATA3 knockdown increases radiosensitivity by regulating NRP1 *in vivo*, nude mice-bearing xenografts from A549-shNC and A549-shGATA3 were treated with or without 20 Gy IR. The xenografted tumors originated from A549 cells with stable low expression of GATA3 genes constructed by subcutaneous injection (Figure S4). Strikingly, GATA3 knockdown combined with IR significantly suppressed A549 tumor growth (Figures 6(a) and 6(b)). However, H1299 cell knockdown GATA3 combined with 20 Gy irradiation did not reduce the tumor (Figure 6(c) and 6(d)). The body weight of nude mice remained essentially unchanged within 14 days after irradiation (Figure S5). IHC results showed that the staining of GATA3 and NRP1 decreased gradually in the four groups (A549-shNC, A549-shNC +20 Gy, A549-shGATA3, and A549-shGATA3+20 Gy) (Figures 6(e) and 6(f)). This indicates that the growth inhibitory effect of tumors is related to the reduction of GATA3 and NRP1. Knockdown of GATA3 combined with high-dose irradiation can inhibit the expression of NRP1. Next, the mRNA (Figure 6(g)) and protein expression levels (Figure 6(h)) of GATA3 and NRP1 in tumor tissues also confirmed our conjecture.

4. Discussion

In recent years, more and more studies have shown that GATA3 is closely related to the prognosis of various cancers. GATA3 is one of the most frequently mutated genes in breast cancer, and its mutation affects breast cancer

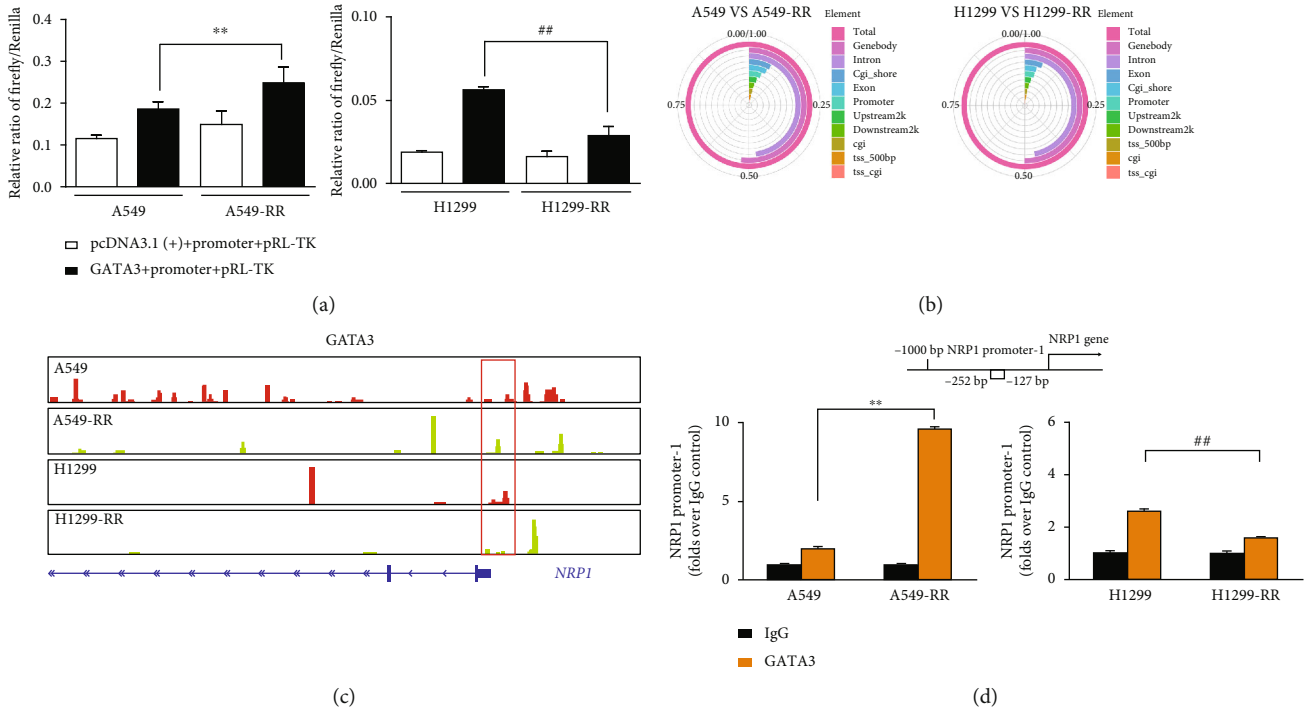

FIGURE 4: GATA3 regulates the expression of NRP1 target gene. (a) Luciferase values in A549, A549-RR, H1299, and H1299-RR cells cotransfected with pcDNA3.1(+), pcDNA3.1(+)-GATA3, or *NRP1* promoter sequence and pRL-TK measured by a dual-luciferase reporter assay. (b) Genomic distribution of GATA3 targets, based on ChIP-seq analysis. (c) ChIP-seq gene tracks show the binding locations of transcription factor GATA3 at the *NRP1* gene locus in A549, A549-RR, H1299, and H1299-RR cells. Red box indicates the region associated with GATA3 signals in four kinds of cells. (d) ChIP-qPCR with IgG and GATA3 antibody in A549, A549-RR, H1299, and H1299-RR cells, followed by qRT-PCR with primers of the *NRP1* promoter-1 region (-252~-127) specific to the GATA3. Data were shown as means ± SD from three independent experiments ($n = 3$; $^{*}P < 0.05$, $^{**}P < 0.01$ vs. A549; $^{\#}P < 0.05$, $^{\#\#}P < 0.01$ vs. H1299; two-tailed t-test).

progression [28]. GATA3 can promote breast cancer invasion and metastasis through epithelial-mesenchymal transition (EMT) [29, 30]. In addition, GATA3 is a major transcription factor for T cell differentiation into Th2-type cells [32], which is involved in the immune microenvironment of lung tumors and maintains chemoresistance [31]. However, the mechanism of action of GATA3 in nonsmall cell lung cancer is still unclear, and whether GATA3 is related to radiation resistance has not been reported. Therefore, the present study explored the mechanism of GATA3 in two radiation-resistant cell models of nonsmall cell lung cancer (A549-RR and H1299-RR).

Firstly, according to the different sensitivity of the two lung adenocarcinoma cells to radiation, we used different dose rates to construct the radiation resistance models. After successful construction, it was found that the two cells had different cell cycle arrest. This phenomenon may be caused by different cellular genetic backgrounds. A549 cells are p53 wild-type and H1299 cells are p53 deletion-type [32–34]. It is well known that p53 is a tumor suppressor and can also regulate the metabolic pathways of cancer cells. RBL2/DREAM-mediated Aurora kinase A/B pathway inhibition in p53 WT NSCLC can increase the radiosensitivity of NSCLC [35]. On the other hand, p53 is an important checkpoint in the G1/S phase. The radioresistance of p53null H1299 cells results in cell cycle checkpoint disturbance and a higher tetraploid ratio compared to that of p53wt A549 cells. It has been demonstrated in the literature that two types of lung adenocarcinoma cells (A549 and H1299) have different sensitivities to radiation, and after conventionally fractionated irradiation regimens, the two types of cells exhibit different apoptosis, metabolic activity, and EMT transformation [36]. This fully demonstrates that nonsmall cell lung cancer (NSCLC) treatments should become more personalized according to the status of key protein molecules in tumor tissue [34]. This also coincides with our research. Our study also found that the mechanisms by which the two types of lung cancer cells develop radioresistance are different, and in-depth exploration has been carried out.

After that, we analyzed the difference of gene expression between A549 and A549-RR cells. The results showed that GATA3 and NRP1, a key gene closely related to the high invasion and metastasis of lung cancer [37–39], were highly expressed. A large number of studies have confirmed that the transcription factors GATA3 and NRP1 are involved in the process of EMT. So, what is the relationship between them? Our study found that NRP1 is a direct downstream target gene of GATA3. GATA3 positively promoted NRP1 expression in A549 and A549-RR cells but inhibited NRP1 expression in H1299 and H1299-RR cells (Figure 3). As we all know, the complexity of transcription factor regulation depends in part on its transcription cofactor. GATA3, as a

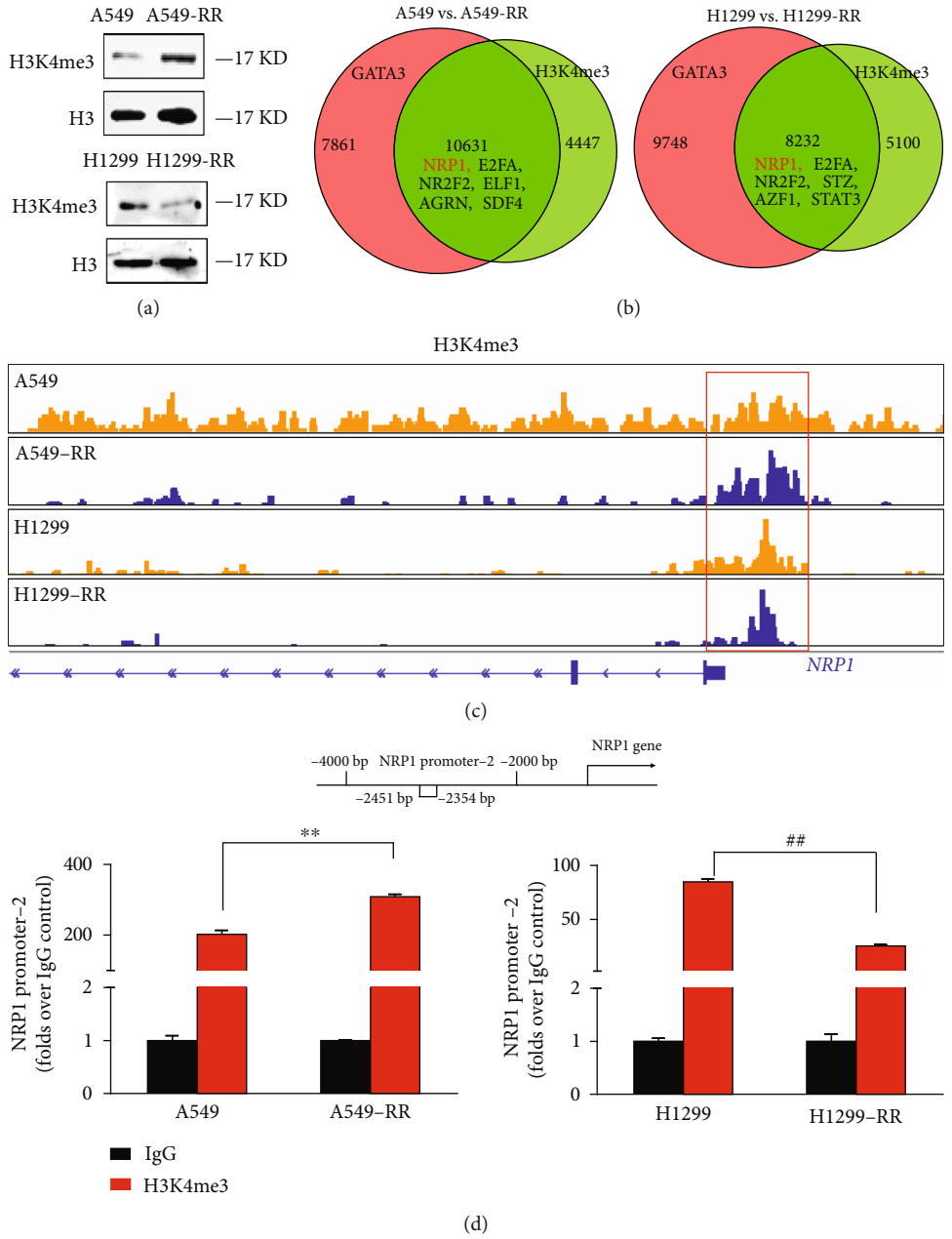

FIGURE 5: H3K4me3 obviously bind to the NRP1 promoter region. (a) The levels of H3K4me3 modifications in histone extracts were determined via western blotting. (b) Venn diagram showing overlapping genes bound by GATA3 and H3K4me3 in A549, A549-RR, H1299, and H1299-RR cells. (c) ChIP-seq gene tracks show the binding locations of H3K4me3at the *NRP1* gene locus in A549, A549-RR, H1299, and H1299-RR cells. Red box indicates the region associated with H3K4me3 signals in four kinds of cells. (d) ChIP-qPCR with IgG and H3K4me3 antibody in A549, A549-RR, H1299, and H1299-RR cells, followed by qRT-PCR with primers of the *NRP1* promoter-2 region (-2354~-2451) specific to the H3K4me3. Data are shown as means ± SD from three separated experiments ($n = 3$; $^{*}P < 0.05$, $^{**}P < 0.01$ vs. A549; $^{\#}P < 0.05$, $^{\#\#}P < 0.01$ vs. H1299; two-tailed t-test).

biological regulator of tumor cells, can form complexes with a variety of proteins to jointly regulate the transcription of target genes.

As research progresses, it has become increasingly recognized that both genetic and epigenetic events can contribute to cancer development [40]. Since epigenetic changes are reversible and epigenetic regulators are often proteins with enzymatic activities, which can regulate the expression of many target genes, and depending on different cell environments, they can play different roles as tumor suppressors or oncoproteins [41]. Therefore, we speculate whether there is a histone modification involved in the regulation of NRP1 by GATA3. We analyzed competitive H3K4me3 and GATA3 binding in the NRP1 promoter region by ChIP and ChIP-seq (Figure 5(c)). H3K4me3 modification is a marker of gene activation [42, 43], which can jointly promote the transcription of NRP1 in A549-RR cells. However, the modification of H3K4me3 in H1299-RR cells was less than that in

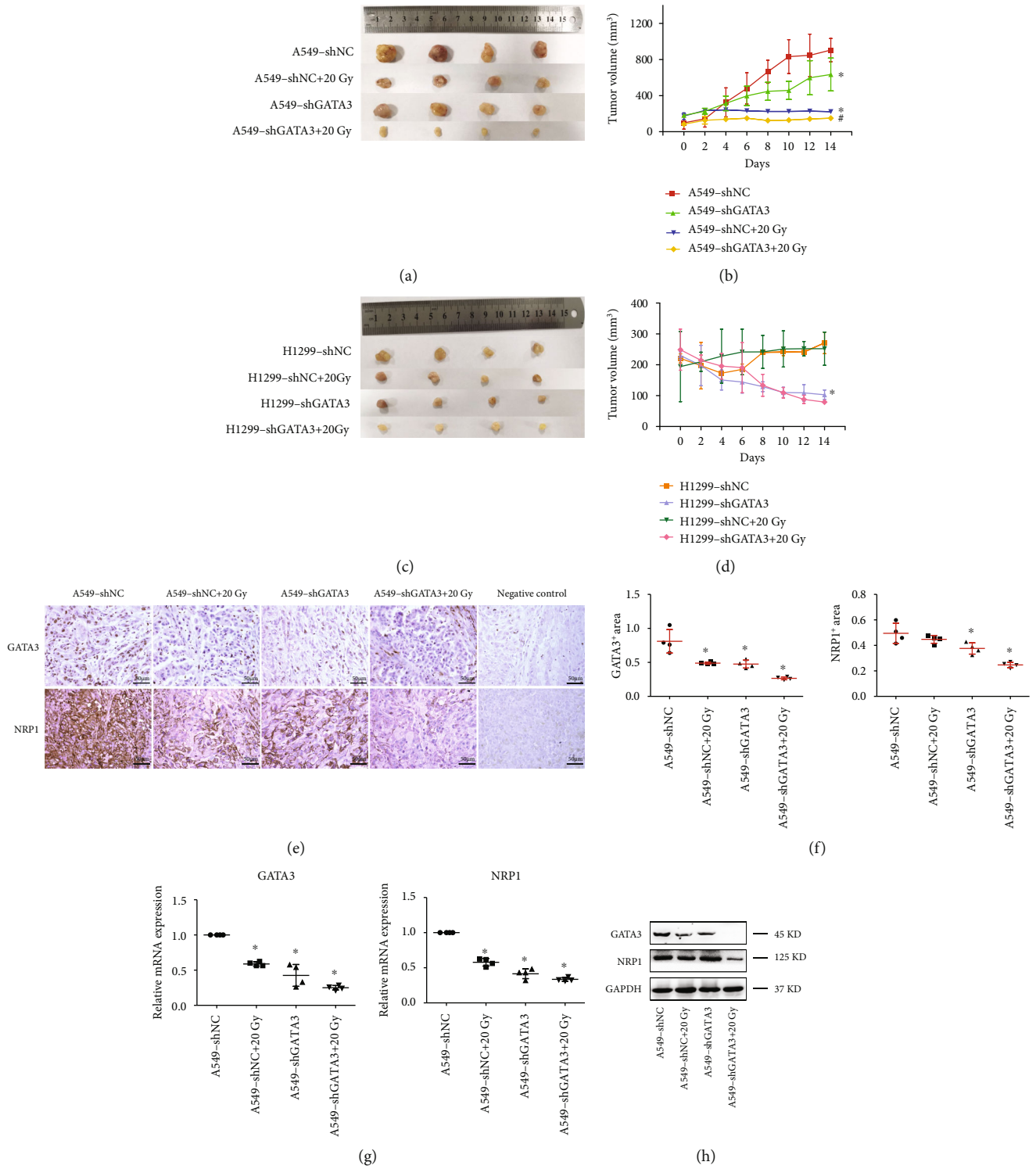

FIGURE 6: Knockdown of GATA3 can enhance the radiosensitivity of A549-RR cells. (a, c) Cells were injected subcutaneously into nude mice. Mice were exposed to 20 Gy of radiation when the tumor volume reached approximately 200 mm^3.The tumor was removed 14 days after irradiation. (b, d) The average volumes of the tumors were measured every 2 days ($n = 4$, $^*P < 0.05$ vs. A549-shNC or H1299-shNC, $^{\#}P < 0.05$ vs. A549-shNC+20 Gy). (e) IHC staining for GATA3 and NRP1 proteins in tumors of the four groups at 14 days. Scale bars, 50 μm. (f) Quantification of GATA3 and NRP1 staining in (e). Dots in (f) depict individual samples. (g) The mRNA expression of GATA3 and NRP1 genes was measured by qRT-PCR in (e). Dots in (g) depict individual samples ($n = 4$, $^*P < 0.05$ vs. A549-shNC). (h) Western blotting was used to detect GATA3 and NRP1 proteins in tumors of the four groups.

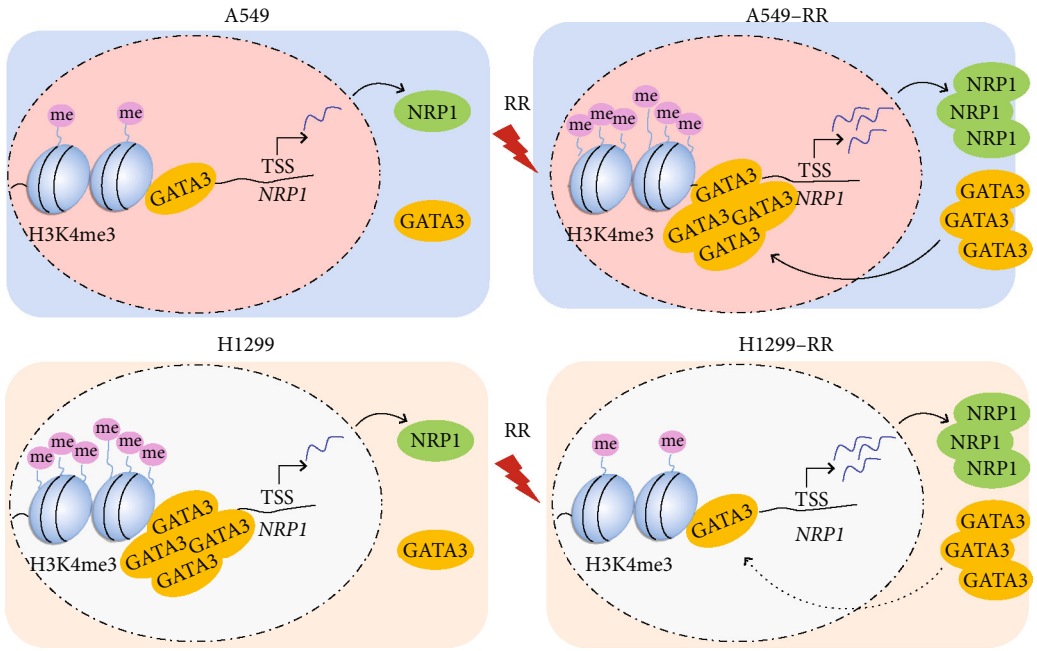

Figure 7: A working model of GATA3/H3K4me3-regulating NRP1-induced radiation resistance in two kinds of nonsmall cell lung cancer cells (A549 and H1299).

H1299 cells, indicating that the role of H3K4me3 in H1299-RR cells was weakened and GATA3 played a leading role. Finally, we verified the regulatory effect of GATA3 on NRP1 in vivo. GATA3 knockdown in A549 cells increased radiosensitivity of A549 cells and reduced tumor volume (Figure 6(a)).

5. Conclusions

In summary, during the formation of radiation resistance in A549 cells, the transcription factor GATA3 will be recruited to the NRP1 gene promoter region. Additionally, the H3K4me3 alteration in the NRP1 gene promoter region will increase, increasing NRP1 gene transcription and resulting in radiation resistance in A549 cells. The process of radiation resistance in H1299 cells, on the other hand, is fundamentally different from that in A549 cells. In H1299 cells, the transcription factor GATA3 acts as a transcription inhibitor to inhibit the transcription of NRP1. Moreover, the enrichment of GATA3 and H3K4me3 in the promoter region of NRP1 gene decreased. Therefore, we speculate that the main factor of radiation resistance in H1299 cells is the increase of NRP1 transcription caused by the decrease of GATA3 enrichment (Figure 7). Overall, our results clarify that GATA3 has different regulatory effects on NRP1 in two lung adenocarcinoma cells, and H3K4me3 is also involved.

Data Availability

The data used to support the findings of this study are available from the corresponding authors upon request.

Conflicts of Interest

The authors confirm that there are no conflicts of interest.

Authors' Contributions

Shunzi Jin and Wei Wei directed the study and granted support. Rui Wang designed and performed most of the experiments, wrote the manuscript, and analyzed the data. Junxuan Yi, Hui Gao, and Xinfeng Wei performed experiments. Lihong Shao, Mingwei Wang, Weiqiang Xu, and Xiaoshu Yin conducted data acquisition and analyses. Yannan Shen and Zhicheng Wang contributed reagents, materials, and analytic tools. All authors read and approved the final manuscript.

Acknowledgments

This work was supported by the grants from the National Natural Science Foundation of China (No. 81872550, 82173454, and 82103783).

Supplementary Materials

Table S1: the sequences of the siRNA oligonucleotides and the shRNA. Table S2: the D_0, n, D_q, SF_2, and R^2 values of the single-click multitarget model. Figure S1: the expression of GATA3 in A549 and A549-RR cells transfected with siRNAs. Figure S2: GATA3 positively regulates NRP1 expression in A549 and A549-RR cells. Figure S3: GATA3 represses NRP1 expression in H1299 and H1299-RR cells. Figure S4: establishment of A549 cell model knockdown GATA3. Figure S5: the average body weights of the mice among groups. *(Supplementary Materials)*

References

[1] S. K. Vinod and E. Hau, "Radiotherapy treatment for lung cancer: current status and future directions," *Respirology*, vol. 25, no. S2, pp. 61–71, 2020.

[2] U. Ricardi, S. Badellino, and A. R. Filippi, "Stereotactic body radiotherapy for early stage lung cancer: history and updated role," *Lung Cancer*, vol. 90, no. 3, pp. 388–396, 2015.

[3] Y. H. Yao, Y. Cui, X. N. Qiu et al., "Attenuated LKB1-SIK1 signaling promotes epithelial-mesenchymal transition and radioresistance of non-small cell lung cancer cells," *Chinese Journal of Cancer*, vol. 35, no. 1, p. 50, 2016.

[4] M. C. Lin, J. J. Lin, C. L. Hsu, H. F. Juan, P. J. Lou, and M. C. Huang, "GATA3 interacts with and stabilizes HIF-1α to enhance cancer cell invasiveness," *Oncogene*, vol. 36, no. 30, pp. 4243–4252, 2017.

[5] I. C. Ho and S. Y. Pai, "GATA-3 - not just for Th2 cells anymore," *Cellular & Molecular Immunology*, vol. 4, no. 1, pp. 15–29, 2007.

[6] T. Hosoya, I. Maillard, and J. D. Engel, "From the cradle to the grave: activities of GATA-3 throughout T-cell development and differentiation," *Immunological Reviews*, vol. 238, no. 1, pp. 110–125, 2010.

[7] T. Yashiro, M. Kubo, H. Ogawa, K. Okumura, and C. Nishiyama, "PU.1 suppresses Th2 cytokine expression via silencing of GATA3 transcription in dendritic cells," *PLoS One*, vol. 10, no. 9, article e0137699, 2015.

[8] M. Takaku, S. A. Grimm, and P. A. Wade, "GATA3 in breast cancer: tumor suppressor or oncogene?," *Gene Expression*, vol. 16, no. 4, pp. 163–168, 2015.

[9] W. Yu, W. Huang, Y. Yang et al., "GATA3 recruits UTX for gene transcriptional activation to suppress metastasis of breast cancer," *Cell Death & Disease*, vol. 10, no. 11, p. 832, 2019.

[10] W. Liu, T. Zhang, L. Guo, Y. Wang, and Y. Yang, "Lysyl hydroxylases are transcription targets for GATA3 driving lung cancer cell metastasis," *Scientific Reports*, vol. 8, no. 1, article 11905, 2018.

[11] T. Kimura, Y. Ishii, K. Yoh et al., "Overexpression of the transcription factor GATA-3 enhances the development of pulmonary fibrosis," *The American Journal of Pathology*, vol. 169, no. 1, pp. 96–104, 2006.

[12] G. J. Prud'Homme and Y. Glinka, "Neuropilins are multifunctional coreceptors involved in tumor initiation, growth, metastasis and immunity," *Oncotarget*, vol. 3, no. 9, pp. 921–939, 2012.

[13] I. Zachary, "Neuropilins: role in signalling, angiogenesis and disease," *Chemical Immunology and Allergy*, vol. 99, pp. 37–70, 2014.

[14] B. M. Lichtenberger, P. K. Tan, H. Niederleithner, N. Ferrara, P. Petzelbauer, and M. Sibilia, "Autocrine VEGF signaling synergizes with EGFR in tumor cells to promote epithelial cancer development," *Cell*, vol. 140, no. 2, pp. 268–279, 2010.

[15] W. Liu, T. Wu, X. Dong, and Y. A. Zeng, "Neuropilin-1 is upregulated by Wnt/β-catenin signaling and is important for mammary stem cells," *Scientific Reports*, vol. 7, no. 1, article 10941, 2017.

[16] Y. Peng, Y. M. Liu, L. C. Li, L. L. Wang, and X. L. Wu, "MicroRNA-338 inhibits growth, invasion and metastasis of gastric cancer by targeting NRP1 expression," *PLoS One*, vol. 9, no. 4, article e94422, 2014.

[17] Z. Ding, W. Du, Z. Lei et al., "Neuropilin 1 modulates TGF-β1-induced epithelial-mesenchymal transition in non-small cell lung cancer," *International Journal of Oncology*, vol. 56, no. 2, pp. 531–543, 2020.

[18] Y. H. Tang, A. Rockstroh, K. A. Sokolowski et al., "Neuropilin-1 is over-expressed in claudin-low breast cancer and promotes tumor progression through acquisition of stem cell characteristics and RAS/MAPK pathway activation," *Breast Cancer Research*, vol. 24, no. 1, p. 8, 2022.

[19] L. Shao, Y. Zhang, X. Gong et al., "Effects of MLL5 and HOXA regulated by NRP1 on radioresistance in A549," *Oncology Letters*, vol. 21, no. 5, p. 403, 2021.

[20] A. Klonou, S. Chlamydas, and C. Piperi, "Structure, activity and function of the MLL2 (KMT2B) protein lysine methyltransferase," *Life*, vol. 11, no. 8, p. 823, 2021.

[21] L. Cong, J. Yi, S. Qiu et al., "Effect of EG00229 on radiation resistance of lung adenocarcinoma cells," *Journal of Cancer*, vol. 12, no. 20, pp. 6105–6117, 2021.

[22] W. Wei, Z. Dong, H. Gao et al., "MicroRNA-9 enhanced radiosensitivity and its mechanism of DNA methylation in non-small cell lung cancer," *Gene*, vol. 710, pp. 178–185, 2019.

[23] B. Langmead and S. L. Salzberg, "Fast gapped-read alignment with Bowtie 2," *Nature Methods*, vol. 9, no. 4, pp. 357–359, 2012.

[24] Y. Zhang, T. Liu, C. A. Meyer et al., "Model-based analysis of ChIP-Seq (MACS)," *Genome Biology*, vol. 9, no. 9, p. R137, 2008.

[25] A. R. Quinlan and I. M. Hall, "BEDTools: a flexible suite of utilities for comparing genomic features," *Bioinformatics*, vol. 26, no. 6, pp. 841-842, 2010.

[26] C. Y. Mclean, D. Bristor, M. Hiller et al., "GREAT improves functional interpretation of cis-regulatory regions," *Nature Biotechnology*, vol. 28, no. 5, pp. 495–501, 2010.

[27] K. Zou, Z. Li, Y. Zhang et al., "β-Elemene enhances radiosensitivity in non-small-cell lung cancer by inhibiting epithelial-mesenchymal transition and cancer stem cell traits via Prx-1/NF-kB/iNOS signaling pathway," *Aging*, vol. 13, no. 2, pp. 2575–2592, 2020.

[28] J. P. Gustin, J. Miller, M. Farag et al., "GATA3 frameshift mutation promotes tumor growth in human luminal breast cancer cells and induces transcriptional changes seen in primary GATA3 mutant breast cancers," *Oncotarget*, vol. 8, no. 61, pp. 103415–103427, 2017.

[29] F. Bai, L. H. Zhang, X. Liu et al., "GATA3 functions downstream of BRCA1 to suppress EMT in breast cancer," *Theranostics*, vol. 11, no. 17, pp. 8218–8233, 2021.

[30] M. Saotome, D. B. Poduval, R. Nair, M. Cooper, and M. Takaku, "GATA3 truncation mutants alter EMT related gene expression via partial motif recognition in luminal breast cancer cells," *Frontiers in Genetics*, vol. 13, article 820532, 2022.

[31] S. Petanidis, K. Domvri, K. Porpodis et al., "Inhibition of kras-derived exosomes downregulates immunosuppressive BACH2/GATA-3 expression via RIP-3 dependent necroptosis and miR-146/miR-210 modulation," *Biomedicine & Pharmacotherapy*, vol. 122, article 109461, 2020.

[32] L. Yang, Y. Zhou, Y. Li et al., "Mutations of p53 and KRAS activate NF-κB to promote chemoresistance and tumorigenesis via dysregulation of cell cycle and suppression of apoptosis in lung cancer cells," *Cancer Letters*, vol. 357, no. 2, pp. 520–526, 2015.

[33] J. Jung, J. S. Lee, Y. S. Lee, and K. Lee, "Radiosensitivity of cancer cells is regulated by translationally controlled tumor protein," *Cancers*, vol. 11, no. 3, p. 386, 2019.

[34] L. Alhaddad, M. Pustovalova, T. Blokhina, R. Chuprov-Netochin, A. N. Osipov, and S. Leonov, "IR-surviving NSCLC cells exhibit different patterns of molecular and cellular reactions relating to the multifraction irradiation regimen and p53-family proteins expression," *Cancers*, vol. 13, no. 11, article 2669, 2021.

[35] L. Duan, R. E. Perez, S. Calhoun, and C. G. Maki, "RBL2/DREAM-mediated repression of the aurora kinase A/B pathway determines therapy responsiveness and outcome in p53 WT NSCLC," *Scientific Reports*, vol. 12, no. 1, article 1049, 2022.

[36] M. Pustovalova, L. Alhaddad, T. Blokhina et al., "The CD44high subpopulation of multifraction irradiation-surviving NSCLC cells exhibits partial EMT-program activation and DNA damage response depending on their p53 status," *International Journal of Molecular Sciences*, vol. 22, no. 5, article 2369, 2021.

[37] L. E. Jimenez-Hernandez, K. Vazquez-Santillan, R. Castro-Oropeza et al., "NRP1-positive lung cancer cells possess tumor-initiating properties," *Oncology Reports*, vol. 39, no. 1, pp. 349–357, 2018.

[38] H. Jia, L. Cheng, M. Tickner, A. Bagherzadeh, D. Selwood, and I. Zachary, "Neuropilin-1 antagonism in human carcinoma cells inhibits migration and enhances chemosensitivity," *British Journal of Cancer*, vol. 102, no. 3, pp. 541–552, 2010.

[39] J. C. Dong, H. Gao, S. Y. Zuo et al., "Neuropilin 1 expression correlates with the radio-resistance of human non-small-cell lung cancer cells," *Journal of Cellular and Molecular Medicine*, vol. 19, no. 9, pp. 2286–2295, 2015.

[40] H. Shen and P. W. Laird, "Interplay between the cancer genome and epigenome," *Cell*, vol. 153, no. 1, pp. 38–55, 2013.

[41] N. Ahuja, H. Easwaran, and S. B. Baylin, "Harnessing the potential of epigenetic therapy to target solid tumors," *The Journal of Clinical Investigation*, vol. 124, no. 1, pp. 56–63, 2014.

[42] G. G. Wang, J. Song, Z. Wang et al., "Haematopoietic malignancies caused by dysregulation of a chromatin-binding PHD finger," *Nature*, vol. 459, no. 7248, pp. 847–851, 2009.

[43] L. A. Farrelly, R. E. Thompson, S. Zhao et al., "Histone serotonylation is a permissive modification that enhances TFIID binding to H3K4me3," *Nature*, vol. 567, no. 7749, pp. 535–539, 2019.